Research and Development Year 2 Report for Award # 277993: Integrity Monitoring and Assessment, Prediction, Repair, and Corrosion Control of the Hanford Storage Tanks

Pavan K. Shukla, Mark Kranjc, Bruce Wiersma, Kiana Sykes, Kareen Blue, Nicholas Valdes, Christine Langton

August 2026

SRNL-RP-2026-00997, Revision 0

SRNL is managed by Batelle Savannah River Alliance for the U.S. Department of Energy's Office of Environmental Management.

DISCLAIMER

Printed in the United States of America

Prepared for the U.S. Department of Energy

SRNL-RP-2026-00997, Revision 0

Research and Development Year 2 Report for Award # 277993: Integrity Monitoring and Assessment, Prediction, Repair, and Corrosion Control of the Hanford Storage Tank

Pavan K. Shukla, Mark Kranjc, Bruce Wiersma, Kiana Sykes, Kareen Blue, Nicholas Valdes, Christine Langton

August 2026

Keywords: Corrosion, Waste Tank Integrity, Corrosion Monitoring
Retention: Permanent

SRNL-RP-2026-00997, Revision 0

Savannah River National Laboratory is operated by Battelle Savannah River Alliance for the U.S. Department of Energy under Contract No. 89303321CEM000080.

Reviews and Approvals

LEAD AUTHOR:

PAVAN SHUKLA (Affiliate) Digitally signed by PAVAN SHUKLA (Affiliate)
Date: 2026.08.19 09:22:55 -04'00'

P. K. Shukla, SRNL Date

TECHNICAL REVIEWER:

MORGANA WHITESIDE (Affiliate) Digitally signed by MORGANA WHITESIDE (Affiliate)
Date: 2026.08.19 10:17:45 -04'00'

M. Whiteside, SRNL Date

APPROVAL:

JOSEPH MANNA (Affiliate) Digitally signed by JOSEPH MANNA (Affiliate)
Date: 2026.08.19 17:33:59 -04'00'

J. Manna, SRNL/Director, Materials Technology and Energy Sciences Division Date

MICHAEL STONE (Affiliate) Digitally signed by MICHAEL STONE (Affiliate)
Date: 2026.08.20 08:56:50 -04'00'

M. Stone, SRNL/DOE-EM Program Manager Date

Preface or Acknowledgements

The authors acknowledge the U.S. Department of Energy-Environmental Management for the funding and support to conduct this research. The development of more robust reference electrodes for in-situ monitoring of tank corrosion is under the umbrella of a program that was initiated as part of the “R&D Roadmap for Hanford Tank Waste Mission Acceleration” (NNLEMS-2022-00005).

Executive Summary

U.S. Department of Energy (DOE) conducted a research program with the focus of preserving and increasing available volume for waste storage at Hanford. The long-term availability and operability of the Hanford Double Shell Tanks (DST) is critical to the completion of the Hanford mission. Maintaining the integrity of the tank will involve having a technology for repair or refurbishment of a DST should the tank function be compromised by degradation, monitoring the tank for indications of accelerated degradation, developing a means for mitigating accelerated degradation, and evaluating options for increasing the storage capacity in the tank farm without construction of new tanks. The project work was started in the middle of 2024; significant progress has been made in the following four areas: (i) Task 1 — tank refurbishment using a high-performance grout and an epoxy sealant layer system, (ii) Task 2 — developing a chemically and radiologically stable reference electrode, (iii) Task 3 — designing and implementing a cathodic protection system to mitigate underside corrosion of DST secondary shells, and (iv) Task 4 — exploring evaporation to increase waste storage capacity and a cost benefit analysis of the existing tanks' refurbishment versus new tank construction.

Year 2 of the program began in the second quarter of FY25. The project focused on materials development and associated testing for refurbishing DSTs. SRNL has developed a two-layer approach, consisting of a grout layer overlayed by an epoxy layer. Grout formulations were developed to obtain satisfactory flowable and pumpable properties. Epoxy materials were tested for their glass transition temperatures, compression strength, shrinkage, rheology, and workability time. Testing was also conducted to understand and determine the bond strength between the grout and epoxy layers.

The project work includes developing a chemically and radiologically robust reference electrode for corrosivity monitoring of the DST contents. To this end, SRNL developed new design concepts for the reference electrodes and filed an invention disclosure associated with the design concepts for patent application consideration in Year 2. In addition, SRNL worked with industry partners to fabricate prototypes using the novel designs of the reference electrode. Further, chemical testing of the materials to be used to fabricate the prototypes was conducted. The chemical testing data was used to evaluate the long-term performance of the prototypes.

The project work also included developing an implementation plan for cathodic protection to mitigate the underside corrosion of the DST secondary liners. To this end, a large-scale model of a DST tank farm was developed in Year 2; the model includes complex buried structures interconnected with several tanks in a tank farm. Several concepts were explored to make computationally viable analysis assumptions for the existing cathodic protection (CP) system and new CP system design to mitigate the secondary liner underside corrosion.

The project activities were paused mid-way in Year 2 as per DOE order.

Table of Contents

1.0 Introduction and Year 2 Accomplishments……1
2.0 Deliverables…… 2

List of Tables

Table 1. List of presentations delivered in 2026 Waste Management conference and invention disclosures 2

Table 2. Deliverable Status for Award Number 277993.....3

List of Abbreviations

SRNL	Savannah River National Laboratory
DST	Double-Shell Tanks
CP	Cathodic Protection
FIU	Florida International University

1.0 Introduction and Year 2 Accomplishments

The long-term availability and operability of the Hanford Double Shell Tanks (DSTs) is critical to the completion of the Hanford mission. Maintaining the integrity of the tanks will involve having technological options for: 1) repair or refurbishment of a DST should the tank function be compromised by degradation, 2) monitoring the tank for indications of accelerated degradation, 3) developing a means for mitigating accelerated degradation, and 4) evaluating options for increasing the storage capacity in the tank farm without construction of new tanks. The overall project team consists of:

Partner	Role/Task
Savannah River National Laboratory	Lead, Contracting, Program Management
Florida International University	High-performance grout and polymeric material
DNV Columbus	Testing for developing robust reference electrode
CorrPro	Cathodic Protection Design Development
Finite Element Expert, Andrew Nordquist	Develop Model to Support Cathodic Protection Design Effort

Year 2 of the program began in the second quarter of FY25. The project focused on materials development and associated testing for refurbishing DSTs. SRNL has developed a two-layer approach, consisting of a grout layer overlayed by an epoxy layer. Grout formulations were developed to obtain satisfactory flowable and pumpable properties. Epoxy materials were tested for their glass transition temperatures, compression strength, shrinkage, rheology, and workability time. Testing was also conducted to understand and determine the bond strength between the grout and epoxy layers. A full task report, consisting of SRNL and FIU reports, is attached in Appendix 1.

The project work included developing a chemically and radiologically robust reference electrode for corrosivity monitoring of the DST contents. To this end, SRNL developed new design concepts for the reference electrodes and filed an invention disclosure associated with the design concepts for patent application consideration. In addition, SRNL worked with industry partners to fabricate prototypes using the novel designs of the reference electrode. Further, chemical testing of the materials to be used to fabricate the prototypes was conducted. The chemical testing data was used to evaluate the long-term performance of the prototypes. A full task report for the reference electrode work is attached in Appendix 2.

The project work also included developing an implementation plan for cathodic protection to mitigate the underside corrosion of the DST secondary liners. To this end, a large-scale model of a DST tank farm was developed; the model includes complex buried structures interconnected with several tanks in a tank farm. Several concepts were explored to make computationally viable analysis assumptions for the existing cathodic protection (CP) system and new CP system design to mitigate the secondary liner underside corrosion. A full task report for the CP development effort is attached in Appendix 3.

This project demonstrated development of the deployable technologies and applicable scientific bases to help maintain the Tank Farm critical asset (i.e., DSTs) for the Hanford tank waste treatment mission. Table 1 lists the presentations delivered at the 2026 Waste Management conference during Year 2.

Table 1. List of presentations delivered in 2026 Waste Management conference and invention disclosures	
Document Number	**Title**
WM26 Conference Paper	Update on Integrity Monitoring, Prediction and Assessment, Corrosion Control, and Repair of the Hanford Storage Tanks
WM26 Conference Paper	Flowable Cementitious Grouts for False Bottoms in Hanford Waste Tanks
WM26 Conference Paper	Study of Epoxy Sealant Layer for Use in Tank Bottom Refurbishment for the DOE EM Tank Waste R&D Program
WM26 Conference Paper	Adhesion Performance of Polymeric Epoxy Coatings on Grout for Nuclear Waste Tank Refurbishment
WM26 Conference Paper	Development of a Robust Reference Electrode for Use in Aggressive Chemical and Radiation Environments
WM26 Conference Paper	Evaluation of Hanford Supernatant Waste Evaporation
SRNL-STI-2025-00235	Evaluation of Hanford Supernatant Waste Evaporation
SRS Docket No. 25-018	Invention Disclosure: Robust High Performance Reference Electrodes for Aggressive Environments
SRS Docket No. 25-020	Robust High Performance Reference Electrodes for Radiation Environments

The project activities were paused mid-way of Year 2 as per DOE order.

2.0 Deliverables

Table 2 list various deliverables status for the project. The status provide completeness levels of the deliverables. Some of the deliverables not completed in Year 1, were completed in Year 2. In addition, several of Year 2 deliverables were only partially completed due to incomplete funding. All Year 2 deliverables are listed in Table 2.

Table 2. Deliverables Status for Award Number 277993			
Deliverable	**Status**	**Document Number**	**Notes**
1. Evaluation of candidate epoxy material (Task 1 Year 2 deliverable)	Completed	SRNL-TR-2026-00446 and FIU-ARC-2026-800019286-04b-001	Task 1 report is attached as Appendix 1.
2. Complete scoping tests to determine accelerated aging conditions (Task 1 Year 2 deliverable)	Partially completed	SRNL-TR-2026-00446	Scoping test included testing with the grout material. The data and results are documented in the report attached as Appendix 1.
3. Preparation for large-scale testing in Year 2 (Task 1 Year 2 deliverable)	Not completed	____	____
4. Chemical and radiating testing of the reference electrode materials (Task 2 Year 2 deliverable)	Partially completed	SRNL-STI-2026-00432	Chemical testing was conducted but not the radiation testing. Chemical testing was used to evaluate long-term expected performance of the prototype reference electrode. Task 2 report is attached in Appendix 2.
5. Prototype reference electrode development (Task 2 Year 2 deliverable)	Partially completed	SRNL-STI-2026-00432	Development of the prototypes, working in conjunction with industry partners, was started but could not be completed.
6. Complete collection of existing CP system details for a given Hanford tank farm (Task 3 Year 1 deliverable)	Completed	SRNL-STI-2026-00371	Collected information was incorporated in the large-scale model described in the report. Task 3 report is attached in Appendix 3.
7. Complete development of close-couple CP system design for DSTs (Task 3 Year 1 deliverable)	Completed	SRNL-STI-2026-00371	The model is documented extensively in the report attached in Appendix 3.
8. Complete development of finite element-based model for CP systems (Task 3 Year 1 deliverable)	Completed	SRNL-STI-2026-00371	The development of the finite element model is extensively documented in the report.

Table 2. Deliverables Status for Award Number 277993			
Deliverable	**Status**	**Document Number**	**Notes**
9. Analyze Model to Study Interaction Between CP Systems (Task 3 Year 2 deliverable)	Not completed	____	____
10. Develop Tank CP System Implementation Plan (Task 3 Year 2 deliverable)	Not completed	____	____
11. Catalogue cost of various storage options (Task 4 Year 2 deliverable)	Not completed	____	____
12. Compare the storage cost option with the repair and refurbishing existing tanks (Task 4 Year 2 deliverable)	Not completed	____	____

Appendix 1: Task 1 (Tank Bottom Refurbishment) — SRNL-TR-2026-00446 and FIU-ARC-2026-800019286-04b-001

Tank Bottom Refurbishment Year 2 Report

Portion of Award #277993: "Integrity Monitoring and Assessment, Prediction, Repair, and Corrosion Control of the Hanford Storage Tanks"

Contributors:

M. Alderman, K. Blue, M. Kranjc, C. Langton, N. Valdes

August 2026

SRNL-TR-2026-00446, Revision 0

SRNL is managed by Batelle Savannah River Alliance for the U.S. Department of Energy's Office of Environmental Management.

DISCLAIMER

Printed in the United States of America

Prepared for the U.S. Department of Energy

Tank Bottom Refurbishment Year 2 Report

For Portion of Award #277993:

"Integrity Monitoring and Assessment, Prediction, Repair, and Corrosion Control of the Hanford Storage Tanks"

M. Alderman, K. Blue, M. Kranjc, C. Langton, N. Valdes

Date: August 2026

Keywords: Waste Tanks, Hanford, Epoxy, Grout, Tank Bottoms
RSM Track: SRNL-TR-2026-00446

Savannah River National Laboratory®

Savannah River National Laboratory is operated by Battelle Savannah River Alliance for the U.S. Department of Energy under Contract No. 89303321CEM000080.

Reviews and Approvals

AUTHORS:

MARK KRANJC (Affiliate) Digitally signed by MARK KRANJC (Affiliate) Date: 2026.08.12 11:25:06 -04'00'

Mark Kranjc, sub PI of Project #277993, L3320/Material Evaluation & NDE Group Date

NICHOLAS VALDES (Affiliate) Digitally signed by NICHOLAS VALDES (Affiliate) Date: 2026.08.12 09:59:22 -04'00'

Nicholas Valdes, L3310/Glass, Cement, and Ceramic Science Group Date

TECHNICAL REVIEWER:

KIANA SYKES (Affiliate) Digitally signed by KIANA SYKES (Affiliate) Date: 2026.08.12 11:47:01 -04'00'

Kiana Sykes, L3340/Material Science and Disposition Group Date

APPROVAL:

PAVAN SHUKLA (Affiliate) Digitally signed by PAVAN SHUKLA (Affiliate) Date: 2026.08.12 12:53:59 -04'00'

Pavan Shukla, Overall PI of Project #277993, L3340/Materials Science & Disposition Group Date

THOMAS SKIDMORE (Affiliate) Digitally signed by THOMAS SKIDMORE (Affiliate) Date: 2026.08.12 13:29:52 -04'00'

Eric Skidmore, Manager, L3320/Material Evaluation & NDE Group Date

JOSEPH MANNA (Affiliate) Digitally signed by JOSEPH MANNA (Affiliate) Date: 2026.08.12 14:03:32 -04'00'

Joseph Manna, Director, Materials Technology & Energy Sciences Division Date

Acknowledgements

This work was made possible by funding provided by the Department of Energy – Environmental Management (DOE-EM) Hanford Tank Waste R&D (LAB23-EM001) program, Award #277993. The authors would like to thank Group L1310, Advanced Manufacturing and Design (Camden Chatham, Haley Jones, Cade Willis, Kylee Denardo, Brandon Walden, and others) for use of their polymer characterization equipment (DMA, Rheometer, and DSC) and 3D printing the silicon molds for casting of multiple cylindrical samples for compressive stress strain testing. Thanks also go to Group L1120 (Annie Mullins) for performing Compression Stress/Strain on the cured epoxy cylinders on their MTS Tensile/Compression Tester. Thanks also go to H2C (Stephanie Doll, Kayle Boomer, and David Swanberg) for providing a letter of recommendation in the proposal stage, attending update meetings, providing the service conditions that the refurbished waste tanks would operate under, answering questions, and general guidance provided throughout this research.

Executive Summary

This report summarizes findings from Year 2 and Year 1 of the "Tank Bottom Refurbishment" portion for Award #277993 "Integrity Monitoring and Assessment, Prediction, Repair, and Corrosion Control of the Hanford Storage Tanks". Additional accomplishments from Year 1 can be found in SRNL-TR-2025- 00233. This work was funded by the Hanford Tank Waste R&D (LAB23-EM001) program. The Award was divided into three sub projects, the other two projects focused on "Improving In-Tank Reference Electrodes for Corrosion Monitoring" and "Cost-Benefit Analysis of Evaporation and Double Shell Tank Corrosion Protection". Award #277993 focused on extended use of waste tanks beyond their intended service life to assist in waste retrieval which is a top priority in the "R&D Roadmap for Hanford Tank Waste Mission Acceleration". Unfortunately, in late March 2026 the DOE Hanford Field Office decided to redirect funding away from these Hanford Tank Waste R&D program (LAB23-EM001) projects to other site operations and EM programmatic priorities. This essentially ended what was proposed to be a 3 year project into only a 1.5 year project.

The initial proposed method to refurbish a waste tank bottom was to use a single layer of grout material composed of a combination cement/polymer binder with or without aggregate. Due to concerns with adhesion of the grout to a decades old carbon steel tank bottom, low flowability of the polymer grout, and permeability of moisture through the polymer/cement grout it was decided to move to a two-layer approach. This is composed of an initial cementitious grout layer poured on top of the tank bottom, allowed to solidify, and then pour a second epoxy sealant layer on top of the fresh grout surface. Additional reasons for going to a two-layer approach are given in section 1.0 Introduction of the report.

Four cementitious grout formulations were identified as potential choices for the first grout layer. They all exhibited adequate fresh and cured properties, especially flow using the ASTM C1611 slump flow test, with grouts A and B showing greater flow than grouts C and D as well as greater compressive strengths. Compressive strength could be an indicator of cohesive strength. In general cement or concrete has high compressive strength and low tensile strength. If cohesive strength of the cementitious grout is very low this could mask low adhesive strengths between epoxy and grout when using our adhesive strength test, ASTM C7234 Pull-Off Strength of Coatings on Concrete.

Several epoxy formulations were initially tested for mixed epoxy+curative flow properties during cure and the most favorable results were obtained on a formulation that AVANTech had tested in collaboration with Washington River Protection Solutions (WRPS) several months prior to when this research began. An NDA agreement was signed at the end of Year 1 to gain access to this formulation. Favorable things about this epoxy formulation are the following: relatively low maximum cure temperature while curing at room temperature, no heating required to initiate cure; slow cure rate, maximum cure temperature reached after 3 to 4 hours and maximum cure reached between 14 and 28 days as measured by the glass transition temperature (Tg); low shrinkage, no gap observed when cast molded in a 48"x48" mold to a thickness of 2 inches; a Tg (52 ^{O}C) of greater than 20 ^{O}C above the maximum service temperature (27 ^{O}C), therefore the polymer will be in the glassy state during service and degrade at a lower rate than if it were above Tg. Two drawbacks of this epoxy are: (1) its relatively low Tg, which could make accelerated aging tests more difficult; and (2) the inclusion of an aliphatic reactive filler. While this filler improves the epoxy's viscoelastic properties and helps prevent cracking, it may also produce degradation by products such as volatile organic compounds and hydrogen gas.

This report also outlines the testing that had been planned for the remaining 1.5 years of the expected 3 years. This primarily consisted of scaling up to an 8 ft diameter tank and preparation for that. SRNL was also preparing to collaborate with AGI Engineering to speed up the scale up process. In addition, Areas of Concern and Technology Gaps are Identified in section 3.0 and Accomplishments/Conclusions are summarized at the end in section 4.0. The items mentioned in this paragraph should assist any researchers if and when it is decided to continue work on refurbishing waste tank bottoms.

Table of Contents

1.0 Introduction 1
2.0 Delivery of Year 2 Milestones 4
2.1 Evaluation of Cementitious Grout 4
2.1.1 Criteria for Using Cementitious Grouts in Tank Refurbishment 4
2.1.2 Materials and Methods 5
2.1.3 Fresh Properties 6
2.1.4 Cured Properties 8
2.1.5 Chemical Durability 9
2.2 Evaluation of NDA Epoxy 12
2.2.1 Processing Properties Evaluation 12
2.2.2 Final Physical Properties Testing 13
2.3 Expectations for Physical Properties 15
2.3.1 Glass Transition Temperature, Tg 15
2.3.2 Compressive Strength 17
2.3.3 Adhesion Strength 19
2.3.4 Dimensional Changes 19
2.3.5 Plans for Accelerated Aging and Concerns 20
2.4 Scaling Up and Heat Transfer Experiments 22
3.0 Areas of Concern and Technology Gaps Identified 24
4.0 Accomplishments/Conclusions 27
5.0 References 28
APPENDIX A: Requirements for the Epoxy Sealant Layer A-1
APPENDIX B: Requirements for the Initial Grout Layer B-1
APPENDIX C: AGI Contact Information C-1

List of Tables

Table 1. Flowability Data of the Mixes 7
Table 2. Flows at Initial, and Static and Dynamic conditions after 90 min. Scale bar is 10 in 8
Table 3. Cured Property Data of the Mixes. 9
Table 4. Pictures of Grout A After Exposure to Various Conditions (samples were immersed for 389 days, discs are 2 in. diameter). 10
Table 5. Results from Tg and Compression Testing. 14
Table 6. Results of Pull Up Pressure and Type of Failure. 15
Table 7. Comparison of Table 1 properties (Tg and Compression) to test sample aged at 150 °C for 30 days after cure 18
Table 8. Shrinkage and Weight Loss of Compression Cylinder Over 31 Days at 150 °C 19
Table 9. Desirable Properties of the Epoxy Layer A-2
Table 10. Criteria of Using Grout for Tank Refurbishment B-2
Table 11. Outcome of Grout Testing to Date B-2

List of Figures

Figure 1 On the left is an illustration of the two layer approach and on the right is a panoramic photo of tank AY102, a DST, after extensive cleaning. 1
Figure 2. Slump flow by ASTM C1611, for A) Grout A, B) Grout B, C) Grout C, D) Grout D 7
Figure 3. Grout B Sample After 60°C Immersion in Simulant for 227 Days. 10
Figure 4. Weight Change Over Time for Grout A Samples in A) Simulant, B) DI Water. 11
Figure 5. Isothermal cure curves of SRNL and NDA Epoxies with usual curative and Jeffamine curative. 13
Figure 6. Tg vs Days of Cure for NDA Epoxy. 14
Figure 7. Stress Strain Curves for NDA Epoxy after 14, 28 , and 56 days of cure. 14
Figure 8. Bottom of Adhesion Pull Up Test Fixtures showing modes of Failure. 15
Figure 9. DSC scans on the same sample after 14 days and 28 days of cure. 16
Figure 10. DMA curve generated from a sample of the NDA Epoxy after 28 days of cure. 17
Figure 11. Compression test of a cylinder cured for over 56 days and then aged for 30 days at 150O C. See blue curve. 18
Figure 12. %Change in Diameter and Length of Compression Cylinder after 31 days at 150 °C. 20
Figure 13. %Change in Weight of Compression Cylinder after 31 days at 150 °C. (Trend line added to assist seeing the data points). 20
Figure 14. 8 foot diameter tank on the left and 8 foot diameter cribbing on the right. 22
Figure 15: Examples of in line mixers. Clear PVC piping with baffles visible inside on the left. Stainless steel piping with high viscosity baffles partially removed and shown on the right for high viscosity liquids like two part epoxies. 23
Figure 16. On the left is a photo of a not to scale mockup of AGI robotic sluicing arms in a Hanford waste tank. On the right is the result of filling any gap that would develop at the tank wall using the AGI robotic arm. 24

List of Abbreviations

ALARA	As Low As Reasonably Attainable
ALC	Air Lift Circulator
ASTM	American Standard Test Methods
bp	boiling point
CTE	Coefficient of Linear Thermal Expansion
DGEBA	Diglycidyl ether of bisphenol A
DMA	Dynamic Mechanical Analysis
doe	design of experiment
DOE	Department of Energy
DSC	Differential Scanning Calorimetry
DST	Double Shell Tank
EDL	Engineering and Design Laboratory
FIU	Florida International University
G’	Storage Modulus
G”	Loss Modulus
H2C	Hanford Tank Waste Operations and Closure (Hanford to Closure)
IQRPE	Independent Qualified Registered Professional Engineer
M	Molar
mCi/L	milliCuries per Liter
η^*	Complex viscosity
NaOH	Sodium Hydroxide
NDA	Nondisclosure Agreement
rad	Radiation
SRNL	Savannah River National Laboratory
SRS	Savannah River Site
tan δ	Tan Delta (= G”/G’)
TTS	Time temperature Superposition
TTCS	Time Temperature Chemical Superposition
Tg	Glass Transition Temperature
Tm	Melting point of crystalline regions in a polymer
UHPC	Ultra High Performance Concrete
WM2025	Waste Management 2025 Conference
WRPS	Washington River Protection Solutions

1.0 Introduction

Starting date was April 1, 2024 for the "Integrity Monitoring and Assessment, Prediction, Repair, and Corrosion Control of the Hanford Storage Tanks" project. This was a part of the Hanford Tank Waste R&D (LAB23-EM001) program (Award #277993). The first half funding installment for Year 2 was received in April of 2025, however, the second half installment for Year 2 funding of all projects under LAB23-EM001 was held back by the DOE Hanford Field Office in October of 2025. In late March 2026 the DOE Hanford Field Office decided to redirect funding away from these Hanford Tank Waste R&D (LAB23-EM001) program projects to other site operations and EM programmatic priorities. What had been planned to be a project funded for three years became funded for only 1.5 years.

This report is on the accomplishments of the "Repair" portion of Award #277993. The Award was divided into three sub projects; this sub project was on "Refurbishment of Hanford Tank Bottoms". The other two projects focused on "Improving In-Tank Reference Electrodes for Corrosion Monitoring" and "Cost-Benefit Analysis of Evaporation and Double Shell Tank Corrosion Protection". Award #277993 focused on extended use of waste tanks beyond their intended service life to assist in waste retrieval which is a top priority in the "R&D Roadmap for Hanford Tank Waste Mission Acceleration". [1]

In the original proposal for the tank bottom refurbishment portion of award #277993, it was anticipated that a single layer of polymer-modified cement would be used. This material, which consists of cement mixed with a polymer making up more than 5% of the total mixture, was considered for refurbishing or improving tank bottoms that had experienced significant thinning due to corrosion. After a review of prior research and some initial investigations it was hypothesized that a two layer approach would be better. This would consist of an initial grout layer (containing cement, no polymer binder) being poured first on the carbon steel tank bottom and then an epoxy sealant layer would be poured over that first grout layer after it had solidified and hydrated. [2], [3], [4], [5], [6] This is illustrated on the left in **Figure 1**.

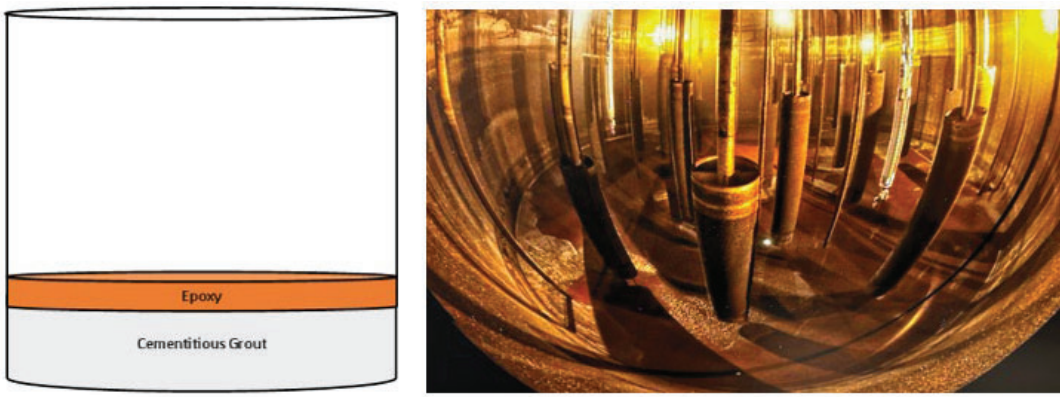

Figure 1 On the left is an illustration of the two layer approach and on the right is a panoramic photo of tank AY102, a DST, after extensive cleaning.

The majority of those columns seen on the right of **Figure 1** are Air Lift Circulators (ALC) that were used to cool down radioactive liquid waste. They were effective in cooling stored liquid waste by injecting air at the bottom of the ALC which reduced the density of the waste in the barrel of the ALC. The denser

solution outside the ALC flows in, lifting the lighter mixture of air and waste out the open top. The ALC columns do not reach the bottom of the tank but are suspended 30 inches (2.5 ft) from the tank floor. These ALCs should not interfere with spread of the grout and epoxy layers since the combination of the two layers will not exceed 18 inch thickness (1.5 ft).

The reasons for going to a two layer approach are the following:

- Pouring an initial grout layer would provide a fresh surface for a subsequent second layer of polymer to adhere to. The grout layer would contain cement as the only binder material in the grout (no added polymer binder). Epoxy was chosen as the second sealing layer due to superior radiation resistance and adhesion properties in comparison to other polymers. [7], [8] Epoxies are commonly used as coatings or sealants for cement and concrete.
- There was considerable concern about how to prepare the surface of the decades-old carbon steel tank bottom to ensure proper adhesion of a single-layer repair, regardless of whether a cement/polymer mix or a pure polymer was used. Surface inspection and preparation are important for adhesion when considering refurbishment of a tank bottom. Some level of adhesion is required to prevent leakage. Inspection of the bottom surface of an emptied waste tank would likely need to be done robotically to ensure As Low As Reasonably Attainable (ALARA) rad conditions. In the two layer approach there is less concern with adhesion of epoxy to the bottom since it will be adhering to a fresh layer of grout. If residual moisture remains on the original carbon steel tank bottom after cleaning, it will be incorporated into the grout during its hydration and hardening. Any residual radiation will be shielded by the grout, protecting the subsequent epoxy layer. Other contaminants that could interfere with adhesion will also be covered by the grout. After the grout hardens, it creates a new, clean surface for sealing with a second epoxy layer. The sealing occurs at the interface between the grout and the epoxy, not at the interface between the old steel tank bottom and a single repair layer.
- There was concern that a single layer composed of epoxy/cement/aggregate or epoxy/aggregate would result in a product that would not provide sufficient flow to cover the tank bottom surface when applied. Two of the epoxy/aggregate materials were evaluated early on in Year 1 of this project and resulted in very low flow properties and segregation of aggregate when higher levels of epoxy were used to improve flow [6] [9] . It seemed that the addition of cement to the epoxy/aggregate products tested would only exacerbate this flow issue.
- There was a concern with adhesion to the steel tank bottom due to permeation of aqueous based tank waste through a single layer of grout even if hydrophilic polymer was mixed into the grout at some level greater than 5%. According to the literature, even pure epoxy will take up about 3% moisture, but this was considered to be lower than what could be expected from a grout that was a combination of cement and polymer. [25] [26] The presence of moisture at a bond interface is known to reduce adhesion.
- Epoxy is not as resistant to degradation from radiation as cementitious grout, however, Hanford Tank Waste Operations and Closure (H2C, formerly WRPS or Washington River Protection Solutions) stipulated that the tank waste that would be stored in a refurbished tank

would have extremely low radiation levels of no higher than 0.175 mCi/L due to removal of Cs-137. Because of this expected very low level of radiation it was decided that radiation degradation of a separate epoxy layer would be less of an issue than permeation of low level radioactive aqueous waste through a cement/epoxy polymer grout layer. Epoxies are one of the most radiation resistant polymers, second only to polyimides. [8] One of the goals of this work was to determine an estimate for service life of the epoxy layer in an environment of Hanford tank simulant.

The original proposal discussed using design of experiment (doe) to determine an optimum formulation for a polymer modified cement that included input variables of types and amounts of components like base polymer, aggregates, and cement to water ratios. Output variables of a doe like this would include change in viscosity during cure, final compression strength, final adhesive strength, % uptake of tank simulant after soaking, etc. The further we proceeded through this project it was determined that construction of a doe like this would be a huge undertaking for the two layered approach requiring large amounts of time and resources. In addition, early in Year 1 WRPS shared results from testing done with AVANTech using a room temperature, slow cure epoxy with no cement or aggregate, that showed very promising properties such as no cracking during cure when poured in a mold 48” x 48” at a 2” inch thickness of epoxy as well as no gap or shrinkage observed at the mold wall. [7]

While undergoing initial experiments during year 1 with other epoxies [6], [9] SRNL started to pursue a non-disclosure agreement (NDA) with AVANTech to evaluate this formulated epoxy that showed promising results. The NDA was signed at the start of Year 2 and the formulation was received soon after on April 8, 2025. This epoxy will be referred to as the NDA Epoxy in the rest of this report. It was decided to put off the doe formulation work to a later date if needed and move forward with characterizing the NDA Epoxy.

While evaluating this NDA Epoxy in Year 2, it was decided that this material appeared to be adequate for the purposes of this application. The reasons for this are the following: it has a Tg of 52 °C, which is greater than twenty degrees above the maximum storage temperature of 27 °C; the compression strength of a fully cured sample has a yield stress that should adequately resist any hydrostatic pressure from the tank waste over time; it appears to bond very well with grout which will be used to cover the tank floor before pouring the epoxy sealant layer; a long plastic deformation plateau region in the stress/strain curve of the epoxy indicates the NDA epoxy would be able to withstand residual stresses created during material expansion at the point of maximum heat/temperature of cure. Many formulated epoxies do not have these kinds of plateau regions and will crack or fail at significantly lower strains. Cracking occurred on the other epoxy that was studied in the WRPS/AVANTech “Depth Test” [7]. The results of testing these critical properties mentioned in this paragraph are summarized in this report.

When the funding for 1.5 years of the project began to get depleted there were plans to run heat transfer experiments and a scale up for the two layer approach in an 8 foot diameter tank in the second half of Year 2 and Year 3. These were not pursued due to the lack of funds and announcement of a pause in work on all Lab 23 EM001 projects at the end of March 2026 with redirection of the anticipated funding slated for the second half of Year 2 and Year 3. The plans for heat transfer experiments and scaling up are discussed in greater detail in section 2.4.

Over the course of Year 1 and Year 2 service conditions and desirable properties for the grout and epoxy layer were identified (See Appendix A and Appendix B). These are not exhaustive and can be refined as this research is continued. Service conditions identified by H2C are given below. [10]

- Tank Waste temperature: 16-27^{O} C (60-80^{O} F)
- Temperature of Tank Bottom during application/pumping of grout and epoxy layers:
  - Below ground temperature stabilizes at a constant 9 – 13^{O} C (48-55^{O}F) at depths of 6ft. (via Google AI)
- Maximum radiation level of liquid waste: 0.175 mCi/L
  - Tank waste returned to a refurbished DST will be low activity waste where 99.9% of the Cs-137 has been removed. The Cs-137 concentration will be no higher than 0.175 mCi/L.
- Alkalinity of tank waste solution: 4% NaOH (1 M, pH=14)
- Focus is on "refurbishment" not "repair"
  - Refurbishment – to enhance the longevity of a tank prior to a through wall penetration, for example, when thinning of the tank bottom has been identified.
  - Repair – to fix something that is no longer usable, for example, patch a tank *after* a through wall penetration has been identified
    - Repair requires approval by an Independent Qualified Registered Professional Engineer (IQRPE).

Desirable properties of the epoxy and grout layers are given in Appendix A and Appendix B. A great deal of effort and consideration throughout this project was spent on determining these properties and can be considered one of the more successful outcomes of this effort. Close inspection of these Tables and understanding of the Reasons/Comments shown will give researchers a headstart if and when this research gets restarted.

2.0 Delivery of Year 2 Milestones

2.1 Evaluation of Cementitious Grout

2.1.1 Criteria for Using Cementitious Grouts in Tank Refurbishment

Table 10 in Appendix B lists the criteria for using cementitious grout for the tank refurbishment application [11]. To achieve the pumpability and flowability requirements for use inside a waste tank, the grout should exhibit a flow testing greater than 24 in. [12] [13], per American Society of Testing and Materials (ASTM) C1611 protocol. Additional critical criteria for the tank refurbishment application per **Table 10** includes no bleed or segregation, low shrinkage, and chemical durability, which will be discussed further in this report. Adhesion to steel was briefly investigated. Grouts adhere to steel qualitatively, but standard pull off adhesion testers do not work on steel/grout mixes due to weak cohesive strength of the grout [11], and a specialized setup would be necessary to further evaluate this. Permeability (hydraulic conductivity) was not included in **Table 10** for two reasons: 1) if epoxy sealants

are used over the grout, the epoxy would be impermeable, and 2) the permeability values of related cementitious grouts (1.3*10-8 cm/s [14]) are considered “impervious” materials by definition [15]. In addition, epoxy to grout adhesion is important and this is addressed in section 2.2 Evaluation of NDA Epoxy.

2.1.2 Materials and Methods

The grouts studied in this work include the following information. Further details on Grouts A-D can be found in [11].

- Grouts A and B were based on commercially available prepackaged non-shrink grouts. They contain fine aggregate in addition to Portland cement, pozzolans, and processing admixtures. They were modified with additional commercial liquid admixtures to obtain the desired fresh properties. The water to premix ratio was in the range of 0.18-0.20.
- Grouts C and D were updated mix designs for Savannah River Site (SRS) that were used for closing reactors and eight SRS one-million-gallon high level waste tanks. [13] [16]. The mix design is included in ref [11]. They contain Type IL Portland cement, Class F Fly Ash, ASTM C33 concrete sand, ASTM #8 granite aggregate, along with commercial high range water reducers (HRWR) and viscosity modifying admixtures (VMA) to obtain the desired fresh properties. Grout D does not contain gravel and has additional sand. The water/cement ratio of Grouts C and D are higher than A and B (0.73-0.76 for C and D respectively). Ingredients available at SRS were used in this proof of concept evaluation. If either Mix C or D is selected for further evaluation then mixes containing pozzolan, sand, and gravel available in Richland WA would need to be tested.

Grouts A, B, C and D were prepared using a Hobart planetary mixer to create several 0.5 cu ft batches for fresh and cured property testing using ASTM methods. Initial flow measurements were determined by both ASTM C1611 and ASTM D6103. ASTM D6103 was used for static and dynamic flow testing. Static flow means that the cylinder for the ASTM D6103 test was filled and left to sit undisturbed for 90 min, after which the cylinder was pulled and the flow measured. Dynamic flow means the mix was continuously mixed for 90 min, after which the cylinder for flow was prepared and then the flow measured. 90 min represents an upper limit for how long the grout processing could take, considering steps of batching and mixing, delivering the grout in a ready-mix truck, pumping the grout from the truck into the tank, and then letting the grout flow inside the tank. It also considers worse case scenarios such as mixer or pump failures in the process, i.e. a process upset.

A subset of grouts was chosen for chemical durability testing. Cut grout disks of ≈1 in. thick by ≈2 in. diameter (cured at least 28 days) were placed into Teflon jars filled with either deionized water or simulant solution of Hanford tank waste and loosely capped. The samples rested on a Teflon scaffold. The amount of solution was 2-3X the weight of the sample. The simulant recipe was provided to the authors from H2C. [17] Samples were either at ambient temperatures (22-25°C) or placed in an oven at 60°C to accelerate the aging effects. Samples were periodically removed from their solutions to evaluate any changes or degradation over time. Excess surface water or solution was dried by patting with a towel.

2.1.3 Fresh Properties

Figure 2 shows the ASTM C1611 slump flow test of each mix A, B, C, and D. Visually they show no bleed or segregation [11]. **Table 1** shows the flowability measurements for mixes A, B, C, and D. The commercial grouts A and B were fluid and exceeded the dimensions of the board per ASTM C1611 (see **Figure 2**A and 2B). The reactor closure grouts C and D exhibited flowable behavior. Per dynamic and static flows using the D6103 test, the flowability of all mixes decreased with long mixing times, except for Grout A which when continuously mixed had improved flow. Pictures of the flows from static and dynamic testing are shown in **Table 2**. Grout A completely lost its flowability after remaining static for 90 minutes. Grouts C and D began to show signs of mounding after 90 minutes. It's important to note that the 90-minute duration used in both static and dynamic tests represent a worst-case scenario. In most situations, mixing and placement would be completed well before 90 minutes, without any process interruptions. Ultimately, the change in flowability of the mixes after extended mixing or static periods needs to be evaluated at a larger engineering scale to determine how much it may impact remote placement applications. It is also important to note that all grout design mixes set within 24 hours. Additional fresh property data is included in [11].

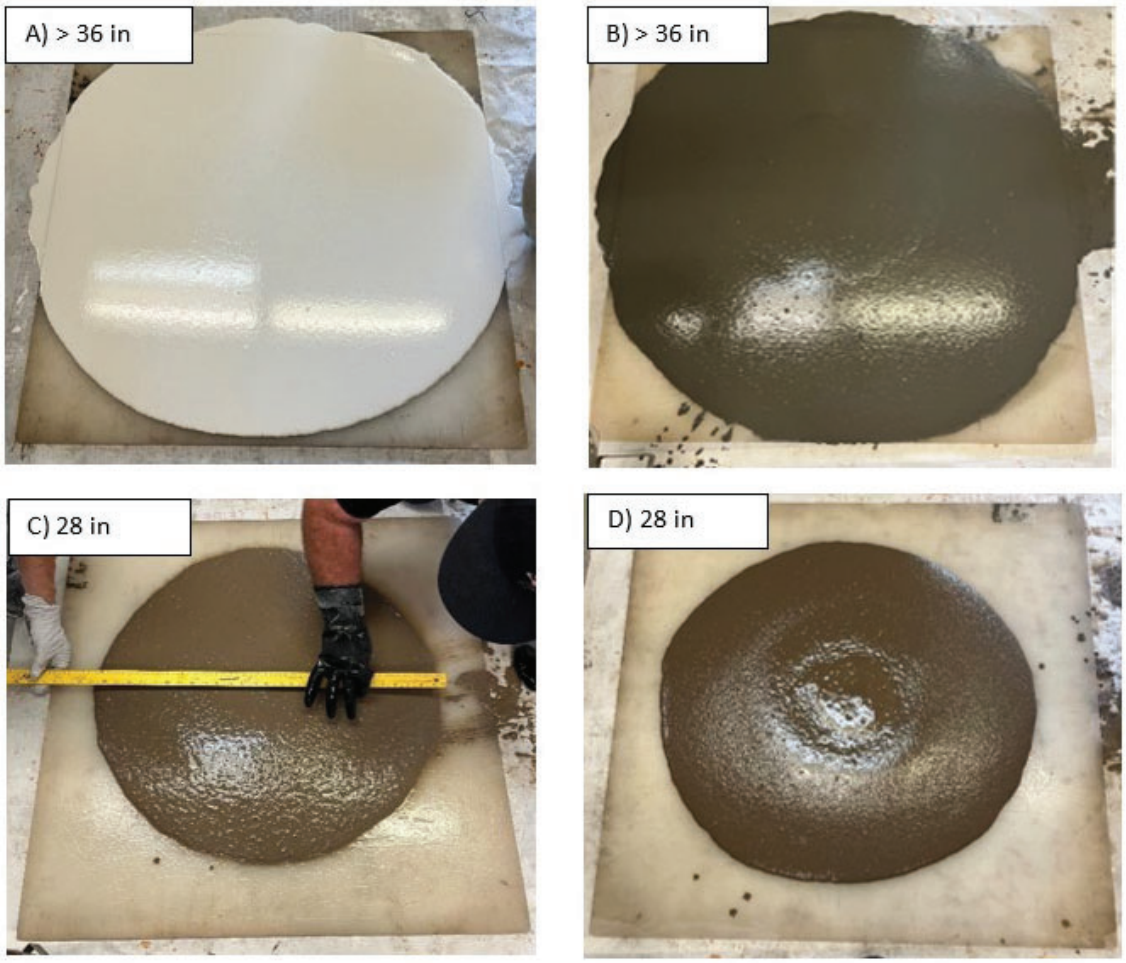

Figure 2. Slump flow by ASTM C1611, for A) Grout A, B) Grout B, C) Grout C, D) Grout D

Table 1. Flowability Data of the Mixes [11].

Properties	Grout A	Grout B	Grout C	Grout D
Flow (in) ASTM C1611	> 36	> 36	28	28
Flow (in) ASTM D6103	19	17	11	11
Static Flow after 90 min (in) ASTM D6103	No flow	13	10	8
Dynamic Flow after 90 min (in) ASTM D6103	20	14	9	8

Table 2. Flows at Initial, and Static and Dynamic conditions after 90 min. Scale bar is 10 in [11].

Formulation	Initial	Static Flow after 90 min	Dynamic Flow after 90 min
Grout A			
Grout B		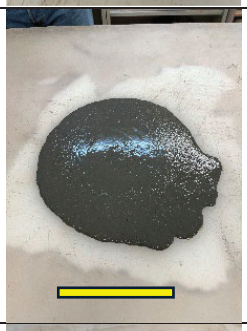	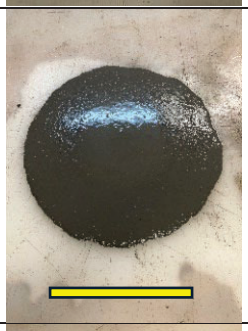
Grout C			
Grout D		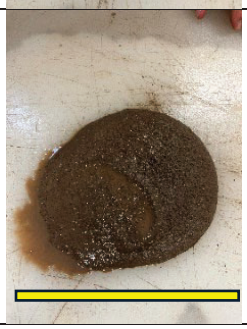	

2.1.4 Cured Properties

Table 3 shows cured properties of the mixes. The commercial grouts A and B are an order of magnitude stronger than the Reactor Closure based grouts C and D, even at 7 days of curing. The strengths of all grouts would still be acceptable for the tank refurbishment application (note grouts for SRS reactor closure grouts required compressive strengths of only 50 psi [13], and the hydrostatic pressure of tank waste would be approximately 15 psi). Grouts A and B exhibited a larger magnitude of shrinkage

(negative values in length of change indicate shrinkage) perhaps due to no added aggregate in the commercial mixes, i.e. they only contain fine aggregates. Additional cured properties were similar [11]:

- Densities between 2.11 – 2.17 g/cm3
- Porosities between 21 – 28 %

Table 3. Cured Property Data of the Mixes.

Properties	Number of Days	Grout A	Grout B	Grout C	Grout D
Compressive Strength (psi) ASTM C39	7	9,000	6,800	210	250
	28	13,300	8,700	570	570
Length of Change (%) ASTM C157	7*	-0.12	-0.14	-0.04	-0.05

*Length of change measurements beyond 7 days gave less than 0.03% change in length for all samples.

The cured properties for Grouts A through D are acceptable for tank refurbishment. They should be evaluated at larger scale, especially to determine if shrinkage would cause the grout to pull back from the tank walls, leaving a gap on the sides in which tank waste could enter, or crack in other areas of the false bottom grout.

2.1.5 Chemical Durability

Grouts A and B were selected for chemical durability testing due to their overall better fresh and cured properties for the tank refurbishment application. Additional types of commercial or ultra-high performance grouts were also provided to the authors for chemical durability evaluation (fresh and cured properties not evaluated in this work). All the grouts that were studied for chemical durability demonstrated similar phenomena that will be described in the upcoming paragraphs.

Table 4 shows Grout A samples after exposure to various conditions for 389 days. The grouts do not have any visual signs of cracking. However, for samples in simulant and 60°C, the accelerated case, there is discoloration of the sample. The surrounding simulant solution is also discolored (initial solution is clear), especially obvious for Grout B, which is shown in **Figure 3**. This suggests the grouts are leaching particles into the simulant. Note that these color changes can occur within 2 months (56 days) for 60°C samples [11].

Table 4. Pictures of Grout A After Exposure to Various Conditions (samples were immersed for 389 days, discs are 2 in. diameter).

Temperature (°C)	Air	DI Water	Simulant
25	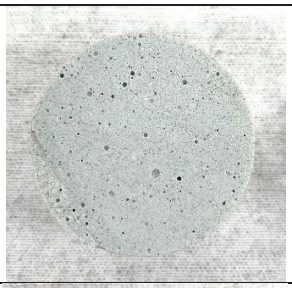		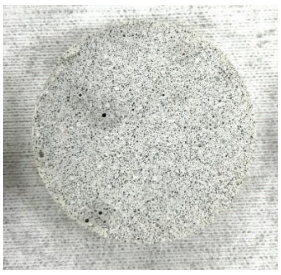
60	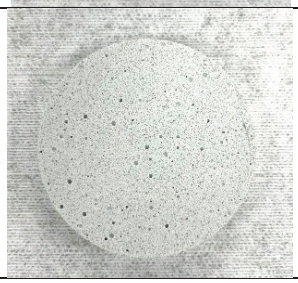	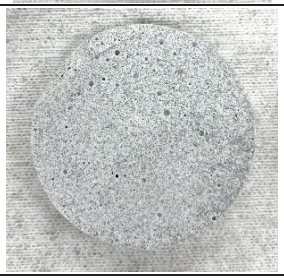	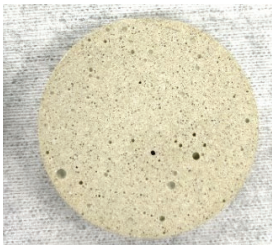

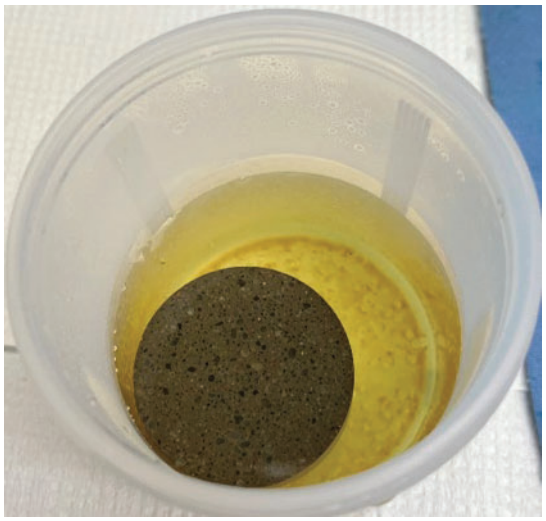

Figure 3. Grout B Sample After 60°C Immersion in Simulant for 227 Days.

The grout samples in solution are also gaining weight over time. **Figure 4** shows the percent change of weight over time for Grout A, where positive percentages indicate weight increase. **Figure 4A** is in simulant and **Figure 4B** is in DI water.

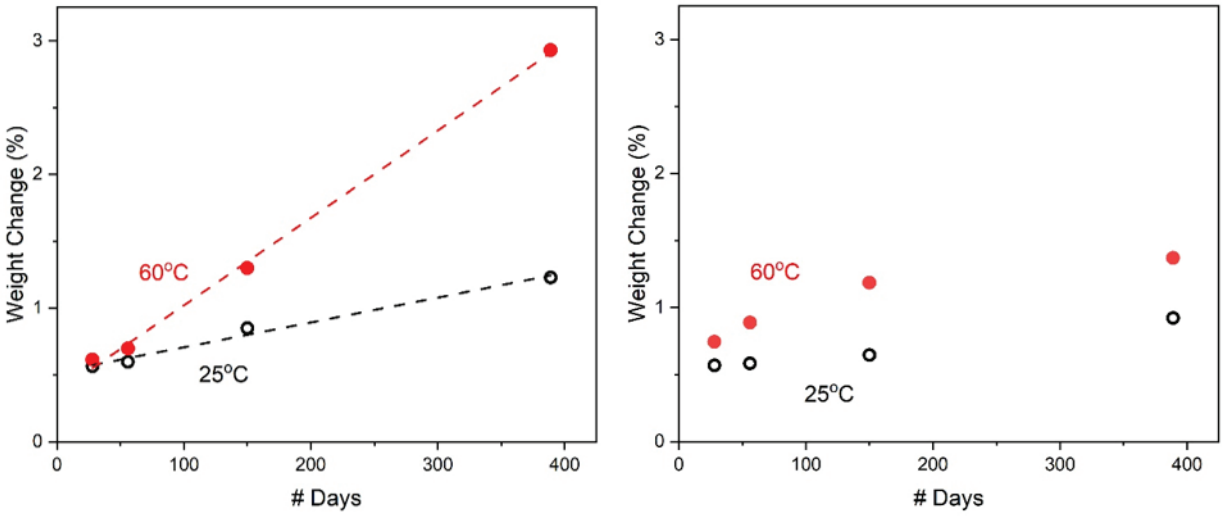

Figure 4. Weight Change Over Time for Grout A Samples in A) Simulant, B) DI Water.

Beyond 28 days (first data point), the slope of the samples vary depending on the condition. Samples in simulant have a linear increase in weight over the duration of the time studied. Because of the linearity between the two slopes, the degradation rate is assumed to be proportional to temperature in the studied range. The ratio of slopes between 60°C and 25°C for all grout samples studied is between 3 and 5. Thus the 60°C samples are degrading at a rate 3-5 times faster than at ambient conditions, and thus it is a prediction of the grout appearance and properties 3-5 years after initial exposure to tank waste simulant. As for samples in DI water, at 60°C the shape is logarithmic, whereas the ambient 25°C sample has a small linear slope. A consideration is that grout samples when immersed in water may leach $Ca(OH)_2$, which may influence the weight increases/decreases. This is potentially supported by pH measurements of grout samples in DI water being between 9-11 after 28 days immersion (not shown here). On the other hand, the pH of grout samples in simulant had no change over 56 days (not shown here). Note for samples in simulant, it is possible that some of the sodium species from the simulant may be absorbed into the grout as well.

In the beginning of immersion testing (before 28 days), all samples whether in simulant or in DI water have a similar increase in weight per **Figure 4**. Thus, the weight increase of the grout samples in immersion can be partially due to water absorption. This is expected, as water fills the permeable pores in the grout. Furthermore, in a separate immersion experiment using similar Grout A samples, weight increases were between 0.2 to 1.0% within just 1 hour of exposure to the solution (not shown here). After 1 hour, the weight increase continues but at a slower rate. The range in values for the weight increase in this experiment is likely due to the starting condition of the grout; the drier the sample, the more increase in weight from water absorption is possible. The samples in this separate study had been left in a bag months after initial mixing, so they were likely drier than the majority of samples studied previously.

From the results of the chemical durability testing, it is hypothesized that upon initial exposure to the tank waste, water will immediately and continuously fill open pores, leading to a sharp initial weight increase. If the cementitious grouts were immersed in water only, the weight would continue to increase until all the permeable pores are filled, and this appears to take more than a year at ambient

conditions. It is known, however, that $Ca(OH)_2$ can leach from cement when immersed in water and this could be happening at the same time as pore filling. On the other hand, with tank waste simulant, there appears to be a reaction in which species are continuously entering the grout and other species are being removed from the grout. This leads to a net increase in weight as well as a color change for the sample and simulant. Perhaps the simulant causes changes in the pore structure of the grout as well, allowing for more pathways for species to enter, and thus mass increase. Higher temperature (60°C in this work) accelerates all the effects listed in this paragraph. Fortunately, exposure to tank waste simulant does not lead to large cracks in the cementitious grout for the duration studied, estimated from the slopes in **Figure 4** and additional samples to be between 3-5 years.

To further understand these changes, additional experimentation and characterization would have to be performed. One aspect to consider is for the chemical durability testing performed in this work the grout samples were exposed to solution on all sides of the grout, whereas in the actual application only the top surface would be exposed. Thus, it is possible the degradation mechanisms or extent of degradation may be different for the two experimental setups. Ultimately, chemical durability of grout samples coated with epoxy should be tested as well. While the epoxy may absorb water too, the epoxy may enhance the durability by preventing the potential leaching of the grout into the simulant (i.e. tank waste) and absorption of species into the grout.

2.2 Evaluation of NDA Epoxy

2.2.1 Processing Properties Evaluation

The NDA Epoxy showed a great deal of improvement in workability time over the best epoxy candidate found by SRNL. Epoxies that start with a low viscosity, are cured at room temperature, and have a long cure time are difficult to find; it appears that this epoxy from AVANTech was formulated just for this purpose. Isothermal cure curves at 30 °C for the best candidate from SRNL and the NDA Epoxy are shown in **Figure 5**. The graph shows that the NDA Epoxy took much longer to reach a viscosity of 2,000 mPa-sec than the SRNL Epoxy, 135 min and 6 minutes respectively. In addition, an additional Jeffamine curative was identified that was different from the curatives used in the original NDA formulation and SRNL formulation. When used in combination with the original part A epoxies of each at a 3:1 epoxy:curative ratio the result was even longer cure times, as shown in **Figure 5**. Two thousand mPa-sec viscosity was chosen as an arbitrary measure of when flow would stop; as reference honey is reported to have viscosities in the range of 2,000 to 10,000 mPa-sec.

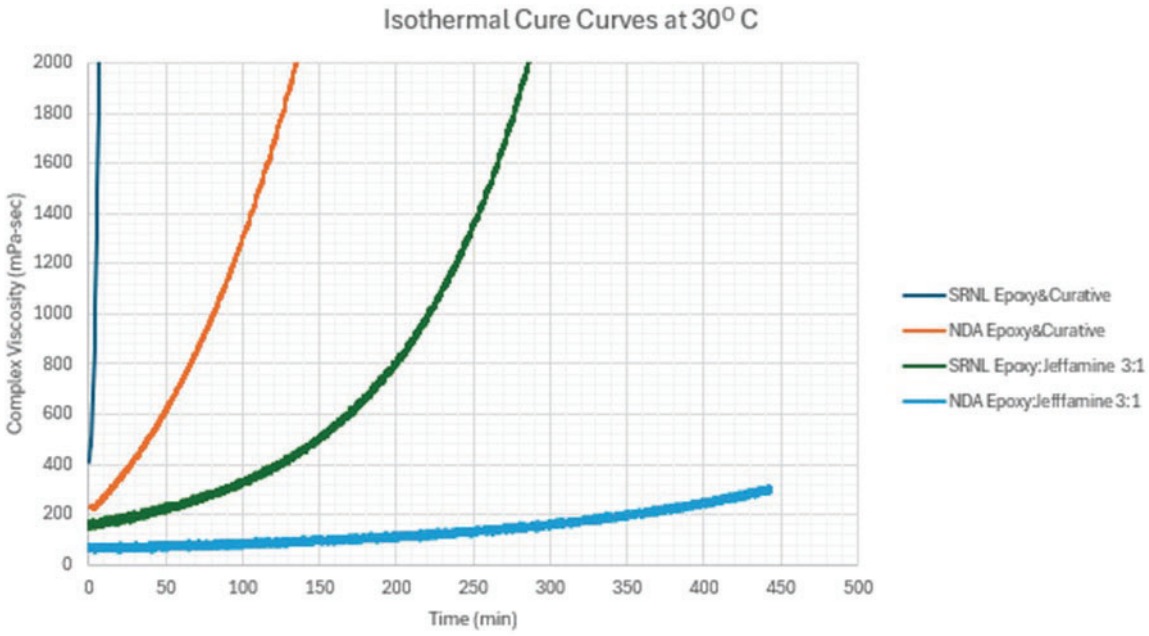

Figure 5. Isothermal cure curves of SRNL and NDA Epoxies with usual curative and Jeffamine curative.

2.2.2 Final Physical Properties Testing

Further testing of the NDA Epoxy was started on properties that were decided to be critical for this application. These include Glass Transition Temperature (Tg, ASTM D3418 by Differential Scanning Calorimetry, DSC, and E1640 by Dynamic Mechanical Analysis, DMA), Compression Stress/Strain Curves (ASTM D695), Adhesion Strength (ASTM D7234), and Changes in Sample Dimensions (weights and lengths). These properties were to be tested on samples as they are removed from accelerated aging conditions during this project. A significant portion of the latter half of Year 1 and the first half of Year 2 was dedicated to selecting, developing, and implementing these test methodologies at SRNL.

Figure 6 shows results of tested Tg versus Days at Room Temperature Cure, **Figure 7** shows Compression Stress/Strain Curves for samples that were tested after 14, 28 and 56 days of room temperature cure, and **Figure 8** shows the Pull Up Pressure plots for Adhesion Testing and failure surfaces of the Pull Up fixtures. **Table 5** shows numerical values for Tg and Compression Testing and **Table 6** shows results for Pull Up Adhesion Strength for epoxy poured and then cured onto grout after 28 days at room temperature. As mentioned in the Introduction, the NDA epoxy formulation was received in the first week of Year 2, early April 2025. All testing occurred in the first 6 months of Year 2 or up until funding started being withheld for the second half of Year 2, this began the first week of October 2025.

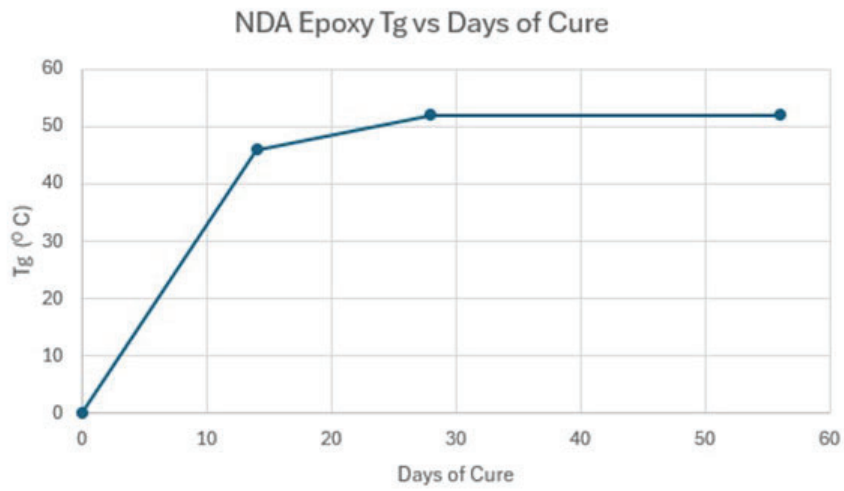

Figure 6. Tg vs Days of Cure for NDA Epoxy.

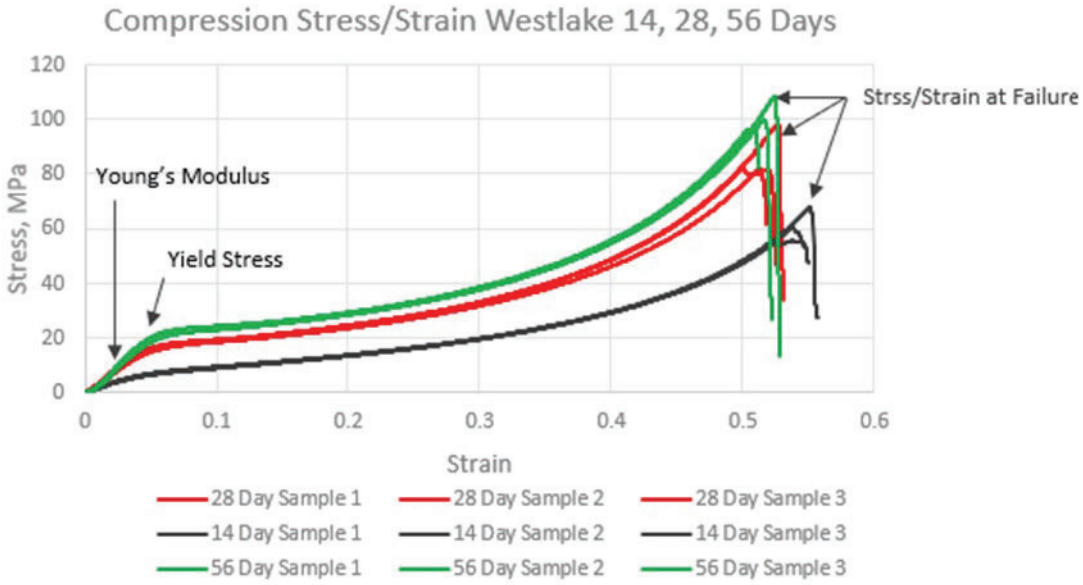

Figure 7. Stress Strain Curves for NDA Epoxy after 14, 28 , and 56 days of cure.

Table 5. Results from Tg and Compression Testing.

Days Cured or Aged	T_g (°C)		Yield Stress (MPa)		Young's Modulus (MPa)		Strain at Failure		Stress at Failure (MPa)	
	avg	st dev	avg	st dev	avg	st dev	avg	st dev	avg	st dev
14	46	3.8	4	0.4	143	8	0.551	0.004	62	5
28	52	2.2	13	1.1	364	31	0.525	0.006	88	8
56	52	3.0	18	0.1	459	21	0.520	0.008	101	5

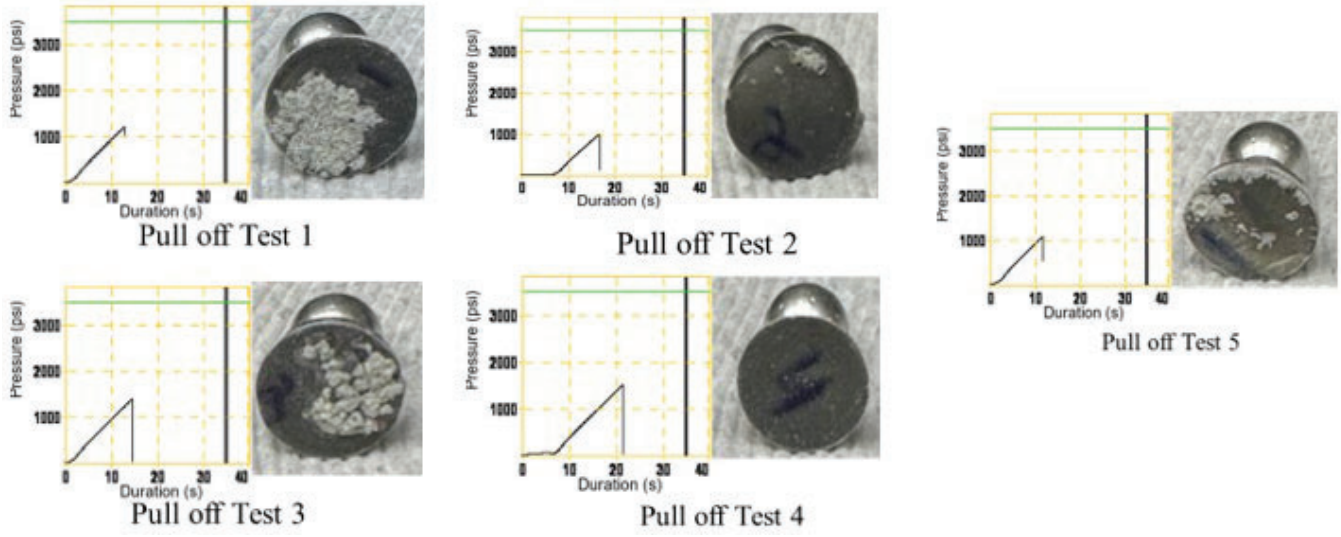

Figure 8. Bottom of Adhesion Pull Up Test Fixtures showing modes of Failure.

Table 6. Results of Pull Up Pressure and Type of Failure.

Sample #	Pull Up Pressure (psi)	Type of Failure
1	1249	Grout Cohesive, Epoxy Cohesive
2	1026	Grout Cohesive, Mostly Epoxy Cohesive
3	1425	Grout Cohesive, Epoxy Cohesive
4	1546	Epoxy Adhesive Failure to Grout
5	1117	Grout Cohesive, Epoxy Cohesive
avg	1227	
st dev	192	
NDA Epoxy to Steel	808 (average)	Primarily Epoxy Cohesive Failure

2.3 Expectations for Physical Properties

2.3.1 Glass Transition Temperature, Tg

The expected range for tank waste temperature in the DST tanks is between 16 – 27 °C (60 – 80 °F). Therefore, the expected glass transition temperature (Tg) for the epoxy sealant layer has been set at 50 °C or higher, this is twenty degrees or more above the maximum storage temperature. During storage of tank waste, the epoxy layer must be in the glassy state, therefore, Tg must be set above the maximum storage temperature. Degradation will be slower when the epoxy is in the glassy state or at

temperatures below Tg. Molecular motion is greater above Tg, free space or free volume in the polymer is greater, and degradation occurs more readily.

Over the course of determining Tg during room temperature cure of the NDA Epoxy over 56 days it was occasionally very difficult to discern where the second order transition or step change in Heat Capacity or Heat Flow occurs in the DSC traces. An example of this is shown in **Figure 9**. The DSC scan in the top graph is for sample WL-A (the NDA epoxy) after 14 days of cure. The two lower scans are the same scan on the same sample as the top scan but tested after 28 days of cure. The scans on the bottom show a much fainter step change in Heat Flow around 54 ^{O}C (28 days of cure) than the step change at 49 ^{O}C (14 days of cure). The top scan and bottom right scan also demonstrate how Tg is determined in ASTM D3418 by finding the center point of the transition. Glass transition is considered a second order material transition in that it occurs over a range of temperatures; there is no abrupt change that occurs at a specific temperature as in first order transitions. For example, boiling point is a first order transition and it occurs at a specific temperature, for water at standard temperature and pressure it is 100 ^{O}C. This faint baseline change in Heat Flow vs Temperature is not uncommon for rigid polymers like epoxies. As the epoxy continues to cure at room temperature the crosslink density increases (raising Tg) making the polymer more rigid.

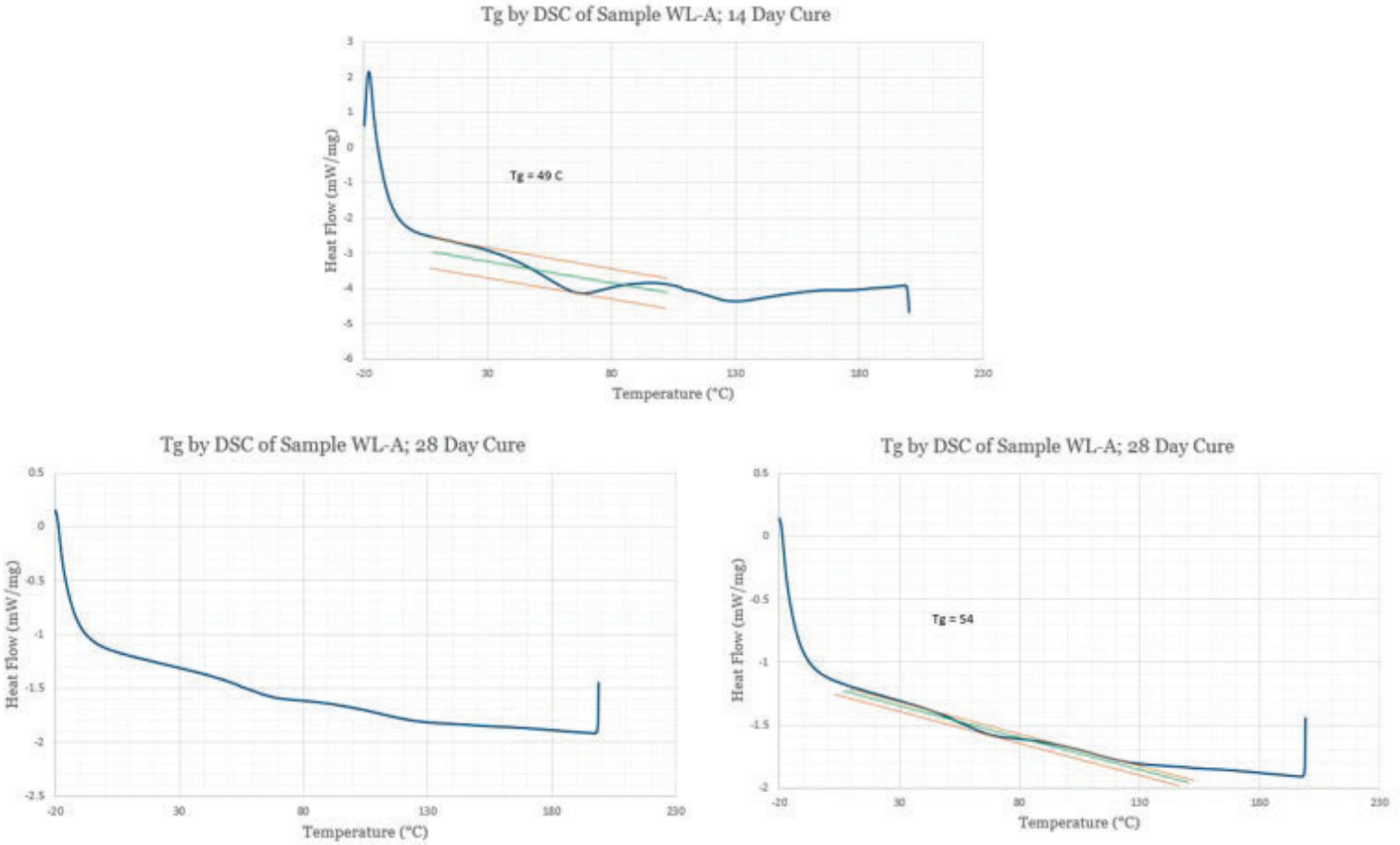

Figure 9. DSC scans on the same sample after 14 days and 28 days of cure.

Instead of running into future difficulties in determining Tg using DSC in subsequent testing as samples are removed during accelerated aging it was decided to switch measuring methods to determining Tg by DMA (ASTM E1640). Tg is measured using DMA by placing a sinusoidal strain on a sample and measuring the subsequent stress from the DMA instrument load cell as temperature is ramped in the instrument environmental chamber. Strain is accurately measured using a Linear Variable Differential Transducer (LVDT) on the DMA instrument. These are converted to values of Storage Modulus (G'), Loss Modulus (G"), and tan δ (= G"/G'). DMA measures the mechanical relaxation of the sample to an oscillating force to determine Tg versus measuring Heat Flow changes by DSC. DMA uses the temperature at the peak of tan δ as Tg, this is outlined in ASTM E1640 and shown in **Figure 10**. In general, determining Tg using tan δ peak by DMA is about 10 to 25 ^{O}C higher than Tg measured by DSC. The DMA method is preferred because the tan δ peak will be easier to determine versus determining a faint transition in the DSC curve as illustrated in **Figure 9** and **Figure 10.**

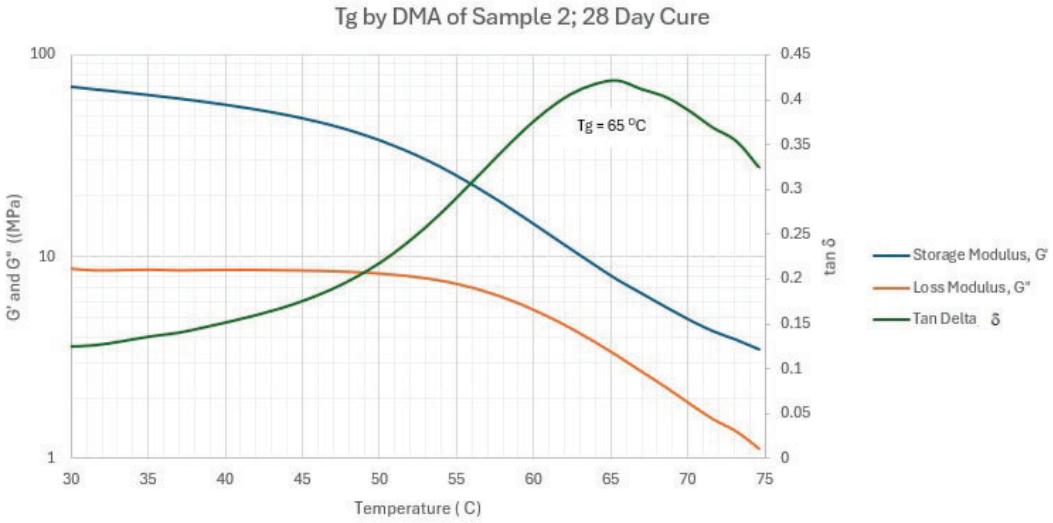

Figure 10. DMA curve generated from a sample of the NDA Epoxy after 28 days of cure.

2.3.2 Compressive Strength

An initial experiment was done on one compression sample where a cylinder which saw a cure time of 56 days at room temperature was placed in an oven at 150 °C for 30 days and the stress strain curve was plotted against samples from **Figure 7**, this is shown in **Figure 11** below. 150 °C was chosen somewhat arbitrarily for this quick experiment and may be higher than where the maximum storage temperature for Time Temperature Superposition (TTS) aging will be set at, as explained later in section 2.3.5.

It does not appear that there is any degradation of the stress/strain curve at low strains, however, there is an observable drop in the strain and stress at failure, as indicated in **Figure 11** by the blue arrow and **Table 7**. The hydrostatic pressure from 30 ft. of tank waste above the epoxy layer applies a force of only 0.10 MPa (15 psi) during service, therefore, the epoxy layer will not see much stress during waste storage. It appears that observation of compressive strength degradation during accelerated aging would best be done by following stress at failure which shows a significant drop-off after 1 month at 150 ^{O}C. For TTS accelerated aging, all aging temperatures should occur below Tg so the maximum aging

temperature is constrained by Tg. It would be worthwhile to do accelerated aging both above and below Tg and some conservative estimations could be made. This is discussed in section 2.3.5.

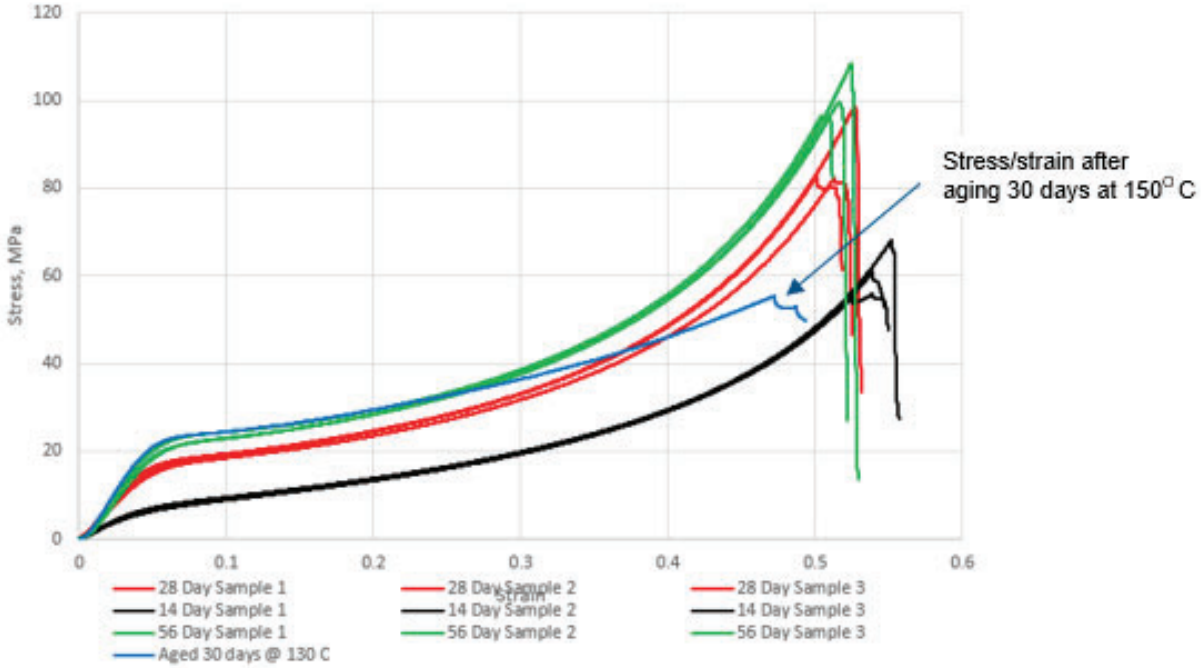

Figure 11. Compression test of a cylinder cured for over 56 days and then aged for 30 days at 150O C. See blue curve.

Table 7. Comparison of Table 1 properties (Tg and Compression) to test sample aged at 150 °C for 30 days after cure

Days Cured or Aged	T_g (^{O}C)		Yield Stress (MPa)		Young's Modulus (MPa)		Strain at Failure		Stress at Failure (MPa)	
	avg	st dev	avg	st dev	avg	st dev	avg	st dev	avg	st dev
14	46	3.8	4	0.4	143	8	0.551	0.004	62	5
28	52	2.2	13	1.1	364	31	0.525	0.006	88	8
56	52	3.0	18	0.1	459	21	0.520	0.008	101	5
30 days @150^O C	TBD		23		501		0.47		55	

2.3.3 Adhesion Strength

The adhesion results from **Table 6** show the distribution and type of failures to expect on unaged samples after allowing a 0.125" layer of NDA epoxy to cure for 28 days at room temperature. The average pull up strength is 1227 psi and the standard deviation is 192 psi. Ideally the adhesion between epoxy and grout would be strong enough that all failure would occur in the grout layer. Typical pull up strength values for epoxy to concrete are in the 300 to 500 psi range and failure is usually cohesive failure within the concrete. [18] In **Figure 8** we see that failure is predominantly cohesive in both the epoxy and the grout. This indicates that the grout used is of high strength and the NDA epoxy used is in general of lower strength. Cohesive strength values for epoxy are generally quantified by tensile strength which is in the 5,000 to 12,000 psi range. [19] It appears that the adhesive strength between this grout and the NDA epoxy is at or above the cohesive strength of both grout and epoxy.

2.3.4 Dimensional Changes

The same sample that was placed in the oven at 150 ^{O}C and compression tested after 30 days was also periodically measured for diameter, length, and weight changes over those 30 days. The results are shown in **Table 8** and graphed in **Figure 12** and **Figure 13.** This would be the same dimensional testing that would occur during accelerated aging experiments. At this time, it is believed that the maximum accelerated aging condition will be less than 150 °C and it is believed that the epoxy sealant layer will not shrink as much as indicated at 150 °C.

Table 8. Shrinkage and Weight Loss of Compression Cylinder Over 31 Days at 150 °C

Time (hours)	Diameter Changes at 150^{O} C			Length Changes at 150^{O} C			Weight Changes at 150^{O} C		
	Diameter (in)	Shrinkage (in)	%Change in Diameter	Length (in)	Shrinkage (in)	%Change in Length	Weight (gms)	Change in Weight (gms)	%Change in Weight
0	0.494	0	0.00%	0.976	0.000	0.00%	-	-	-
2	0.493	-0.001	-0.20%	0.975	-0.001	-0.10%	-	-	-
24	0.491	-0.003	-0.61%	0.971	-0.005	-0.51%	3.2120	0.0000	0.00%
50	0.490	-0.004	-0.81%	0.970	-0.006	-0.61%	3.1949	-0.0171	-0.53%
194	0.487	-0.007	-1.42%	0.969	-0.007	-0.72%	3.1458	-0.0662	-2.06%
359	0.484	-0.010	-2.02%	0.966	-0.010	-1.02%	3.1144	-0.0976	-3.04%
744	0.481	-0.013	-2.63%	0.963	-0.013	-1.33%	3.0672	-0.1448	-4.51%

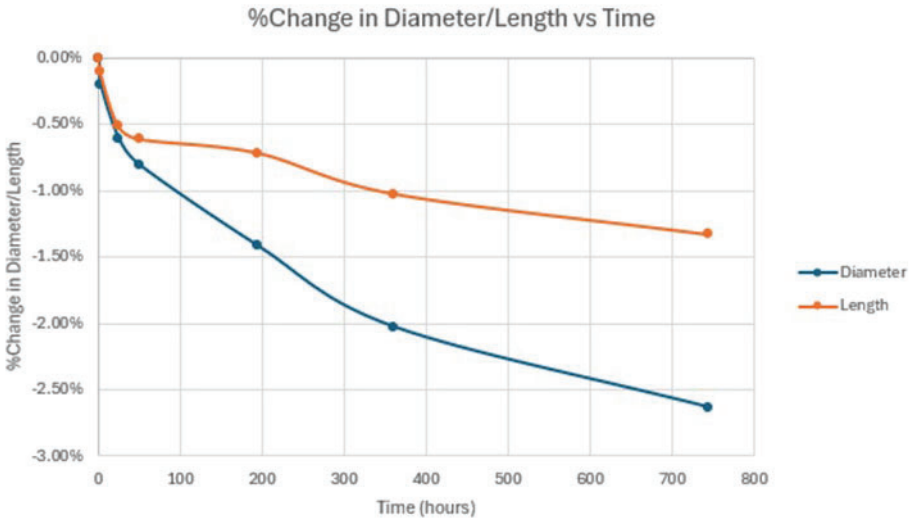

Figure 12. %Change in Diameter and Length of Compression Cylinder after 31 days at 150 °C.

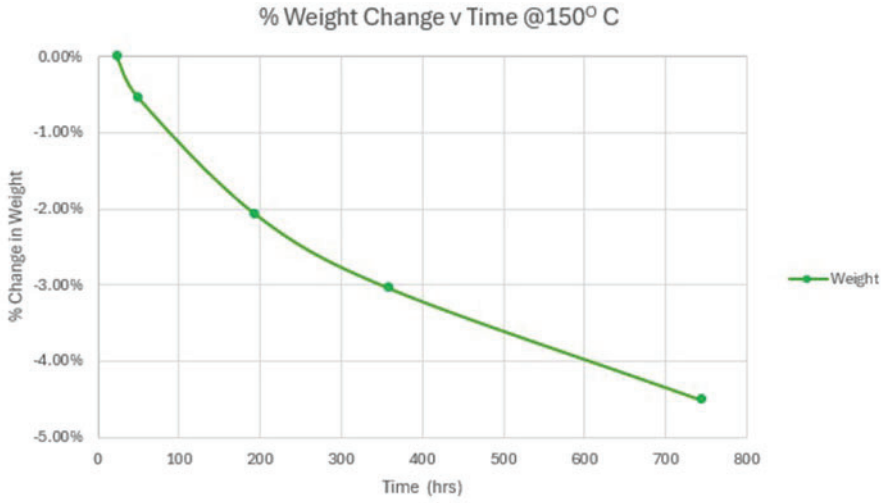

Figure 13. %Change in Weight of Compression Cylinder after 31 days at 150 °C. (Trend line added to assist seeing the data points).

It is unclear at this time if shrinkage during aging will cause enough residual stress to build up in the epoxy layer that is adhesively bound to a grout layer to cause cracking.

2.3.5 Plans for Accelerated Aging and Concerns

In this application the epoxy layer will be constantly submerged in tank waste solution that will have a maximum temperature of 27 ^{O}C, contain various salts along with 4% NaOH (1M or pH=14), and the radiation exposure will be extremely low at 0.175 mCi/L as reported by H2C. In this research we

proposed to do Time Temperature Superposition under two conditions, aging in ovens under air (referred to as TTS conditions) and aging in tank waste simulant (referred to as Time Temperature Chemical Superposition, TTCS). H2C provided SRNL with a tank simulant recipe. In addition, radiation exposure testing would be completed in the Irradiation Lab at SRNL. The radiation testing would be done last since the rad exposure is so low and would be carried out if time and funding was available. It was proposed to do the TTS in ovens at SRNL and the TTCS in tanks at Florida International University (FIU). These tanks were available at FIU from previous testing on composite transfer hoses. [20] [21] Both methods, TTS and TTCS, were proposed to separate out the effects of chemical solution over time versus the effects of time only.

The techniques used in TTS and TTCS are often used in accelerated aging of polymeric materials to determine service life. [22], [23], [24], [25], [26] Samples are placed in aging ovens (TTS) or heated tanks of simulant (TTCS) at several elevated temperatures, removed at various times, and tested for specific criterion properties. The degradation in physical property is plotted versus time at all the temperatures and the curves at higher temperatures are shifted onto the lowest aging temperature curve so the data points overlap one another. This forms one Master Curve and the decrease in physical property dips down below a certain criterion level by the curves from higher temperatures.

One underlying concern with accelerated aging using TTS and TTCS is setting the aging conditions so significant changes are observed within a reasonable time. The lowest temperature curve must show some significant decrease or inflection point in the property tested. If aged samples at the lowest temperature do not show an inflection point, or drop off in property, then the curves at higher temperatures cannot be shifted over.

In TTS It is highly recommended that a phase transition temperature like the glass transition temperature (Tg) or crystal melt temperature (Tm) not fall within the range of temperatures used for aging. The NDA Epoxy formulation used plasticizers to create a plastic deformation plateau region in the stress/strain curves shown back in **Figure 7**. This plastic deformation plateau is suspected to cause the desired effect of minimum shrinkage at the tank wall as well as prevent cracking during cure. The epoxy will be able to deform and accommodate expansion during the exothermic cure reaction without cracking. Unfortunately, the plasticizer also decreases the Tg of the epoxy down to a temperature of 52^{O} C when tested by DSC and 65 ^{O}C by DMA. Since the epoxy layer will be in service below Tg, or in the glassy state, aging should occur below Tg. This limits the maximum aging temperature to around 55^{O} C and there is concern that not enough degradation in properties will occur at aging temperatures at or below 55^{O} C.

It may be possible to come to a conservative, reasonable answer for service life prediction of refurbished tanks by running TTS and TTCS both in the glassy state and the rubbery state. Degradation of polymer will occur more quickly in the rubbery state (above Tg) than in the glassy state (below Tg). By shifting the property versus time curve at temperatures above Tg to the lowest temperature that shows degradation at some reasonable timeframe the time when the Master curve reaches the criterion property level will be faster than if the epoxy were in the glassy state and will represent a conservative estimate of service life. It will be an underestimation of service life. This is not the ideal way to predict service life, but it was used to come up with a conservative estimation of service life in a Hose-In-Hose transfer hose application that worked well for the Tank Farm. [27], [28]

For TTS, proposed aging temperatures below Tg would be 40, 45, 50, and 55 ^{O}C and proposed aging temperatures above Tg would be 70, 90, 110, and 130 ^{O}C. For TTCS, the proposed aging temperature below Tg would be the same 40, 45, 50, and 55 ^{O}C. Aging temperatures above Tg are constrained in TTCS conditions by the boiling point of the simulant that they are soaking in, boiling point (bp) for the simulant will be somewhere between 90 and 100 ^{O}C, so aging temperatures above Tg would be 65, 73, 81, and 90^{O} C. The hope is that the conservative predicted service life will be a long enough time for any refurbished waste tanks at Hanford to store liquid waste until all liquid waste tanks are closed.

2.4 Scaling Up and Heat Transfer Experiments

It was decided in the first half of Year 2 that Scale Up of the two layer approach would be undertaken at the Engineering and Design Laboratory (EDL), 786-A at SRNL or at the new Advanced Manufacturing Collaborative (AMC) facility high bay. It was felt that proving the ability to scale up the two layer approach was needed before any scale up at Hanford in Year 3 or start of accelerated aging occurred. One of the more important variables impacting maximum allowable temperature during cure is the thickness of the epoxy layer, when thickness increases the volume and mass of epoxy increases per unit area of heat transfer surface. Change in mass per unit area is what increases maximum cure temperature.

With that in mind heat transfer experiments were being designed where the maximum temperature will be measured for cast molds of epoxy that would be 20.75” x 12.75” and of varying thicknesses of 2”, 3”, and 4”. In theory, the sample at 2” of thickness will attain a maximum cure temperature of approximately 80 °C, the sample at 4”thickness will attain approximately 160 °C, and the 3” samples will be somewhere in between. This would be consistent with the maximum cure temperature of 80 °C observed for the 48” x 48” x 2” thick cast mold in AVANTech testing mentioned in the Introduction. [7] If cracking is observed in the 3” or 4” thick samples and not on the 2” thick sample then the maximum thickness of the epoxy sealant layer will remain at 2” and if no cracking is observed at the two greater thicknesses than maximum allowable thickness could increase. This would allow for less stringent requirements on self-leveling of the grout layer.

After the heat transfer experiments, scale up at the EDL would occur. This would be done in an 8’ diameter tank. An eight foot diameter by two foot high livestock water trough made of galvanized steel was targeted to be employed. The trough would be placed on 8’diameter x 6” high cribbing to allow for movement out of the way as the first grout layer dries for about 28 days. These are shown in **Figure 14**.

Figure 14. 8 foot diameter tank on the left and 8 foot diameter cribbing on the right.

A portable concrete mixer can be used for mixing grout and the mix fed to a hopper that feeds a pump that would deliver the grout to the tank. The second epoxy layer would then be poured on top of the grout after drying/hydrating for about 28 days. In line mixers would be used to mix part A epoxy resin

and part B curative coming from pumps attached to feed tanks. In line mixing would be far more efficient than batch mixing of part A and part B and subsequent pumping to the tank bottom. Pictures of in line mixers from Koflo Corp. are shown in **Figure 15**. Some preliminary experiments would be needed to determine the length and diameter of the in line mixer needed for pumping epoxy onto the grout layer as quickly as possible. Tg testing would be used to determine good mixing.

Figure 15: Examples of in line mixers. Clear PVC piping with baffles visible inside on the left. Stainless steel piping with high viscosity baffles partially removed and shown on the right for high viscosity liquids like two part epoxies.

Process properties that were intended to be measured during the scale up include the following:

- Self-leveling of the grout layer at various locations from the exit of the conduit(s) delivering grout.
- Maximum temperature during cure of the epoxy using an IR Thermometer directed on the epoxy surface.
- Time for spread of epoxy from initial exit at conduit onto tank floor to when the resin front first reaches the tank wall using video.
- Time from initial tank wall contact to final epoxy thickness again using video.
- Pressure profile that develops at the tank wall as the epoxy layer heats up and cools down during cure using pressure transducers placed on the inside of the tank wall.
- Observation of any cracking in the grout and epoxy layer.
- Observation and measurement of any gap that would develop between the tank wall and new tank bottom (grout and epoxy layers).

Since destruction of the two layer tank bottom would be required to test material properties, samples would be taken after full cure of the second epoxy layer. Material properties that were intended to be measured after all processing experiments and cure of the epoxy layer had occurred include the following:

- Grout compression strength using ASTM C39.
- Grout porosity ASTM C642.

- Adhesion of epoxy to grout using ASTM D7234.
- Epoxy compression strength using ASTM D695.
- Epoxy Tg using ASTM E1640.

In addition, as the result of an encouraging and successful meeting with AGI Engineering in November of 2025 it was decided that we would attempt to redirect some funding (about $50K) from FIU to a scale up at AGI Engineering. AGI Engineering is familiar with the Hanford Site; they were the contractor that cleaned tank AY-102 by using hydraulic controlled robotic arms to direct sluicing water jets on difficult to remove saltcake at the bottom of the tank, see **Figure 16.** AGI had this equipment readily available at their facility and it was thought that these could be modified to deliver both the grout layer and subsequently the epoxy layer to the bottom of the tank. It was intended to create synergistic collaboration between AGI and SRNL on this scale up portion of the research. In addition, if a gap did develop at the tank wall using conventional techniques of delivering grout and epoxy, it is believed that these robotic arms could precisely deliver epoxy in the gap, see **Figure 16**. If epoxy could be delivered precisely at a tank wall gap located at the tank knuckle so there was curvature as shown in the figure, hydrostatic pressure from the tank waste could assist in providing sealing pressure at the tank wall knuckle/epoxy layer interface.

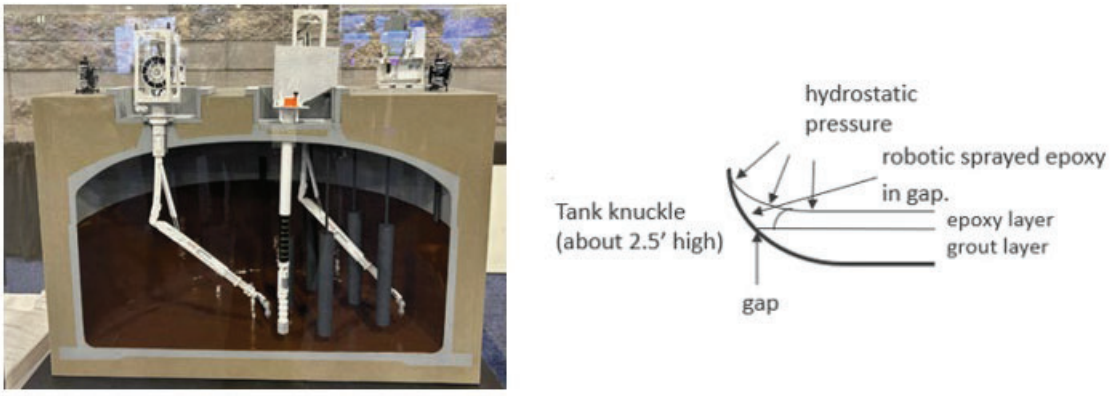

Figure 16. On the left is a photo of a not to scale mockup of AGI robotic sluicing arms in a Hanford waste tank. On the right is the result of filling any gap that would develop at the tank wall using the AGI robotic arm.

Unfortunately, a good bit of thought and planning had occurred for the activities discussed in this section but none of it was brought to fruition due to the curtailment of funding. It had been intended to start intense planning for delivery of mixed grout and mixed epoxy to the 8' tank bottom in January 2026. Charge codes for this portion (Tank Bottom Refurbishment) of Award #277993 were turned off in January of 2026 due to withholding of second half funds by the Hanford DOE Field Office in October of 2025. Funding for the program stopped before this work could be completed.

3.0 Areas of Concern and Technology Gaps Identified

To the authors' knowledge no attempt had ever been made to create a monolithic sealant layer of epoxy on a grout/cement surface that was 75 feet in diameter in an area not available to human access due to radiation. Technological concerns and gaps along with potential ways to answer these gaps were

identified during the course of this research that was truncated by a lack of funding after 1.5 years (expected duration was 3 years). They include the following:

- **Cracking**
  What is the maximum thickness of an epoxy layer that can be poured before enough heat is generated that causes cracking due to adhesion and mismatch in coefficient of linear expansion between grout and epoxy assuming that the epoxy layer will have a constant thickness? All this occurs during the cure process where temperature reaches a maximum and then decreases due to slow down in cure reactions and heat transfer. AVANTech reported [7] that an NDA epoxy cast mold of 48" x 48" x 2" did not crack like the other candidate epoxy. A maximum cure temperature of 80 ^{O}C was reached in 3 to 4 hours and total cure time (epoxy was no longer tacky when touched) was 14 days with no cracking observed. In this research the hypothesis was made that this maximum temperature is controlled primarily by the final thickness of the epoxy layer poured regardless of the areal size of the layer. Heat transfer experiments were being planned to prove this concept but never came to fruition. The stress strain curves of the NDA epoxy at various stages of room temperature cure indicate that there may be enough viscoelastic behavior of the epoxy during cure so that cracking will not occur.

- **Minimum and Maximum Thickness of Layers**
  Can a grout layer be poured over a 75' tank bottom surface such that the variation in levelness is minimal and cracking would not occur? For example, if 2" is determined to be the maximum allowable thickness of poured epoxy before cracking occurs, can a grout layer be poured with enough self-leveling (no human or robotic screeding) such that the variation in the epoxy layer thickness is between 0.125" and 2". A somewhat arbitrary assumption is made that 0.125" (1/8") is an adequate thickness for sealing. In general, the maximum thickness of a "coating" is about 1/8". Variables that would affect variation in thickness of the grout layer would include the following: number of conduits delivering grout to the tank bottom; diameter of the conduits; volumetric pumping rates; formulating of grout that affects slump and viscosity; etc. Scale up testing in an 8' diameter tank would begin to give more practical answers to these questions.

- **Occurrence of a Gap at the Tank Wall**
  Will a gap be created at the interface between the tank wall and epoxy sealant layer if a 2" layer is poured onto a 75' diameter surface? AVANTech reported that in an NDA epoxy cast mold of 48" x 48" x 2" no gap was observed at the mold wall and epoxy, as was observed on the other candidate epoxy in the same test. If the occurrence of a gap becomes an issue if and when this research was to continue it may be helpful to run rheometer viscoelastic experiments where complex viscosity $\eta*$, storage modulus G', loss modulus G", and Temperature are plotted versus time of cure. The point where the G' curve intersects the G" curve and G' values become greater than G" values is called the gelation point. This is the point when the epoxy transitions from a somewhat flowable liquid to a solid. [29] If tank wall gaps and cracking end up being persistent issues this is likely the general path to take forward. The maximum cure temperature should occur before the gelation point so the epoxy can still deform or "flow" as the epoxy recedes in size while it cools.

- **Determination of Service Life of the Two Layer Grout and Epoxy Approach**
  Use of DSTs was initially expected to be about 40 years and they have been in service for 38 to 56 years. [30] During the proposal stage of this project operational plans indicated that WTP operations are expected to be completed in 2075 so one target for service life extension of a refurbished DST would be 40 years. In the two layer approach the critical service life would be that of the epoxy layer since it is in contact with waste process streams and must provide a seal to prevent leakage. The primary requirements of the grout layer were to provide a fresh surface for adhesion, have enough cohesive strength to form a good bond with the epoxy layer and steel tank bottom, and be self-leveling enough so the epoxy layer gets complete coverage without cracking. As discussed in Section 2.3.5 on Accelerated Aging, it could potentially take a long period of time to get results from accelerated aging of the epoxy layer, therefore, it was decided to put greater emphasis on scaling up and ensuring that indeed the NDA epoxy was the material of choice that fulfilled all processing and physical properties required for the task before placing it in accelerated aging conditions. It was expected that by bringing AGI Engineering on board that there would be synergy created to determine all these processing and physical property requirements in a more efficient manner. The methods to be used for accelerated aging are outlined in Section 2.3.5. It would be possible to determine a reasonably conservative service life prediction using the same methods and assumptions as were used for determining service life for the transfer hoses met in section 2.3.5.

- **Concern with Organics Leaching into the Liquid Waste**
  The Hanford facility has concerns with the type and amounts of organics present in the Tank Farm liquid waste. This is due to concern over flammable gas buildup from volatile organics, flammable gaseous hydrogen from hydrocarbon compound radiolysis and degradation, worker exposure to hazardous fumes, and regulatory requirements. [31] The reactive plasticizer used in the NDA epoxy formulation would appear to have greater potential to generate hazardous and flammable vapors than the other ingredients since it has an aliphatic tail that is about twelve carbons long. One possible route to determine noxious chemicals formed would be to use a calculation using G-values for the organic plasticizer, diglycidyl ether of bisphenol A (DGEBA, the epoxide portion of the formulation), and curatives used in the formulation. If G values do not exist for all ingredients, then a G value for a similar compound could be substituted. G-values can be used to quantify the moles of reaction product per 100 eV of radiation. Assuming that stoichiometric amounts of the ingredients would leach into the tank waste, weight changes observed during accelerated aging could be part of the basis of these calculations as a first estimate. However, since the level of radiation is expected to be quite low (0.175 mCi/L) the caustic environment might generate more noxious chemicals than radiolysis. Another exercise could be to use the weight loss during accelerated aging and determine the amount of theoretical H_2 generated if all H in the polymer thermoset network had converted to hydrogen gas. This could represent a theoretical maximum of noxious chemicals generated to determine if it is above or below any flammability and hazard limits. Reference [31] cited in this paragraph may also provide further insight on how to approach this issue.

4.0 Accomplishments/Conclusions

- All the cementitious grouts exhibited favorable properties for the tank refurbishment application. **Table 11** refers back to the criteria listed in **Table 10** and the outcome of the bench scale testing done in this work, these two Tables are shown in Appendix B. The mix flows were >24 in. by ASTM C1611, indicating fluid or highly flowable and pumpable grouts. The mixes exhibited no bleed or segregation. The commercial grouts are most promising due to their higher flows compared to the reactor closure grouts, which is critical for being able to cover Hanford waste tanks up to 75 ft diameter, and they also demonstrate higher strength. Placement should occur as fast as reasonably possible to prevent loss of flow with any delays in pouring.
- Overall, the satisfactory properties of the grouts for the tank refurbishment application justify testing at larger, engineering scale.
- Engineered scale testing of grout is warranted based on current results, to check for the following:
    - Flowability and pumpability at 8-10 ft diameter scale. Degree of self-leveling.
    - Considering effects of static or long mixing times.
    - Cured properties such as shrinkage. It will be particularly important to check if the grout stays adhered to the tank sidewalls or if there are cracks in the center after curing.
- Chemical durability testing should be done with grout materials coated with epoxy to confirm the epoxy coating prevents changes in the grout (weight increase and/or surface color/leaching) due to tank waste simulant exposure. Another consideration is to do chemical durability testing with only the top surface of grout and/or epoxy exposed akin to the setup of the tank.
- Desirable properties for the epoxy sealant layer have been identified and are listed in **Table 9** shown in Appendix A. The NDA epoxy appears to satisfy all these requirements; this is demonstrated in section 2.2 Evaluation of NDA Epoxy and discussed further in section 2.3 Expectations for Physical Properties.
- Overall, the satisfactory properties of the NDA Epoxy for the tank refurbishment application justify testing at larger, engineering scale.
- Engineered scale testing of the NDA epoxy is warranted based on current results, to check for the following:
    - The speed at which the epoxy layer covers the grout layer and comes to final thickness.
    - If maximum cure temperature is maintained around 80 ^{O}C when a layer of epoxy is poured that maintains a maximum thickness of 2”.
    - No cracking is observed.
    - Measurement of pressure at the tank wall from the expanding epoxy during elevated cure temperatures generated.

  - Homogeneous blending of part A epoxy resin and part B curative occurs using in line mixers.
  - Cured properties identified in section 2.2.
  - Does a gap develop at the tank wall / epoxy interface.

- AGI Engineering has been identified as a potential partner for scale up both on a small scale at SRNL and large scale at Hanford. Contact information for AGI is listed in Appendix C.
- Areas of Concern and Technology Gaps are identified in section 3.0.

5.0 References

[1] Network of National Laboratories for Environmental Management and Stewardship(NNLEMS), "R&D Roadmap for Hanford TAnk Waste Mission Acceleration," Report NNLEMS-2022-00005, 2022.

[2] WRPS Chief of Technology Office, "Tank Repair Feasibility", RPP-RPT-62020 WRPS Technical Report," 2020.

[3] T. Wooley, K. Boomer, A. Pappas, “An Ode to Tank Repair and a Longevity Strategy for Underground Storage Tanks at the Hanford”, in *Proceedings of Waste Management 2022 Conference*, Phoenix, 2022.

[4] R. Calmus, “Tank Repair Technology Development – Strategy, Status, and Path Forward”, in *Presentation at Waste Management Conference 2022*, Phoenix, 2022.

[5] N. Valdes, "“Refurbishing Hanford Waste Tanks – Overview on Grout Layers”, SRNL-TR-2025-00056 Technical Report," 2025.

[6] K. Blue, M. Alderman, N. Valdes, M. Kranjc, "“Initial Progress on Tank Bottom Repair for the DOE EM Tank Waste R&D Program 25089”," in *Proceedings of Waste Management 2025 Conference*, Phoenix, 2025.

[7] N. Campbell, "Epoxy Sealant Self-leveling and Adhesion Test Report”, AVANTech Technical Report TR-23302-00, rev. 1, March, 2024.

[8] R. Clough, K. Gillend, D. Cleg, A. Collyer, "Irradiation Effects on Polymers", pp110-111, Elsevier Applied Science, New York, 1991.

[9] M. Alderman, K. Blue, N. Valdes, M. Kranjc, “Tank Bottom Refurbishment Year 1 Report”, SRNL-TR-2025-00233 rev 0 Technical Report, 2025.

[10] S. Doll, ""Bottom Sealant Assumptions for SRNL", email correspondence March 13, 2025".

[11] C. Langton, N. Valdes, "Flowable Cementitious Grouts for False Bottoms in Hanford Waste Tanks," in *Proceedings of Waste Management 2026 Conference*, Phoenix, 2026.

[12] C. Langton, J. Wu, M. Hendrickson, "Testing Case for Closure of Hanford's 241-C Underground Storage Tanks," 2023.

[13] C. Langton, et al, "Use of Cementitious Materials for SRS Reactor Facility In-Situ Decommissioning," in *Proceedings of Waste Management 2011 Conference*, Phoenix, 2011.

[14] C. Langton, et al "Cementitious Grout for Closing SRS High Level Waste Tanks," in *Proceedings of Waste Management 2012 Conference*, Phoenix, 2012.

[15] J. Bear, *Dynamics of Fluids in Porous Media*, Cambridge University Press, 1972.

[16] C. Langton, T. Lorier, "Review of Cementitious Materials Development and Applications That Have Supported DOE-EM Missions: WasteTreatment, Conditioning, Containment Structures, Tank Closures, Facility Decommissioning, Environmental Restoration, and Structural Assessments," SRNL-STI-2019-00009 Technical Report, 2019.

[17] S. Doll, "Bottom Sealant: Supernate Simulants", email correspondence, August 22, 2024.

[18] Google AI, 29 June 2026. [Online]. Available: https://www.google.com/search?q=Typical+Pull+Up+Adhesive+strength+of+concrete+to+epoxy&sca_esv=5a54545fb4e7d790&source=hp&ei=mmpCapGANN7gp84PssuQ2Ao&iflsig=ABILxe8AAAAAakJ4qj0afidrhcTYYPhcJ6wgdbZ7FiWU&ved=0ahUKEwiRtaX5vqyVAxVe8MkDHbIlBKsQ4dUDCCA&uact=5&oq.
Accessed 29 June 2026.

[19] Google AI, 29 June 2026. [Online]. Available: https://www.google.com/search?q=Typical+tensile+strengths+of+epoxy&sca_esv=5a54545fb4e7d790&ei=wmpCatCQBena0PEP3JjZ2AM&biw=1528&bih=698&ved=0ahUKEwjQ-f-Lv6yVAxVpLTQIHVxMFjsQ4dUDCBI&uact=5&oq=Typical+tensile+strengths+of+epoxy&gs_lp=Egxnd3Mtd2l6LXNlcnAiIlR.
Accessed 29 June 2026.

[20] A. Awwad, D. McDaniel, J.Rivera, "Accelerated Aging and Evaluation of Hose-In-Hose Transfer Lines in the Hanford WasteTransfer System," in *Proceedings of Waste Management 2020 Conference*, Phoenix, 2020.

[21] D. McDaniel, J. Rivera, L. Legos, A. Awwad, "Effects of Sodium Hydroxide, Temperature, and Exposure Duration on Hose-In-Hose Transfer Lines Used in the Hanford Waste Transfer Systems" *in Proceedings of Waste Management 2022 Conference*, Phoenix, 2022.

[22] J. Ferry, *Viscoelastic Properties of Polymers, 3rd edition*, John Wiley and Sons Inc., pp 264-320, New York, 1980.

[23] J. Aklonis, W. Macknight, *Introduction to Polymer Viscoelasticity, 2nd edition*, John Wiley and Sons Inc., pp 36-56, New York, 1983.

[24] M. Silva, B. Fonseca, H. Biscala, "On Estimates of Durability of FRP Based on Accelerated Tests," *Composite Structures,* vol. 377, p. 116, 2014.

[25] D. Gibhardt, A. Krauklis, A. Doblies, A. Gagani, S. Sabalina, O. Starkova, B. Fiedler, "Time, Temeprature, and Water Aging Failure Envelopeof Thermoset Polymers," *Polymer Testing,* vol. 18, p. 1, 2023.

[26] A. Guen-Geffroy, P. LeGac, B. Habert, P. Davies, "Physical Aging of Epoxy in a Wet Environment: Coupling Between Plasticization and Physical Aging," *Polymer Degradation and Stability,* vol. 108947, p. 168, 2019.

[27] M. Kranjc, T. Skidmore, R. Hawsey, "Service Life Evaluation of the Hose-In-Hose Transfer System Between Tank 13 and 15", SRNL-TR-2021-00828 Technical Report," 2021.

[28] M. Kranjc, B. Hill, "Update on Accelerated Aging Tests and Preparation Work for Forensics Testing After Service Life of Tank 13/15 HIH", SRNL-TR-2022-00519 Technical Report," 2022.

[29] T. Chen, B. Rajaram, "Characterizing Thermoset Curing Using Rheology," in *SAMPE 2019 Conference Proceedings*, Charlotte, 2019.

[30] P. Shukla, "Integrity Monitoring and Assessment, Prediction, Repair, and Corrosion Control of the Hanford Storage Tanks, Proposal Submittal to LAB23-EM001 Announcement," 2024.

[31] M. Lindberg, L. Stock, G. Cooke, H. Meznarich, S. Doll, "Process Knowledge Concerning Organic Chemicals in Hanford Tank Waste Supernate", RPP-RPT-61301 Technical Report, 2019.

[32] N. Valdes, "Task Technical Plan for Hanford Tank Bottom Refurbishment Using Grouts", SRNL-RP-2025-00379 Technical Report, 2025.

APPENDIX A - Requirements for the Epoxy Sealant Layer

Table 9. Desirable Properties of the Epoxy Layer

Priority Level	Property	Criterion	Method to Determine	Reasoning/Comments
1	Glass Transition Temperature (T_g)	> or = about 50^{O} C approximately 20^{O} C above max service temperature (27^{O} C)	ASTM D1356 Determining Tg and Tm by DSC ASTM E1640 Assignment of Tg by DMA	- Less degradation occurrs in the glassy state - DMA method proved to be a more reliable method
1	Compression Stress at Yield	- Hydrostatic pressure on the bottom of the tank is about 0.10 MPa (15 psi) - Criterion is set at 4x hydrostatic pressure or 0.40 MPa (60 psi)	ASTM D695 Compressive Properties of Rigid Plastics	- Very likley to be easily achieved after cure. - Also expected to be achievable after accelerated aging
1	Toughness	TBD	ASTM D695 Compressive Properties of Rigid Plastics	- Greater toughness will help prevent cracking - Area under Compression Stress/Strain Curve
1	Adhesion Between Grout and Epoxy Layers	TBD (currently set at 5.52 MPa (800 psi)	ASTM D7234 Pull-Off Strength of Coatings on Concrete	- Adhesion test to use was an FIU task. Several tests were considered and evaluation presented; final decision made by SRNL. - Determined to be the best adhesion test due to a combination of ease of use, ability to prepare and test many samples with significantly less sample and test machine preparation time, and comparison to data that has already been generated by WRPS on some epoxy systems.
1	Workability Life (or Pot Life)	Final criterion was to be determined after scale up in Year 3. Currently set at 2 hours before reaching 2,000 mPa-sec on rheometer	Rheometer DSC Large scale testing in year 2 and 3 to compliment rheometer and DSC data.	- Depends on the following: - Resin viscosity, which will depend on rate/degree of cure, temperature, etc. - Tihcknes and volume of the epoxy layer needed. - Pump capacity. - Diameter & number of conduits to tank floor. - Will resin fronts from different conduits bond sufficiently
1	Low Maximum Cure Temperature	TBD	Rheometer DSC Large scale testing Maybe ThermTest	- To prevent cracking of epoxy layer as it cures (expansion during rxn then contraction during cooling) - What is CTE at various degrees of cure and temperature. ThermTest measures CTE on solid samples only.
1	Required Thickness of Epoxy Layer	TBD. Currently should vary between 3/8" to 2". What is reasonable for a self leveling grout.	Large scale testing in Year 2 and 3	- What is a reasonable range of epoxy layer thickness considering that the self leveling grout layer will not be perfectly self leveling - Currently the minimum thickness needed for sealing is set at 3/8" - The maximum thickness depends on how self-leveled the grout can be which influences how much heat is generated during epoxy cure (the greater the epoxy thickness the greater the volume, heat of reaction, and potential cracking)
1	Cure Shrinkage	0% or a maximum that is low enough to accommodate a 75' diameter monolith	Large scale testing in Year 3	- 0% needed so there is no gap between monolith and tank wall - Robots can apply an epoxy sealant at gap between wall and monolith if a gap develops (AGI). - Spraying the entire epoxy layer instead of pouring was considered but there was concern about time it would take to do this and quality of the coverage which would likely be less than 3/8". Seems like using robots to spray coat an epoxy sealant layer at the gap would be simpler and faster

Table 9 (Cont'd). Desirable Properties of the Epoxy Layer

Priority Level	Property	Criterion	Method to Determine	Reasoning/Comments
2	Low Moisture Absorption	4% maximum, below Tg	TTCS, weighment	- Literature shows that moisture absorption of several epoxies in pure water and seawater is about 4% - Some moisture absorption could be beneficial in that it could cause expansion and better sealing at the tank wall. For best sealing may want to introduce a small layer of water for expansion prior to introduction of waste for sealing at the tank wall. - NDA epoxy has a large platuea in the stress/strain curve beyond the yield point in compression, therefore, it appears that epoxy might be able to withstand a good deal of compression before cracking.
2	Coefficient of Thermal Expansion (CTE)	- CTE range between 16 to 27^{O} C service temperaturer range should be as low as possible to maintain sealing at the tank wall.	ThermTest	- Does this depend on thickness variation? - Some elasticity without creep could maintain sealing pressure and adhesion
3	Degree of Cure	TBD	DSC FTIR	- If degree of cure is not 100% then applied energy due to aging at room temp and rad from tank waste would be expended in crosslinking reactions rather than in degradation reactions. Suspicion is that completing crosslinking would occur before degradation due to lower activation energy (Ea) of crosslinking than degradation rxns. - DSC indicates that degree of reaction is not 100% after room temperature cure.

APPENDIX B - Requirements for the Initial Grout Layer

Table 10. Criteria of Using Grout for Tank Refurbishment

Criteria	Reasons
Pumpable	• Limited tank access. • Transport material from external environment (tank farm area) to the access point of the tank. • 4 in openings on tank tops.
Fluid/Flowable	• Once the grout enters the tank, it must be able to flow as far as possible (up to the walls) and also around and over any obstacles such as residual saltcake.
No bleed or segregation	• Structural integrity and homogeneity. • Surface must be as dry as possible for epoxy application and bonding.
Low shrinkage	• Minimize shrinkage to eliminate cracking and promote bonding to metal. • Grout must maintain contact with the walls to prevent liquid from seeping to the bottom or under the grout.
Chemical Durability	• Withstand tank waste, especially if there is incomplete coverage of epoxy, or if the epoxy sealant ends up not being used. No cracks should be observed which would provide a pathway for tank waste to reach the steel.
Adhesion to carbon steel	• Form strong bond with steel tank to prevent peeling or leaking, especially on the side walls.

Table 11. Outcome of Grout Testing to Date

Criteria	Criteria Met?
Pumpable	Yes. Grouts A and B are fluid, but all are acceptable. Mixing and pouring should be done as quickly as possible.
Flowable	Yes. Grouts A and B are fluid, but all are acceptable. Mixing and pouring should be done as quickly as possible.
No bleed or segregation	Yes, observed visually.
Low shrinkage	Yes, but must be monitored during engineered scale experiments.
Durability in tank waste simulant	Yes, due to no structural cracking. However, leaching and material ingress observed. Grout/epoxy durability testing needed to confirm if epoxy can prevent these effects.
Adhesion to carbon steel	Yes, qualitatively observed on steel plate samples.

APPENDIX C - AGI Contact Information

- AGI Engineering

  14175 State Rte. 26, Linden, CA 95236
- Founder and CEO: Alex Innes
- Year Founded: 1996
- Office Administrator: Kristen Godfrey
- Email contacts: alex@agieng.com

  kristen@agieng.com

  info@agieng.com
- Company website: http://www.agieng.com/
- Phone: 209-939-9900

Distribution:

Maxwell Alderman
Camden Chatham
Benjamin Barkai
Kareen Blue
Charles W. James
Haley Jones
Will Jolin
Mark Kranjc
Christine Langton
Joseph Manna
Anastasia Mullins
Thomas Eric Skidmore
Pavan Shukla
Kiana Sykes
Nicholas Valdes
Morgan Whiteside
Cade Willis

FIU-ARC-2026-800019286-04b-001

Adhesion and Durability Evaluation of Epoxy Coatings on Grout for DOE Nuclear Waste Tank Refurbishment

Final Technical Report – Florida International University

Dwayne McDaniel, PhD., P.E.
Applied Research Center, Florida International University, FL

August 2026

Project support: U.S. Department of Energy, TOA No. 0000687324

Executive Summary

The U.S. Department of Energy is evaluating refurbishment strategies for aging nuclear waste storage tanks. One candidate approach uses a cementitious grout layer to restore geometry, distribute loads, and provide structural support, followed by a polymeric epoxy coating that serves as a chemical and moisture barrier. The reliability of this layered system depends on the epoxy–grout interface, particularly when surface preparation is limited and the system is exposed to high-pH chemistry and elevated temperature.

Florida International University's portion of this collaborative project focused on the initial adhesion and long-term durability of epoxy coatings applied to grout. Three proprietary grout formulations—Grout A, Grout X, and Grout BC—were evaluated with one commercial two-component epoxy system. The grout surfaces were retained in the as-cast condition and only air-cleaned before coating to represent field conditions where grinding or chemical treatment may be impractical.

Surface characterization included three-dimensional profilometry, static water contact-angle measurements, and scanning electron microscopy. The epoxy was applied at approximately 2 mm thickness, cured for 14 days under ambient conditions, and evaluated using pull-off adhesion testing and failure-mode analysis. Clear differences were observed among the three grouts. Grout A exhibited low roughness, favorable and consistent wettability, a dense near-surface morphology, and an average adhesion strength of 5.38 MPa. Grout X had the highest roughness but also contained larger surface-connected cavities, showed a higher and more variable contact angle, and produced a lower and more variable adhesion strength of 3.98 MPa. Grout BC exhibited moderate roughness and wettability, favorable substrate integrity, and the highest average pull-off strength of approximately 6.37 MPa. Failure modes also differed. Grout A primarily showed adhesive failure at the epoxy–grout interface, Grout X predominantly showed substrate failure, and Grout BC exhibited mixed adhesive and cohesive failure. These findings showed that roughness alone was not sufficient to predict adhesion. Surface continuity, wettability, near-surface morphology, and substrate integrity collectively governed bond strength and failure behavior. Based on its higher adhesion strength and balanced failure response, Grout BC was selected for durability evaluation.

Two alkaline-aging configurations were developed to determine which method would provide the most reliable and repeatable exposure. The first used EPDM and PTFE wrapping around the specimen to expose the intended coating region while sealing the remaining surfaces. The second used a PTFE cylinder compressed and sealed on top of the coated grout, confining a high-pH multicomponent waste simulant to a defined area of the epoxy surface. The methods were compared in terms of leakage resistance, exposure control, repeatability, handling, and long-duration suitability. An automated temperature-control and monitoring system was developed for the PTFE-cylinder setup. It incorporated an external silicone heating pad, wall and solution temperature sensors, a microcontroller, and data logging.

1. Project Background and FIU Scope

1.1 Tank refurbishment context

The Hanford double-shell tanks are critical infrastructure for storing high-level radioactive waste. The project background identifies aging of the primary carbon-steel bottom plate under highly alkaline chemistry, thermal loading, mechanical settling stresses, and localized corrosion or pitting as a containment concern. A practical refurbishment strategy must restore support and geometry while reducing direct contact between the waste environment and the underlying structure.

The candidate layered concept evaluated by the project places cementitious grout over the existing tank bottom and applies a polymeric epoxy coating over the grout (Figure 1). The grout provides leveling, load distribution, structural support, and immobilization functions. The epoxy provides chemical isolation, moisture resistance, and a protective barrier. The epoxy-grout interface is therefore a critical region: loss of bond can produce localized delamination and create pathways for fluid transport.

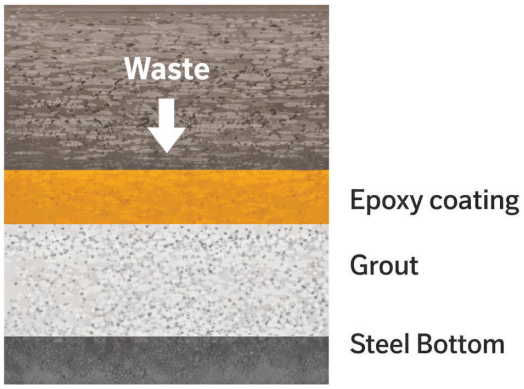

Figure 1: Conceptual layered tank-bottom refurbishment system, with grout epoxy layers

1.2 Collaborative project and FIU responsibility

The broader effort involved collaborators from Florida International University (FIU) and Savannah River National Laboratory (SRNL). Within this program, FIU's technical responsibility was to investigate the adhesion and durability of the epoxy coating on grout. Other project participants developed and optimized proprietary grout formulations and addressed broader tank-refurbishment needs; FIU concentrated on the coating-substrate interface.

- Characterize the as-cast grout surface condition before coating.
- Measure baseline epoxy-grout adhesion strength and classify failure modes.
- Determine how differences among grout formulations affect bond reliability.
- Develop accelerated alkaline-aging methods that expose the epoxy surface while protecting the remainder of the specimen.

1.3 Technical Challenge

Adhesion to cementitious substrates is governed by interacting physical and chemical factors. Mechanical interlocking depends on resin penetration into surface asperities and connected pores. Wetting controls whether the liquid coating can spread and make direct contact. Near-surface porosity, weak layers, loose particles, and

discontinuities can reduce effective contact area or cause failure within the substrate. For these reasons, a rougher surface is not automatically a stronger bonding surface.

The nuclear-service context adds a durability requirement. Even a strong initial bond can degrade when the coating experiences prolonged contact with high-pH solution, temperature gradients, moisture and ion ingress, swelling, and changes in polymer or substrate properties. The FIU program therefore used a staged approach: first establish baseline bond behavior, then develop controlled aging methods and periodic characterization.

2. Objectives and Project Framework

2.1 Objectives

1. Quantify baseline epoxy–grout adhesion performance across different grout formulations under minimal surface preparation conditions.
2. Evaluate epoxy–grout adhesion durability and aging-induced changes in epoxy properties under high-pH chemical exposure and controlled-temperature aging.

2.2 Two-Phase Framework

Phase	Primary Activities	Intended outcome
Phase 1 - Initial Adhesion Performance	Evaluate the surface properties of three different grout formulations and their respective epoxy adhesion strengths	Identify formulation-dependent controls on baseline adhesion.
Phase 2 - Durability and aging	Develop aging configurations, conduct long-term aging under controlled-temperature conditions, and periodically evaluate epoxy–grout adhesion and material properties.	Determine time-dependent degradation of the epoxy coating and epoxy–grout interface.

3. Materials and Specimen Preparation

3.1 Grout Formulations

Three proprietary cementitious grout formulations—Grout A, Grout X, and Grout BC—were provided by SRNL and evaluated in the FIU study (Figure 2). Detailed compositions, mix proportions, and formulation-specific material properties were not disclosed because of proprietary restrictions. These three types of specimens used for surface characterization and coating experiments had nominal dimensions of approximately 2.5 × 2.5 × 1 in. The three grout formulations were evaluated in the as-cast condition without mechanical grinding, abrasive blasting, or chemical surface treatment. Before epoxy application, the grout surfaces were air-cleaned to remove loose debris and surface dust.

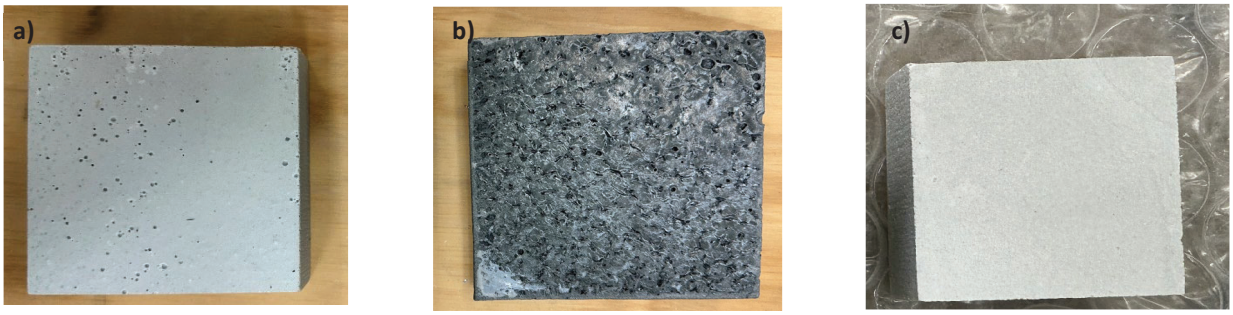

Figure 2: Representative as-cast grout specimens before surface characterization and epoxy application: (a) Grout A, (b) Grout X, and (c) Grout BC

3.2 Epoxy System

A commercial proprietary two-component polymeric epoxy system was provided by SRNL as coating material (Figure 3). The epoxy was self-leveling and was applied directly to the grout without a primer. The resin and hardener were combined at a supplier-specified ratio of 4:1. After mixing, the epoxy was applied to the air-cleaned grout within a silicone-tape mold used to control the coating area and thickness.

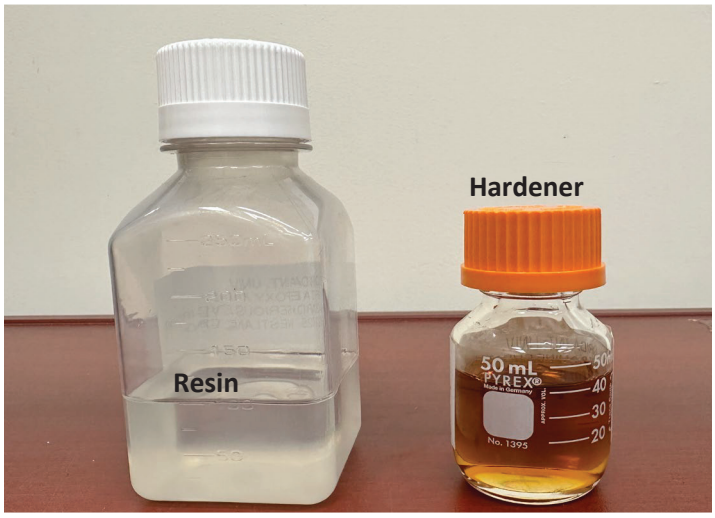

Figure 3: Components of the proprietary two-component epoxy system used in this study

4. Experimental Methods

The experimental program was conducted in two stages. The first stage evaluated the surface properties and baseline epoxy adhesion performance of Grout A, Grout X, and Grout BC under minimal surface preparation. The second stage focused on developing and comparing two alkaline-aging configurations to identify a reliable and repeatable method for long-term evaluation of epoxy–grout adhesion durability and epoxy-property changes.

4.1 Grout Surface Profilometry

The surface topography of the three as-cast grout formulations was characterized before epoxy application using a Nanovea ST400 Modular 3D Surface Profiler. Surface-height data were collected over a 3 × 3 mm scan area at representative locations on each grout. The acquired profiles were plane-leveled before analysis to remove specimen tilt and overall surface form.

4.2 Water Contact-Angle Measurement

The wettability of the grout surfaces was measured using a Surface Analyst™ 3001 system. Measurements were performed on the uncoated, as-cast grout surfaces before epoxy application. A water droplet of known volume was placed on the grout surface, and its footprint was measured using the instrument's top-view imaging system. The apparent contact angle was then calculated from the droplet volume and footprint size. At least five measurements were taken at different locations on each grout specimen to account for surface variation. A lower contact angle indicated better wetting, while a higher contact angle indicated less favorable wetting.

4.3 Scanning Electron Microscopy

Scanning electron microscopy was used to examine the near-surface structure of Grout A, Grout X, and Grout BC. SEM images were collected from the uncoated grout surfaces. The images were used to compare surface texture, continuity of the grout matrix, surface-connected cavities, and other microstructural differences among the grout formulations. These features were considered because they may affect epoxy wetting, penetration, mechanical interlocking, and adhesion.

4.4 Epoxy Coating Application

After surface characterization, the grout specimens were air-cleaned to remove loose particles and dust. No grinding, abrasive blasting, chemical treatment, or primer was used. The resin and hardener were mixed at a 4:1 ratio. A silicone-tape mold was placed around each grout specimen to control the coating area and thickness. The mixed epoxy was poured directly onto the grout and allowed to spread within the mold. The coating thickness was approximately 2 mm. The coated specimens were cured for 14 days at approximately 22 °C and 59% relative humidity before adhesion testing.

4.5 Pull-Off Adhesion and Failure-Mode Evaluation

Epoxy–grout adhesion strength was measured using the ASTM D7234 pull-off test method. Circular steel dollies with a diameter of 20 mm were bonded to the cured epoxy surface (Figure 4). After the adhesive had cured, a core cut was made around each dolly to isolate the test area. Testing was performed using a PosiTest® AT-A pull-off adhesion tester. Tensile loading was applied perpendicular to the coated surface at approximately 0.69 MPa/s, or 100 psi/s, until failure occurred. The pull-off strength was calculated as:

$$\sigma_{\text{pull-off}} = \frac{F_{\max}}{A}$$

where $F_{\max}$is the maximum load at failure and A is the bonded area of the dolly.

Figure 4: Pull-off adhesion test showing the test principle (left) and the portable pull-off adhesion tester used in this study (right)

Multiple tests were performed for each grout formulation. After testing, the failure surfaces were visually examined and classified as adhesive failure at the epoxy–grout interface, cohesive failure within the epoxy, substrate failure within the grout, or mixed failure.

5. Baseline Results and Discussion

5.1 Surface Roughness and Topography

The three grout formulations showed clear differences in surface roughness and topography. The roughness was compared using S_a, the average height variation of the surface, and S_q, the root-mean-square height variation.

Because S_q gives more weight to larger peaks and valleys, it is usually higher than S_a. Grout X had the highest average roughness, with $S_a$and $S_q$values of 12.1 µm and 16.4 µm, respectively. Grout A had the lowest roughness, with an $S_a$of 5.8 µm and an $S_q$of 7.6 µm. Grout BC showed intermediate roughness, with an $S_a$of 8.1 µm and an $S_q$of 11.4 µm (Figure 5).

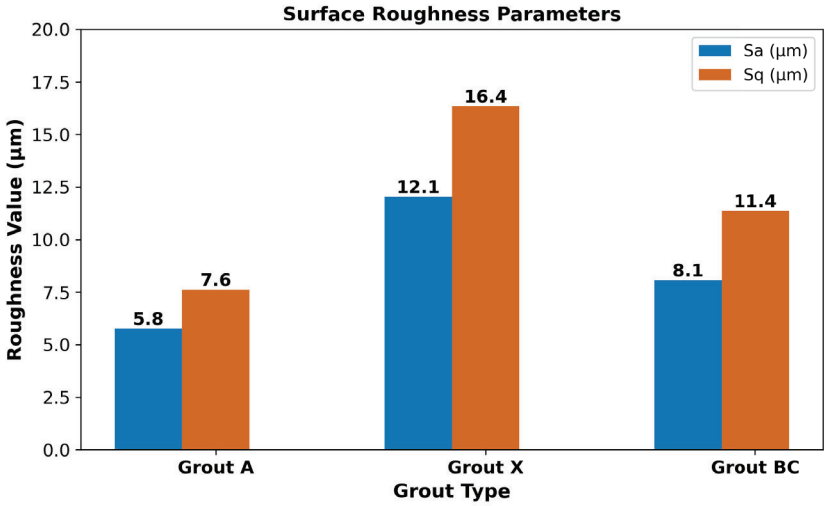

Figure 5: Comparison of the surface roughness parameters for Grout A, Grout X, and Grout BC

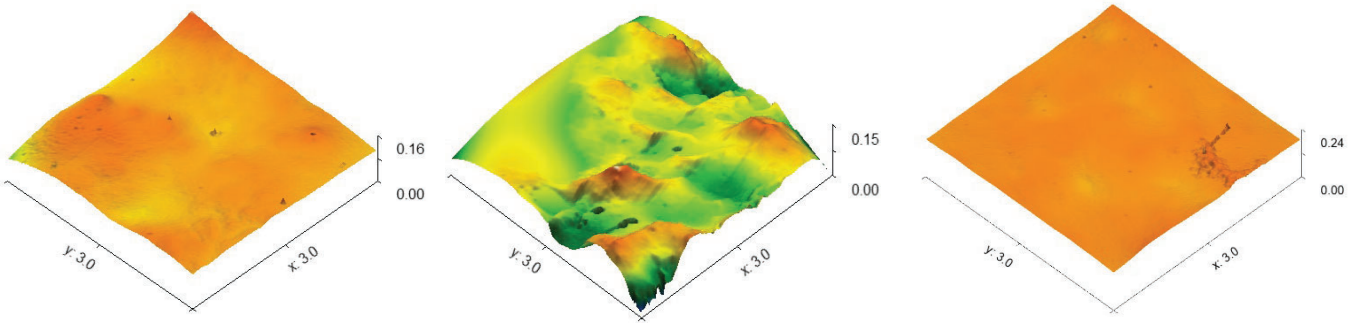

Figure 6: Three-dimensional surface topography maps of Grout A (left), Grout X (center), and Grout BC (right)

The three-dimensional surface maps, Figure 6, also showed differences in the distribution of surface features. Grout X contained larger peaks and deeper valleys, which resulted in higher roughness values. Grout A had a more uniform surface with smaller height variations. Grout BC showed moderate surface variation compared with Grout A and Grout X.

5.2 Surface Wettability

The water contact-angle results showed differences in surface wettability among the three grout formulations. A lower contact angle indicates better spreading of the liquid on the grout surface, while a higher contact angle indicates less favorable wetting. Better wettability may allow the liquid epoxy to spread more evenly and make closer contact with the grout surface, which can support improved bonding. However, the water contact angle was used only as a comparative indicator and does not directly measure the wetting behavior of the epoxy.

Grout A had the lowest average contact angle, at 48.8 ± 2.4°, indicating the most favorable and consistent wettability. Grout X had the highest average contact angle, at 56.2 ± 4.8°, indicating lower wettability and greater variation across the surface (Figure 7). Grout BC showed an intermediate contact angle of 52.1 ± 2.6°.

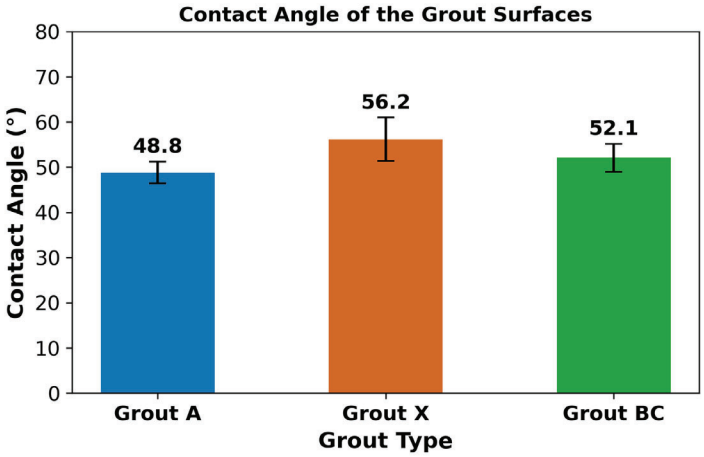

Figure 7: Average water contact angle of Grout A, Grout X, and Grout BC

The results also showed that higher surface roughness did not necessarily lead to better wettability. Although Grout X had the highest roughness, it also had the highest contact angle. Its larger surface features and surface-connected cavities may have reduced uniform liquid contact across the grout surface. Grout A showed the most favorable and consistent wetting behavior, while Grout BC showed moderate wettability between Grout A and Grout X.

5.3 Near-Surface Morphology

SEM images showed different near-surface features for the three grout formulations (Figure 8). Grout A had a relatively dense and continuous surface matrix with clustered surface features. This surface condition provided a more uniform region for epoxy contact. Grout X contained several irregular surface-connected cavities and local discontinuities. These cavities may have formed from entrapped air, differences in grout flow, incomplete consolidation, or other casting-related effects. The cavities could trap air during epoxy application and reduce uniform contact between the epoxy and grout. They may also create weak regions within the near-surface grout. Grout BC showed a finer and more fragmented surface texture with microscale heterogeneity. Although its surface was not as uniform as Grout A, it appeared to have sufficient near-surface integrity to support strong epoxy adhesion.

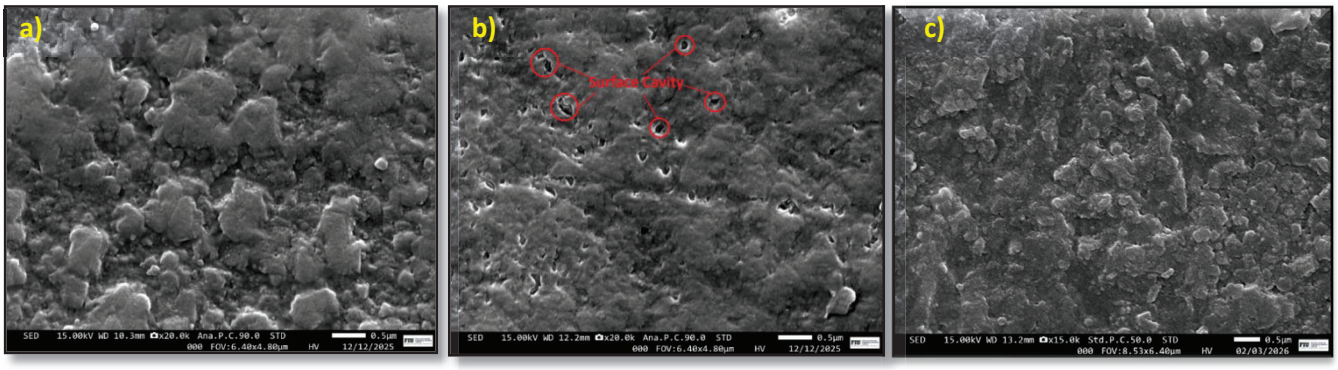

Figure 8: SEM images showing the near-surface morphology of (a) Grout A, (b) Grout X, and (c) Grout BC

Overall, the SEM observations showed that surface continuity and substrate integrity varied among the grout formulations. These differences helped explain why the roughest grout did not provide the highest adhesion strength.

5.4 Pull-Off Adhesion Strength and Failure-Mode Evaluation

The pull-off test results also showed differences in adhesion strength among the three grout formulations. Grout BC had the highest average pull-off strength of 6.37 ± 0.32 MPa. Grout A had an average strength of 5.38 ± 0.28MPa, while Grout X had the lowest average strength of 3.98 ± 1.34 MPa. Grout A produced relatively consistent adhesion results, with individual values ranging from 5.09 to 5.66 MPa. Grout X showed a wider range, from 2.72 to 5.38 MPa, which indicates greater variation in its surface and near-surface condition. Grout BC showed the highest and consistent adhesion performance among the three formulations (Figure 9).

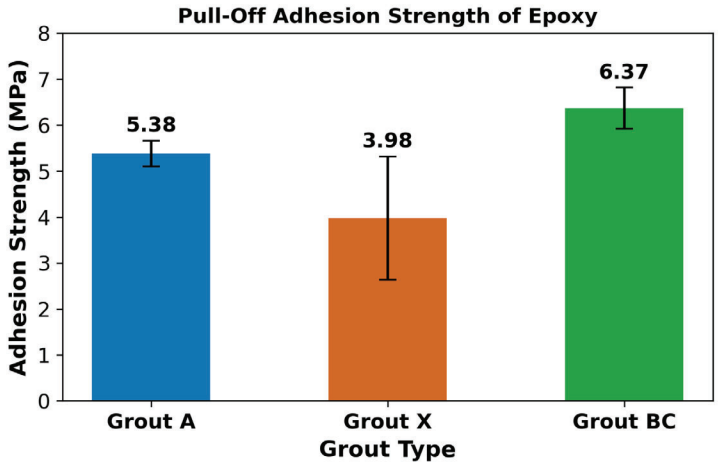

Figure 9: Average pull-off adhesion strength of epoxy coatings applied to Grout A, Grout X, and Grout BC

The failure modes also differed among the grout formulations. Grout A mainly showed adhesive failure at the epoxy–grout interface, indicating that the interface was generally the weakest region. Grout X mainly showed substrate failure within the grout. However, this did not indicate stronger adhesion because the failures occurred at lower and more variable pull-off strengths. Instead, the results suggest that the near-surface region of Grout X was weak or nonuniform, which is consistent with the surface-connected cavities observed in the SEM images (Figure 8). Grout BC showed mixed adhesive and cohesive failure involving the epoxy–grout interface and the epoxy coating. This failure occurred at the highest average pull-off strength and suggests a more balanced load transfer through the epoxy, interface, and grout.

The results did not show a direct relationship between surface roughness and adhesion strength. Grout X had the highest roughness but the lowest average adhesion strength. In contrast, Grout BC had moderate roughness and wettability but produced the highest adhesion strength. This shows that roughness alone did not control adhesion. Surface continuity, near-surface grout integrity, wettability, and the distribution of surface features also affected the epoxy–grout bond.

6. Alkaline Aging Method Development

Strong initial adhesion does not always guarantee long-term performance. During service, the epoxy coating may be exposed to high-pH chemical solutions and elevated temperatures for long periods. These conditions can allow moisture and ions to enter the coating, change the epoxy properties, weaken the epoxy–grout interface, and reduce adhesion strength over time. Therefore, an accelerated aging test is needed to evaluate the long-term durability of the epoxy coating and the epoxy–grout bond under controlled alkaline and temperature conditions.

As part of this work, two aging configurations were developed to determine which method could provide more reliable, repeatable, and controlled exposure of the epoxy-coated grout specimens.

6.1 Design requirements

The aging method was designed to represent the exposure direction of the proposed layered refurbishment system. The alkaline solution contacts the epoxy coating first, while the grout remains below the coating. Therefore, the setup needed to:

- expose a defined area of the epoxy surface;
- protect the grout sides and bottom surface from direct exposure;
- prevent leakage around the specimen;
- withstand high-pH chemical exposure;
- support controlled-temperature aging;
- allow continuous monitoring of the solution and temperatures; and
- allow specimens to be removed at selected aging times for testing.

6.2 Alkaline Waste Simulant

SRNL provided a recommended recipe for the high-pH, multicomponent alkaline waste simulant planned for the aging study. The solution was intended to represent important chemical species present in the tank environment, including hydroxide, nitrate, nitrite, carbonate, chloride, and phosphate. The proposed composition is shown in the following table.

Component	Concentration (M)
NaOH	1.09
$NaNO_3$	1.30
$Na_2CO_3 \cdot H_2O$	0.744
NaCl	0.341
$Na_3PO_4 \cdot 12H_2O$	0.0315

6.3 Method 1- Wrapped Specimen Configuration

In the first configuration, the epoxy-coated grout specimens were wrapped using either PTFE or EPDM. The wrapping covered the grout sides and uncoated regions while leaving the epoxy-coated surface exposed to the alkaline solution. A chemical-resistant adhesive was applied along the edges, corners, and joints to reduce possible leakage paths. Because this setup did not include its own heating system, the wrapped specimens would need to be placed in an oven or another temperature-controlled environment for elevated-temperature aging.

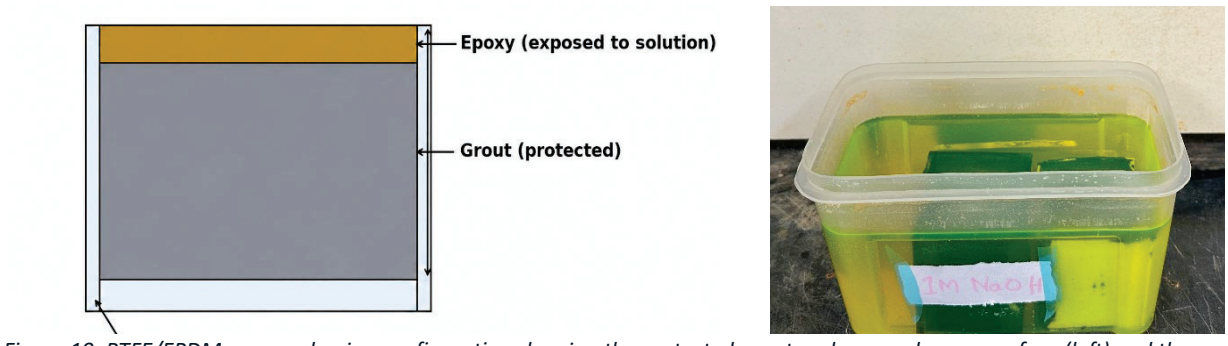

Figure 10: PTFE/EPDM-wrapped aging configuration showing the protected grout and exposed epoxy surface (left) and the wrapped specimens immersed in 1 M NaOH solution during the seven-day leakage trial (right)

A trial test was carried out to evaluate the sealing performance of the wrapped configuration. One PTFE-wrapped specimen and one EPDM-wrapped specimen were immersed in 1 M NaOH containing fluorescein sodium salt for seven days at room temperature (Figure 10). The fluorescein was used as a tracer to identify any movement of the solution through or around the wrapping. After exposure, the specimens were removed, dried for 24 hours, and the wrapping materials were carefully removed. The grout surfaces and the inner sides of the wrapping were then examined under a blue LED light with a wavelength of approximately 450–460 nm.

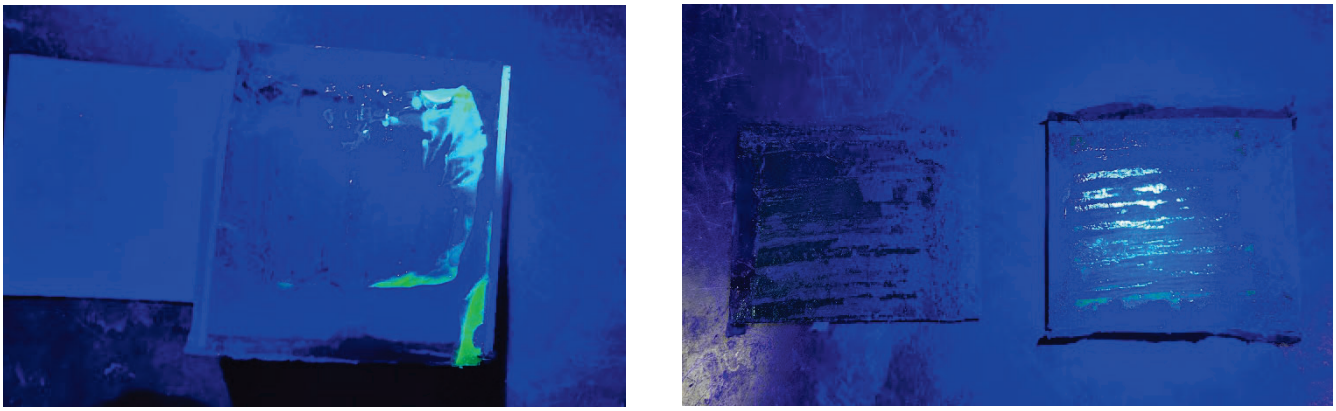

Figure 11: Bright green fluorescence detected under blue light on the grout surface (left) and the inner surface of the wrapping material (right)

Bright green fluorescence was observed on the inner surfaces of both wrapping materials and on the grout specimens, confirming that the alkaline solution had passed through or around the wrapping (Figure 11). Possible causes include incomplete sealing at the corners or joints, small gaps between the wrapping and specimen, poor bonding of the adhesive to PTFE or EPDM, movement or damage of the wrapping during immersion, and solution entry along irregular grout surfaces. The wrapped configuration also had limited repeatability because the quality of the seal depended strongly on the person preparing the specimen. Small differences in wrapping, adhesive application, corner sealing, and handling could vary from one specimen to another and create different leakage paths. Therefore, even when the same materials and procedure were used, the sealing performance could be inconsistent between specimens.

6.4 Method 2 – Top-Exposure Cylinder Configuration

The second aging method used a PTFE cylinder placed directly on top of the epoxy-coated grout specimen (Figure 12). This setup was designed to expose only a defined area of the epoxy surface while protecting the grout from direct contact with the alkaline solution. A chemical-resistant EPDM gasket was placed between the bottom of the PTFE cylinder and the epoxy-coated surface. The specimen and cylinder were positioned between top and bottom compression plates. Threaded rods, washers, and nuts were used to apply uniform pressure and maintain the seal. The alkaline solution was then added inside the PTFE cylinder so that it contacted only the top surface of the epoxy coating. The top compression plate included an access opening that was closed with a rubber stopper. This opening allowed the solution to be added, sampled, and monitored during aging without disassembling the entire setup. The rubber stopper was kept in place during exposure to reduce evaporation and prevent outside contamination. The PTFE cylinder and EPDM gasket were selected because of their chemical resistance to alkaline solutions. Compared with the wrapped configuration, this setup was designed to provide a more consistent exposed area and reduce variation caused by manual wrapping and adhesive application.

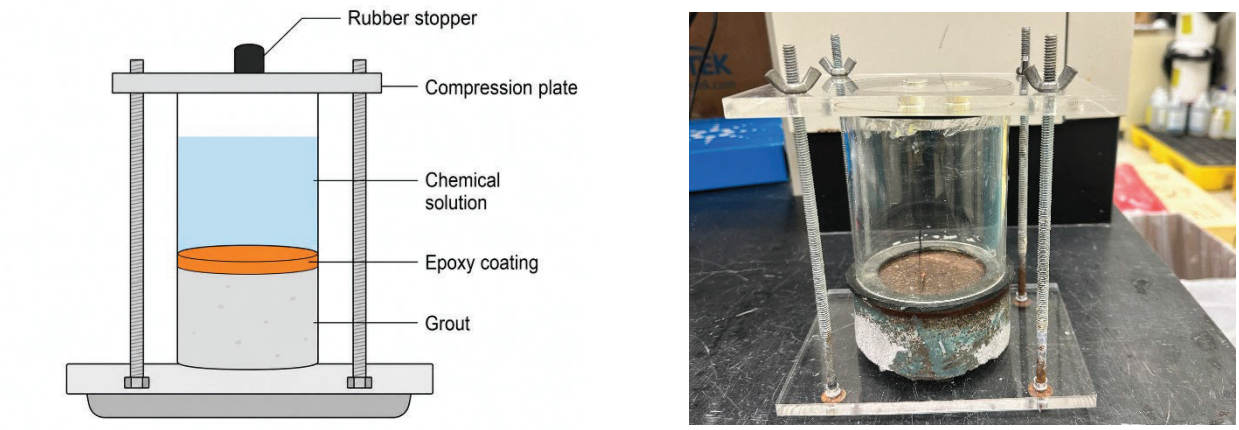

Figure 13: Top-exposure cylinder aging configuration showing the schematic design (left) and assembled experimental setup (right)

However, this configuration required an individual heating system to control the solution temperature. To provide controlled-temperature exposure, an automated temperature-control and monitoring system was integrated into the PTFE-cylinder setup (Figure 13). The system included a silicone heating pad, thermocouples, a relay, a microcontroller, and a computer for real-time monitoring and data logging. The silicone heating pad was wrapped around the outside of the PTFE cylinder to heat the solution indirectly. This avoided placing a heating element directly inside the aggressive alkaline solution. A thermocouple was used to monitor the solution temperature. The temperature readings were sent to the microcontroller, which used the relay to switch the heating pad on and off based on the set temperatures. The computer continuously displayed and recorded the temperature data during the test.

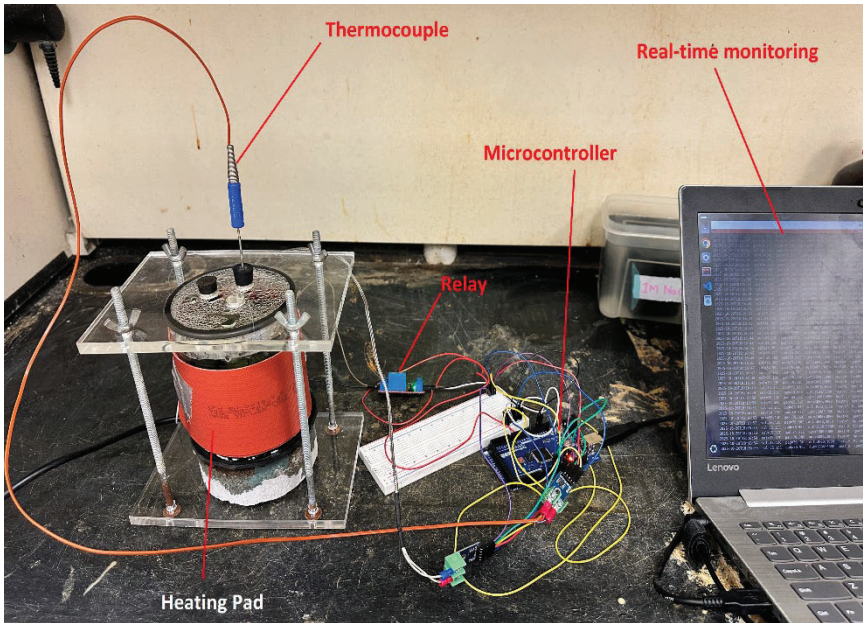

Figure 12: Automated temperature-control and monitoring system showing the heating pad, thermocouples, relay, microcontroller, and real-time temperature logging

6.5 Path Forward: Planned Long-Term Aging and Evaluation

Following completion of the aging setup development, the next phase of the work is to conduct long-term alkaline aging of both bulk epoxy specimens and epoxy-coated grout specimens. The specimens will be exposed to the SRNL-recommended alkaline waste simulant under controlled-temperature conditions for selected aging periods. Characterization will be performed at planned time intervals to monitor changes in the epoxy and the epoxy–grout interface. Bulk epoxy specimens will be evaluated using tensile and compression testing to measure changes in mechanical properties. Fourier-transform infrared spectroscopy will be used to identify possible chemical changes in the epoxy. Dynamic mechanical analysis will be used to monitor changes in stiffness, viscoelastic behavior, and glass-transition temperature. Epoxy-coated grout specimens will be tested periodically using the pull-off method to measure adhesion retention after aging. The failure surfaces will also be examined to determine whether the failure mode changes with exposure time. These measurements will help relate changes in the epoxy properties to changes in epoxy–grout adhesion.

The planned aging program will provide information on:

- changes in epoxy tensile and compressive properties;
- changes in chemical structure measured by FTIR;
- changes in dynamic mechanical properties and glass-transition temperature;
- retention of epoxy–grout adhesion strength; and
- the effect of aging time and temperature on overall system durability.

7. Key Accomplishments

The main accomplishments of the FIU portion of the project are summarized below:

- Evaluated the surface properties of three grout formulations: Grout A, Grout X, and Grout BC.
- Measured surface roughness, water contact angle, and near-surface morphology of the grout specimens.
- Measured epoxy–grout adhesion strength and identified the main failure modes for each grout formulation.
- Demonstrated that surface roughness or wettability alone did not control epoxy adhesion. Surface wettability, surface continuity, near-surface morphology, and grout integrity also affected bond performance.
- Identified Grout BC as the best-performing grout, with an average pull-off strength of 6.37 MPa
- Developed two accelerated-aging configurations for exposing epoxy-coated grout specimens to alkaline solution.
- Integrated an automated temperature-control and monitoring system into the aging setup using a silicone heating pad, thermocouples, a relay, a microcontroller, and real-time data logging.
- Presented and published selected project findings at the WM2026 Conference.

8. Publications

Selected project findings were published and presented at the WM2026 Conference, held March 8–12, 2026, in Phoenix, Arizona.

A. Hossen, M. Kranjc, K. Blue, and D. McDaniel, “Adhesion Performance of Polymeric Epoxy Coatings on Grout for Nuclear Waste Tank Refurbishment,” *WM2026 Conference*, Phoenix, Arizona, 2026.

In addition, a review journal paper was prepared and published in Nuclear Engineering and Design.

A. Hossen, M. Rayhan, M. Sarker, A. Saha, A. Hamrani, D. McDaniel, “A Systematic Review on Grout in Nuclear Waste Management: Advancement, Composition and Performance”, *Nuclear Engineering and Design,* 443 (2025); https://doi.org/10.1016/j.nucengdes.2025.114281

Appendix 2: Task 2 (Reference Electrode Development) —SRNL-STI-2026-00432

Hanford Tank Waste R&D Year 2 Report

Portion of Award #277993

Improvements to Waste Tank Reference Electrode Materials and Design

Kiana Sykes, Bruce Wiersma, Olivia Gaskin, Naim Kabir, Haley Jones

August 2026

SRNL-STI-2026-00432, Revision 0

SRNL is managed by Batelle Savannah River Alliance for the U.S. Department of Energy's Office of Environmental Management.

DISCLAIMER

Printed in the United States of America

Prepared for the U.S. Department of Energy

Hanford Tank Waste R&D Year 2 Report

Portion of Award #277993:

Improvements to Waste Tank Reference Electrode Materials and Design

Kiana Sykes, Bruce Wiersma, Olivia Gaskin, Naim Kabir, Haley Jones

August 2026

Keywords: Corrosion, Waste Tank Integrity, Corrosion Monitoring
Retention: Permanent
SRNL-STI-2026-00432, Revision 0

Savannah River National Laboratory is operated by Battelle Savannah River Alliance for the U.S. Department of Energy under Contract No. 89303321CEM000080.

Reviews and Approvals

LEAD AUTHOR:

KIANA SYKES (Affiliate) Digitally signed by KIANA SYKES (Affiliate)
Date: 2026.08.18 15:17:39 -04'00'

K. S. Sykes, SRNL/Research Scientist Date

TECHNICAL REVIEWER:

VENUS AMIRI (Affiliate) Digitally signed by VENUS AMIRI (Affiliate)
Date: 2026.08.18 16:26:57 -04'00'

Venus Amiri, SRNL/ Postdoc Research Associate Date

APPROVAL:

PAVAN SHUKLA (Affiliate) Digitally signed by PAVAN SHUKLA (Affiliate)
Date: 2026.08.18 17:01:27 -04'00'

P. K. Shukla, SRNL/Advisory Engineer, Lead Principal Investigator Date

MORGANA WHITESIDE (Affiliate) Digitally signed by MORGANA WHITESIDE (Affiliate)
Date: 2026.08.18 14:34:01 -04'00'

M. Whiteside, SRNL/Manager, Materials Science and Disposition Date

JOSEPH MANNA (Affiliate) Digitally signed by JOSEPH MANNA (Affiliate)
Date: 2026.08.18 16:55:53 -04'00'

J. Manna, SRNL/Director, Materials Technology and Energy Sciences Division Date

Preface or Acknowledgements

The authors acknowledge the U.S. Department of Energy-Environmental Management for the funding and support to conduct this research. The development of more robust reference electrodes for in-situ monitoring of tank corrosion is under the umbrella of a program that was initiated as part of the “R&D Roadmap for Hanford Tank Waste Mission Acceleration” (NNLEMS-2022-00005).

Executive Summary

The Hanford site is responsible for the safe storage of over 200 million liters of radioactive and chemically hazardous waste, contained within 177 underground carbon-steel tanks. These tanks, comprising 149 single-shell tanks (SSTs) and 28 double-shell tanks (DSTs), are essential for interim storage and waste retrieval prior to vitrification at the Waste Treatment and Isolation Plant (WTP). With tank service life requirements now far exceeding their original 40-year design, robust corrosion monitoring and control practices are imperative to ensure long-term integrity and environmental safety. Since 2008, reference electrodes have been used to monitor corrosion potential in select DSTs; however, of the 45 electrodes installed, 29 have failed and 6 have provided unreliable results, underscoring the need for more durable solutions.

To address this challenge, the U.S. Department of Energy's Office of Environmental Management (DOE-EM) is sponsoring a three-year research and development program to create a chemical and radiation-resistant reference electrode specifically for Hanford tank applications. The first year of the program focused on diagnosing failure mechanisms and identifying candidate materials for improved electrode construction. In the second year, the program objectives included testing these materials under simulated waste conditions, designing enhanced electrode components, fabricating prototype materials, and assembling reference electrode prototypes for accelerated testing.

Key advancements have been made in the selection and testing of critical electrode components, particularly the junction material, casing, and inner chamber backfill. Nine candidate junction materials, including various polymers and ceramics, some produced via 3-D printing, were evaluated for their resistance to contaminant permeation. Porous polyvinylidene fluoride and Alumina has emerged as a promising candidate for further development. Commercial casing materials have performed well, and 3-D printing is being explored to further enhance fabrication consistency and material performance.

Design improvements have also been implemented, such as lengthening and complicating the internal path between the junction and the sensing wire to reduce contaminant intrusion, guided by finite element modeling to maintain measurement accuracy. With commercial vendor collaboration, these optimized materials and design features were integrated into prototype reference electrodes. Upon completion, recommendations for robust reference electrode materials and designs will be provided to support the long-term corrosion monitoring and structural integrity of Hanford's critical tank infrastructure. Should this project gain more funding in the future, the next steps would include comprehensive testing of the assembled product in a chemical waste simulant, monitoring the open circuit potential (OCP) over time, and comparing the performance to that of commercial reference electrodes

Table of Contents

1.0 Introduction 1
2.0 Delivery of Year 2 Milestones 2
3.0 Conclusions 11
4.0 References 11

List of Tables

Table 1. Materials matrix for reference electrode junction..... 2

List of Figures

Figure 1. Diagram of the onset of localized corrosion or SCC when the OCP exceeds the repassivation potential or the critical cracking potential..... 1

Figure 2. Schematic of H-cell set up using sodium hydroxide and tap water..... 3

Figure 3. pH unit difference over time with various materials at room temperature..... 4

Figure 4. Material after H-cell testing..... 5

Figure 5. pH unit difference over time with various materials at elevated temperatures..... 5

Figure 6. Tortuous path schematic..... 6

Figure 7. Time scale associated with the diffusion of a species vs. number of baffles, where m is the factor by which the baffle diameter is reduced with respect to the reference electrode inner diameter..... 6

Figure 8. Percent error potential measurements vs. number of baffles, where m is the factor by which the baffle diameter is reduced with respect to the reference electrode inner diameter..... 7

Figure 9. Schematic of reference electrode prototype with baffles..... 7

Figure 10. Diffusion of potassium permanganate in water with reference electrode casing with no baffles (left) and with baffles (right)..... 8

Figure 11. Diffusion of potassium permanganate in water with reference electrode casing with baffles..... 8

List of Abbreviations

SRNL	Savannah River National Laboratory
DST	Double-Shell Tanks
OCP	Open Circuit Potential
CPP	Cylic Potentiodynamic Polarization
SST	Single-Shell Tanks
WTP	Waste Treatment Plant
SCC	Stress Corrosion Cracking
PVDF	Polyvinylidene Fluoride
AM	Additive Manufacturing
PEKK	Polyetherketoneketone

1.0 Introduction

The Hanford tank farm facility is responsible for the safe storage of approximately 200 million liters of radioactive and chemically hazardous wastes, relying on robust corrosion monitoring to ensure the long-term integrity of its 177 underground carbon-steel storage tanks. Of these, 149 are single-shell tanks (SSTs) and 28 are double-shell tanks (DSTs) [1]. The DSTs, serving as interim storage prior to waste vitrification at the Waste Treatment Plant (WTP), have been in service for 38 to 56 years, well beyond their original 40-year design life [2]. With waste retrieval operations projected to continue until at least 2075, maintaining effective corrosion control practices is essential to ensure structural integrity and safe operation [1].

A key component of the Hanford site's structural integrity program is the use of electrochemical techniques specifically, the measurement of open circuit potential (OCP) or corrosion potential (Ecorr) of tank materials in contact with waste. The OCP provides valuable insight into corrosion behavior, including passivity and susceptibility to localized attack or stress corrosion cracking (SCC). For DSTs, particular attention is given to localized corrosion and SCC, both of which can be conservatively assessed by monitoring when the tank steel's OCP exceeds critical thresholds such as the repassivation potential (Erp) or the critical cracking potential (CCP) (Figure 1). While laboratory tests using tank waste simulants or actual tank waste are commonly used to establish these electrochemical parameters, in-tank OCP measurements offer the significant advantage of capturing the real-world effects of tank wall steel inclusions and long-term waste contact. However, interpreting OCP data is complex due to the simultaneous anodic and cathodic reactions occurring on the steel surface.

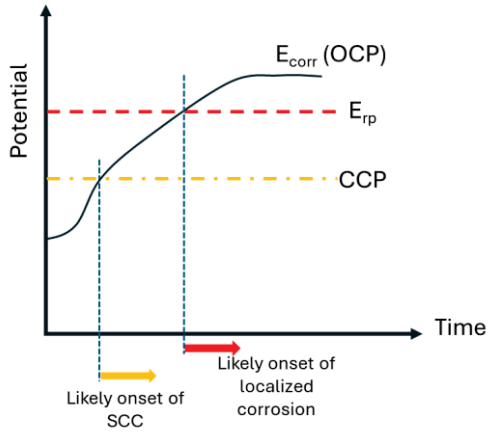

Figure 1. Diagram of the onset of localized corrosion or SCC when the OCP exceeds the repassivation potential or the critical cracking potential.

Since 2008, Hanford's structural integrity program has employed reference electrodes for in-situ OCP monitoring [1,3]. However, a persistent challenge has been the long-term stability of these electrodes in the aggressive waste chemistry environment. Failures have been observed within 2-3 years of deployment, primarily due to the ingress of contaminants, especially hydroxide ions, from the tank waste into the internal components of the reference electrode via the junction material [4]. This contamination alters the electrode's potential readings and limits the effectiveness of the monitoring program. The junction material, located at the interface between the tank waste and the internal chamber of the reference electrode, is critical to performance. It must allow ionic transport for accurate potential

measurement while minimizing the junction potential, maintaining a steady electrolyte flow, and resisting chemical attack [5]. Importantly, it must also prevent the intrusion of contaminants from the waste. Identifying and implementing an improved junction material is key to extending reference electrode service life and enhancing reliability [5].

The objective of this Year End Report is to summarize progress and technical achievements for Year 2 of the Hanford Tank Waste R&D project, "Improvements to Waste Tank Reference Electrode Materials and Design". The focus of Year 2 has been on advancing the materials and design of reference electrodes to address the challenges of long-term stability in tank waste environments. The following milestones were established and achieved:

1. **Thorough Screening and Validation of Advanced Junction Materials:**
   Conducted an extensive evaluation of a diverse range of candidate junction materials using systematic and accelerated testing protocols. The focus was on identifying materials that demonstrate superior chemical inertness, maintain a consistently low junction potential, and provide robust resistance to contaminant ingress ensuring long-term stability and accuracy of reference electrode performance in highly aggressive tank waste environments.

2. **High-Precision Fabrication and Rigorous Qualification of Test Assemblies:**
   Utilized advanced manufacturing techniques to fabricate high-tolerance components and assemblies, enabling the execution of controlled, repeatable materials testing. All testing was performed under conditions that closely simulate actual tank service, ensuring the reliability and relevance of performance data for real-world applications.

3. **Prototype Development through Strategic Industry Collaboration and Innovative Engineering:**
   Partnered with leading industry experts to design, assemble, and refine prototype reference electrodes incorporating state-of-the-art materials and novel engineering solutions. These prototypes were developed with a focus on enhancing operational durability, minimizing maintenance requirements, and optimizing performance in the uniquely challenging chemical and radiological environment of Hanford tank waste storage.

The advancements achieved in Year 2 represent significant progress toward the development of robust, long-lasting reference electrodes for Hanford tank waste monitoring. Through targeted materials research, precision fabrication, and collaborative prototype development, the project is addressing key challenges and laying the groundwork for improved corrosion monitoring practices, critical to the long-term safety and integrity of the Hanford tank farm facility.

2.0 Delivery of Year 2 Milestones

The materials listed in Table 1 have undergone laboratory testing to determine their efficiency and stability as junction material. An H-cell set up was used to monitor the pH changes across the candidate materials. More specifically, the set up included tap water on one side of the H-cell and 3 M sodium hydroxide on the other, as shown in Figure 2. The candidate junction materials were placed in the middle compartment of the cell so that sodium hydroxide would permeate through the frit. Silicon gaskets were placed on each side to prevent leaks. The pH was measured using a standard calibrated pH probe. Sodium hydroxide was chosen for testing because it has been found to cause failures of previous reference

electrodes. Therefore, a material with tendency to minimize hydroxide permeation will limit the number of failures.

Table 1. Materials matrix for reference electrode junction

Nafion - a brand name for a sulfonated tetrafluoroethylene based fluoropolymer-copolymer.
NASICON – Na (sodium) super ionic conductor, family of solid ceramic materials.
Polyvinylidene Fluoride – PVDF, thermoplastic fluoropolymer.
Alumina – Aluminum oxide.

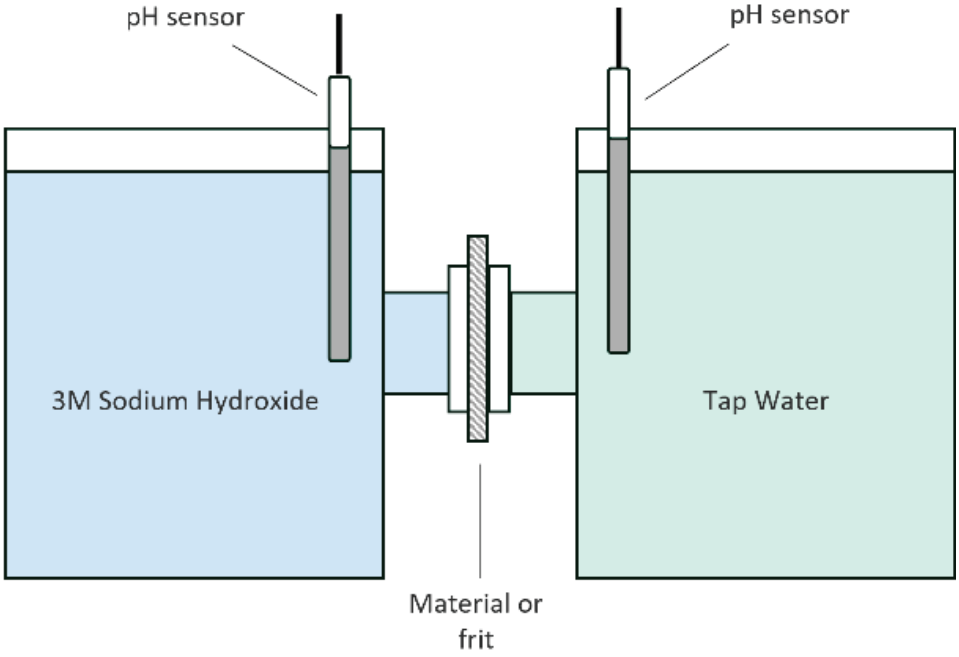

Figure 2. Schematic of H-cell set up using sodium hydroxide and tap water.

Nine materials were tested over a span of 8 days, with pH change for the tap water tracked and monitored for each. The pH change in the tap water was measured relative to its starting pH to determine the extent of ion transport. The side with tap water was of interest because of the natural diffusion of dissolved sodium hydroxide from an area of high concentration to low. Because an ideal material is expected to minimize the permeation of contaminants, smaller pH changes were more desirable. The H-cell test results at room temperature are shown in Figure 3. NASICON material is not included in this graph because less than 24 hours into the experiment it disintegrated and thus was not tested for further use.

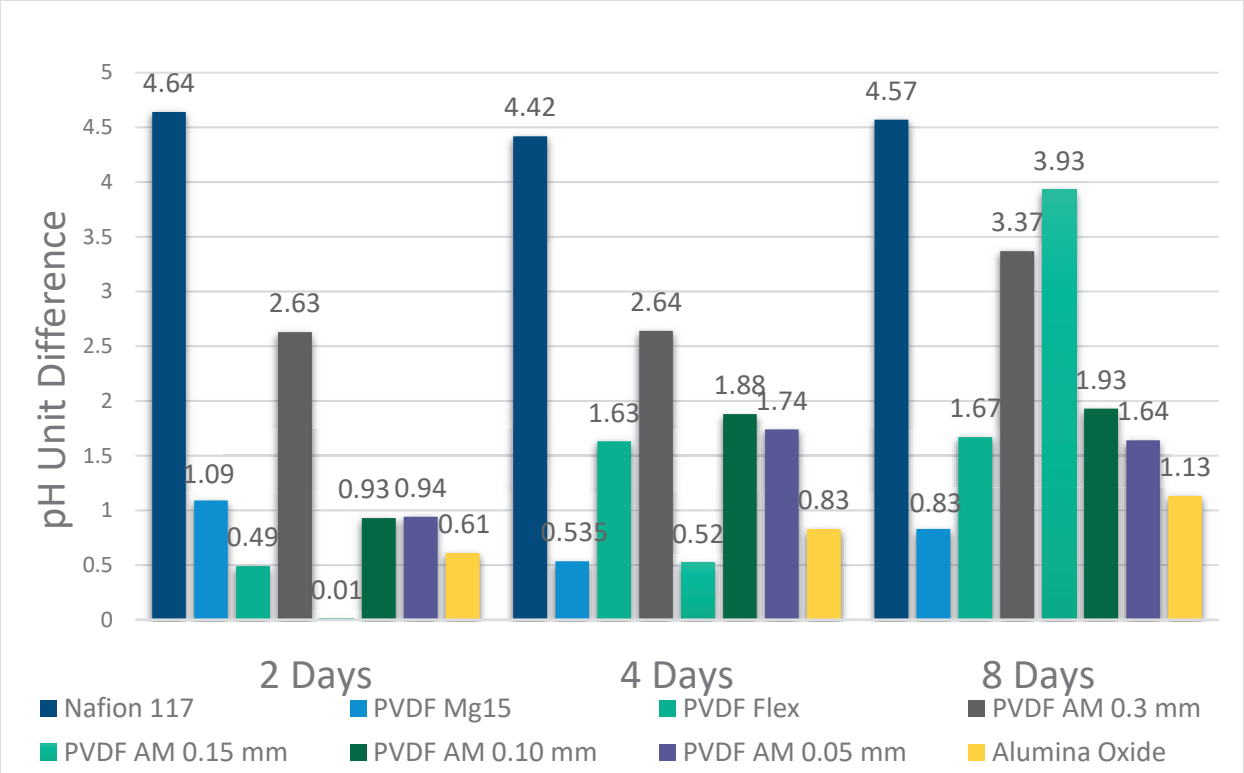

Figure 3. pH unit difference over time with various materials at room temperature.

Nafion 117 performed poorly in the highly caustic environment, having the highest pH difference of the materials tested. Future testing of this material will not be considered further. In contrast, alumina oxide showed small consistent pH changes over time, more specifically, on day eight only showed a 1.13 pH unit difference. Polyvinylidene fluoride (PVDF) MG15, a vendor-supplied, low-porous homopolymer, shows consistently small perturbations when measuring the pH. PVDF Flex, also supplied by a vendor, is a flexible copolymer with larger pore sizes also exhibited small perturbations, albeit somewhat larger than MG15.

Additional additive manufactured (AM) PVDF materials with various layer heights were tested. In AM, the layer height is the thickness of each individual layer of material, affecting the material quality, strength and porosity. Thinner layers provide higher resolution and smoother surface finish, while thicker layers print faster but have the potential for poorer adhesion. Larger layer heights also typically cause an increase in porosity [6,7]. Here, the difference of the layer heights can be observed in correlation with the pH difference in the H-cell measurements. The smaller layer heights of 0.10 mm and 0.05 mm consistently demonstrate a lower pH difference and ion diffusion; after 8 days, the pH increase was less than 2. In comparison, the larger layer heights of 0.15 mm and 0.3 mm were associated with a pH change between 3 and 4 by day 8.

The comparison of the physical differences of the materials before and after testing also provide more insight in chemical inertness and lifespan. In Figure 4, the PVDF materials are shown after the testing, with the first row showing the side exposed to the tap water, and the second row showing the side exposed to the sodium hydroxide. The tap water sides generally show limited to no discoloration on any of the materials, but discoloration can be identified on the side exposed to the sodium hydroxide. The Flex, MG15 and lower layer height PVDF show slight discoloration, but the larger layer height material shows

pronounced discoloration. The color change could be caused by a chemical reaction,dehydrofluorination, that is known to degrade the polymer backbone over time [8]. No color change is observed for Alumina.

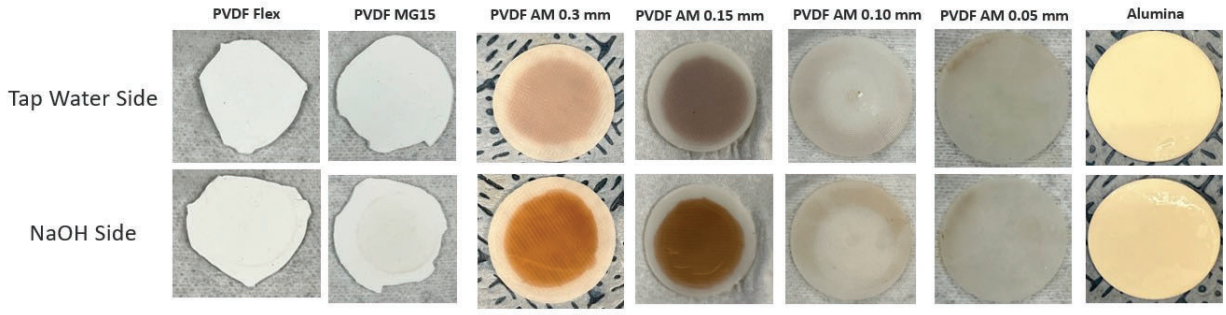

Figure 4. Material after H-cell testing.

Temperature conditions affect the mobility of hydroxide ions through the material, as well as the degree of dehydrofluorination, and additional analysis is required for material selection. Testing at 30 and 70 °C, which are representative temperatures of the waste environment in the Hanford double shell tanks, was conducted on select materials that performed above average in the room temperature tests. Alumina, PVDF MG15, PVDF Flex, and PVDF AM 0.05 mm were tested at the elevated temperatures. Alumina maintained the lowest pH unit different over the course of 8 days at 30 °C in comparison to the other materials. However, at 70 °C the pH unit difference for Alumina substantially increased. At 70 °C, the water in the H-cell was evaporating out over the course of the experiment. The H-cell was sealed, however through the experiment the water kept falling below the water line over time. This would likely cause the pH to appear higher if the water is evaporating out over the course of the experiment. The tests at 70 °C would likely need to be repeated and account for evaporation before any conclusions on the materials could be made. The tests at 30 °C did not appear to have evaporation issues as the water remained at the water line throughout the course of the experiment. More test should be done at 70 °C to fully understand the permeability of hydroxide at elevated temperatures.

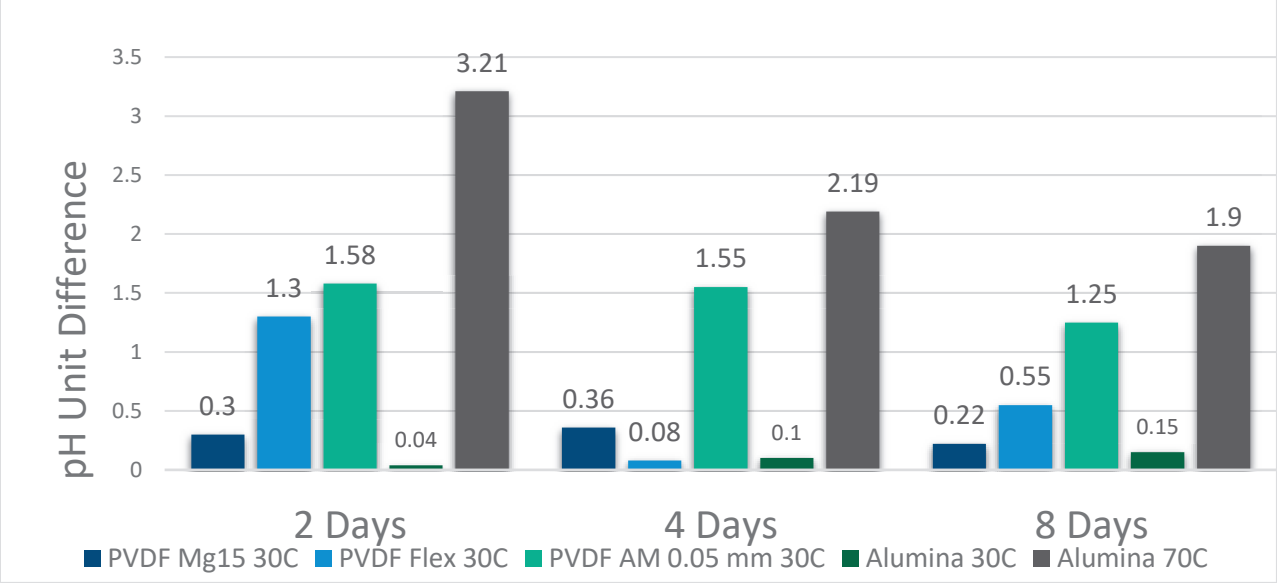

Figure 5. pH unit difference over time with various materials at 30 and 70 °C.

To address the problem of tank waste intrusion, the prototype reference electrode design elongates the chemical path between the junction material and the Ag/AgCl sensing element. Implementation of an internal baffled tortuous path provides further hindrance by slowing the diffusion of contaminant ions (Figure 6). Alongside physical changes to the reference electrode, the properties of the fill solution will be selected to also impede contaminant ions.

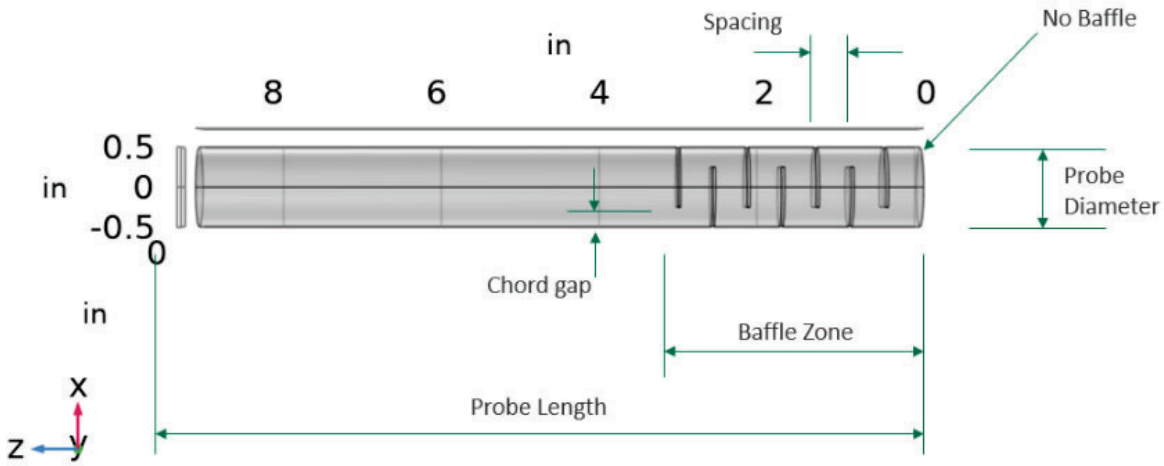

Figure 6. Tortuous path schematic of an enhanced reference electrode design.

A finite element model using COMSOL was used to investigate the effect of baffle size and number on the diffusion time from the electrode junction to the sensing wire. Figure 7 shows when baffle size is 75% or greater of the reference electrode inner diameter, the diffusion time increases by a factor of three to four with 4-5 baffles. This increase in diffusion time is expected to correlate with an increased reference electrode lifetime, resulting in a lifespan of greater than 10 years.

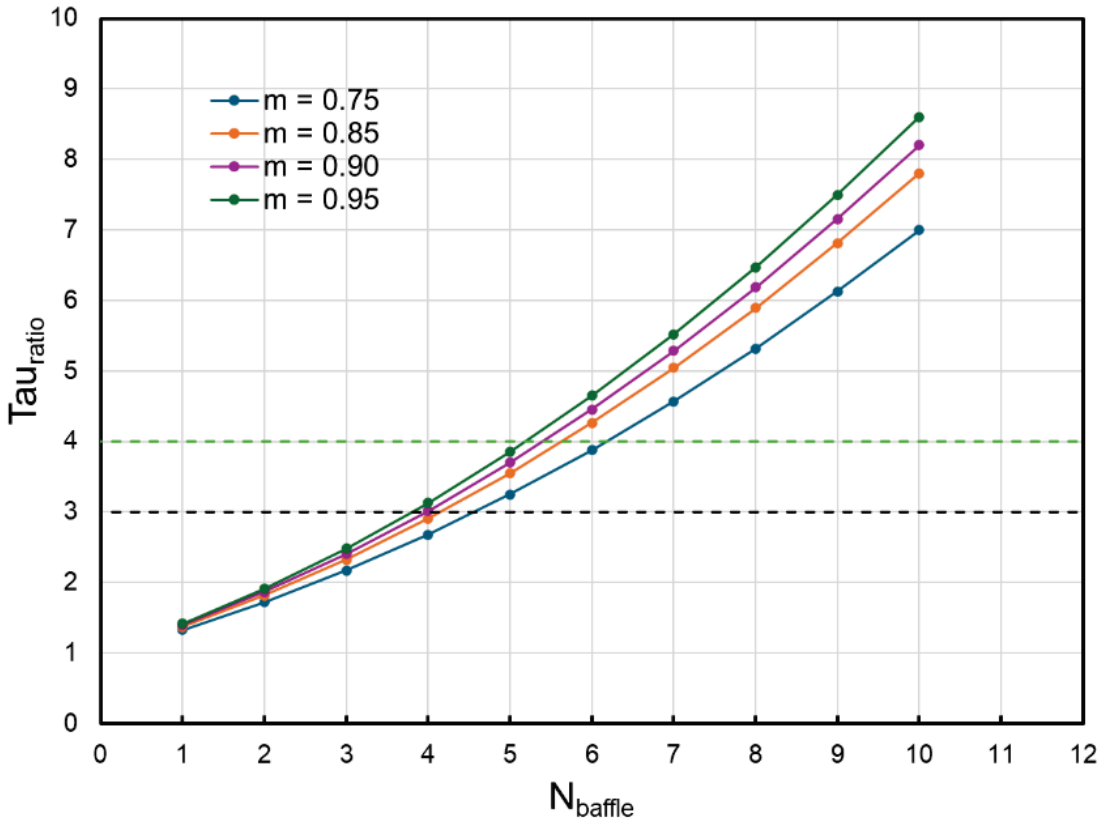

Figure 7. Time scale associated with the diffusion of a species vs. number of baffles, where m is the factor by which the baffle diameter is reduced with respect to the reference electrode inner diameter.

It is recognized that an increase in the distance and tortuosity of the diffusion path may have an adverse impact on the resistance, affecting the accuracy of the potential measurement. A second finite element model was performed to assess the effects of the baffle arrangement on the potential measurements. As shown in Figure 8, the error in the potential measurement with the same baffle configuration, as described above, is less than 0.1%. Thus, the baffles are anticipated to increase reference electrode lifetime without compromising accuracy.

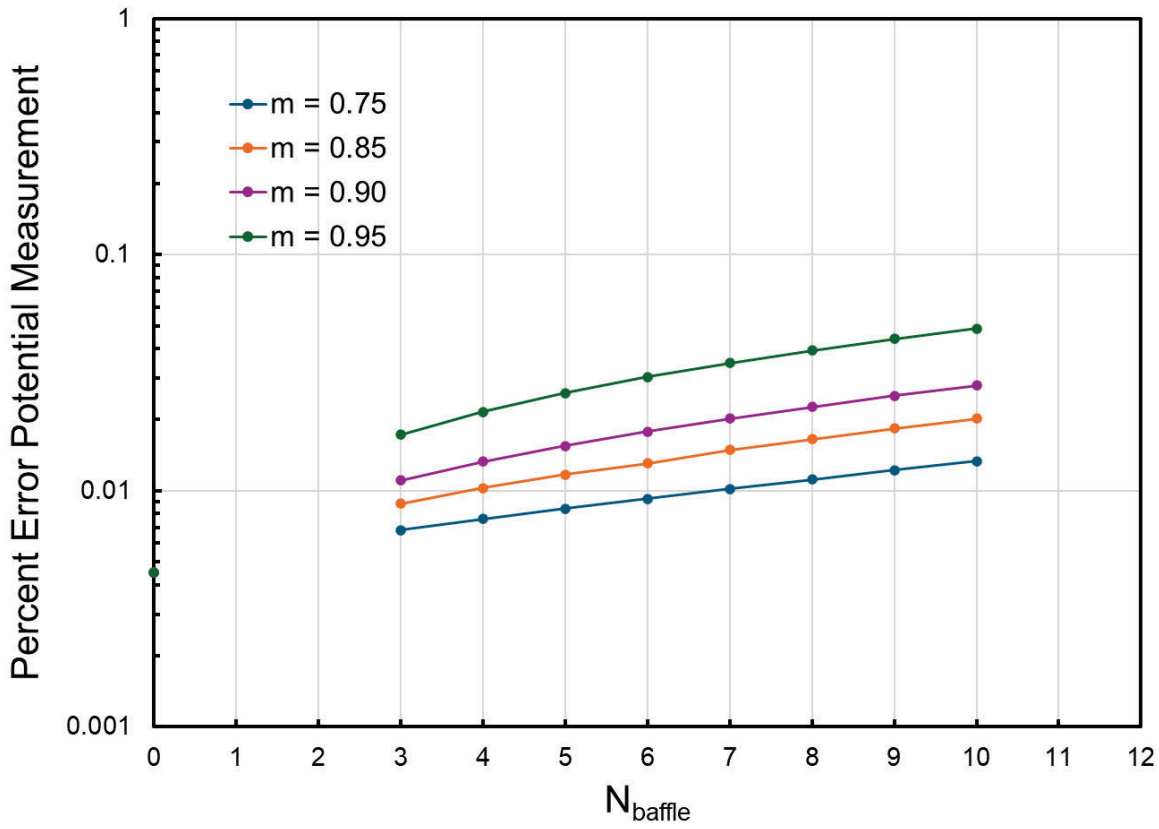

Figure 8. Percent error potential measurements vs. number of baffles, where m is the factor by which the baffle diameter is reduced with respect to the reference electrode inner diameter.

Constructed from AM Somos Waterclear 10122 from TriMech, the prototype aimed to increase the distance in the electrode to the transducer using baffles. The prototype was designed with a clear transparent material to showcase the baffles. Borin is currently manufacturing a prototype printed by Trimech made from polyether ketone ketone (PEKK), for its strong chemical resistance. This prototype was sent to Borin for them to fully assemble the working product using SRNL's design (Figure 9).

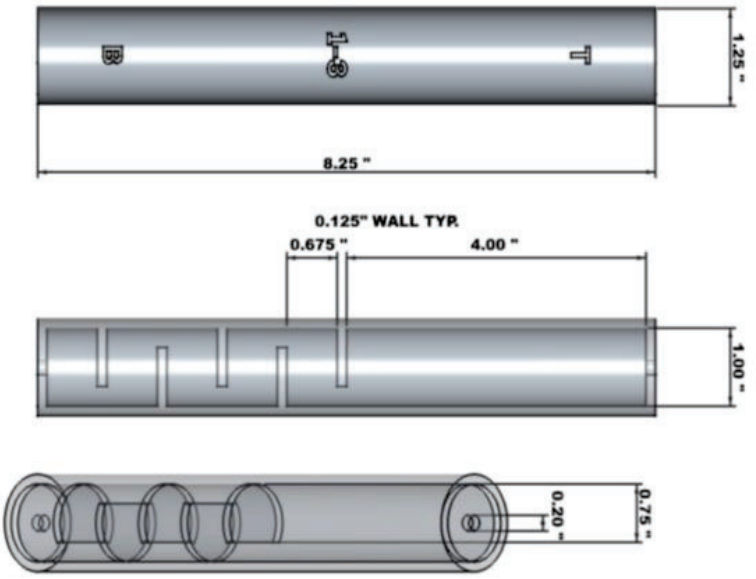

Figure 9. Schematic of the reference electrode prototype with baffles.

To evaluate the prototype's ability to impede diffusion, 10 µL of sodium permanganate solution, a highly pigmented compound, was injected into the clear prototypes and compared to a control prototype with no baffles. The prototype containing baffles slowed diffusion by approximately 30 times compared to the control, demonstrating the effectiveness of the tortuous path design. In the absence of baffles, the potassium permanganate solution diffused to the bottom in less than 60 seconds (Figure 10). In contrast, with baffles present, it took 45 minutes for the solution to reach the bottom (Figure 11). These results confirm that the baffles effectively inhibit diffusion. This test validates that incorporating baffles will enhance the longevity of the reference electrode by restricting the diffusion of contaminant species to the sensing wire, thereby extending its operational lifetime.

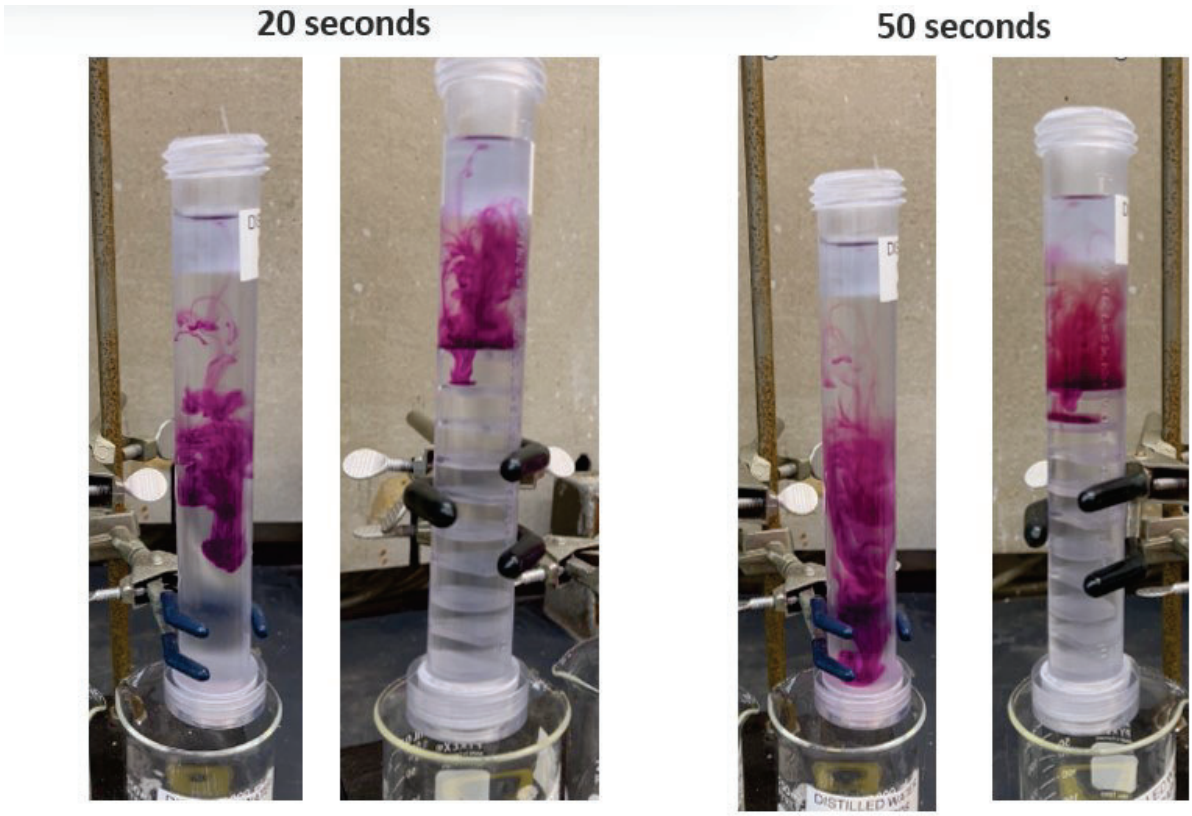

Figure 10. Diffusion of potassium permanganate in water with reference electrode casing with no baffles (left) and with baffles (right).

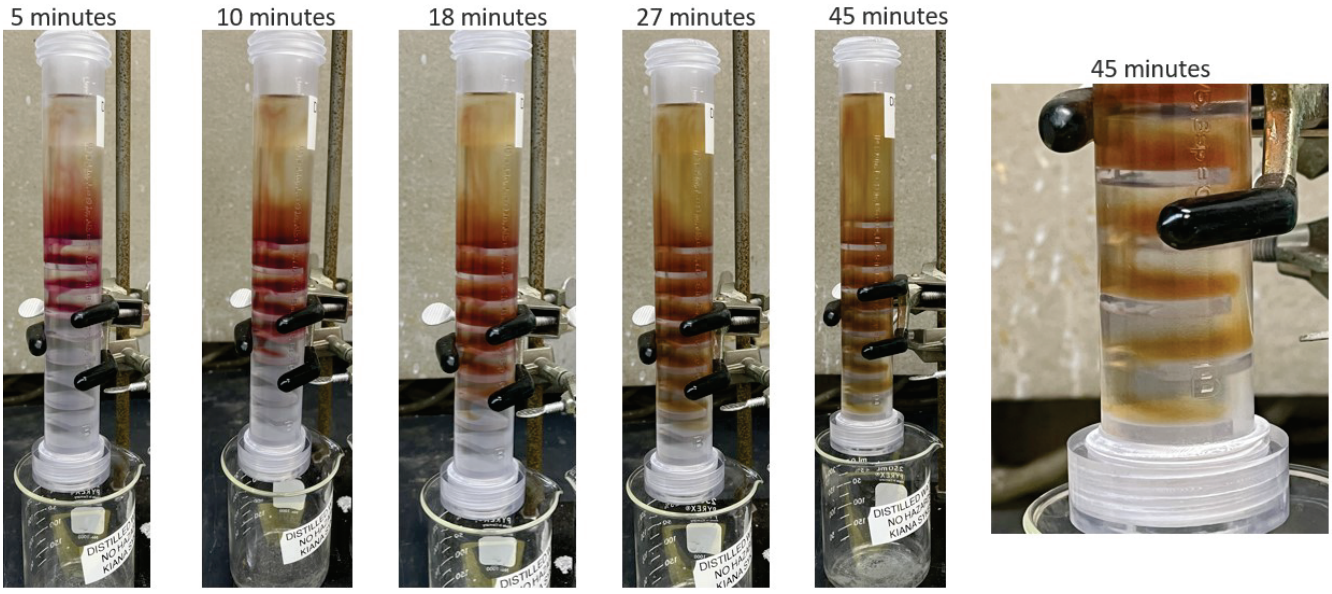

Figure 11. Diffusion of potassium permanganate in water with reference electrode casing with baffles.

3.0 Conclusions

The DOE-EM has initiated a research program aimed at developing reference electrodes capable of withstanding the harsh conditions of waste tank environments for extended periods, thereby improving confidence in system performance. Junction materials testing using an H-cell identified two promising candidates for the junction material: Alumina and PVDF MG15. Following consultation with the external additive manufacturing vendor Trimech, several prototype bodies were fabricated using both a transparent material and PEKK. The transparent prototypes were utilized to visually demonstrate the effectiveness of the baffles and diffusion using a highly pigmented chemical. Prototypes printed with PEKK were packaged and sent to Borin, a leading manufacturer of reference electrodes, for final assembly. Assembly of these prototypes at Borin is currently ongoing. Unfortunately, funding for this project has been withdrawn.

Should the project resume in the future, the next steps would include comprehensive testing of the assembled prototype reference electrodes in a chemical waste simulant, monitoring the open circuit potential (OCP) over time, and comparing the performance to that of commercial available reference electrodes.

4.0 References

[1] C. L. Girardot, RPP-7574, Rev. 8, "Double-Shell Tank Integrity Program Plan", August 10, 2021.

[2] Parsons, *Final Report: Waste Treatment and Immobilization High Level Waste Treatment Analysis of Alternatives.* Richland: Office of River Protection, 2023.

[3] M. M. Dahl and R. J. Crosswhite, RPP-RPT-51766, Rev. 41, *Corrosion Probe Monitoring Systems: January through March 2024 Quarterly Report*, May 2024.

[4] K. Evans, et al., In-Tank Corrosion Probes: DNV laboratory evaluations of reference electrodes, Presentation at the Tank Integrity Expert Panel Corrosion Subgroup Meeting, Denver, CO, March 2023.

[5] K. S. Sykes, J. Jiang, B. J. Wiersma, S. Chawla, N. Sridhar, K. Evans, and J. A. Beavers, "*Design and Materials of Reference Electrodes for Radioactive Waste Tank Service – A Literature Review,"* SRNL-STI-2024-00539, Rev. 0, November 2024.

[6] J. Brackett, D. Cauthen, J. Condon, T. Smith, N. Gallego, V. Kunc, and C. Duty, *"The impact of infill percentage and layer height in small-scale material extrusion on porosity and tensile properties,"* Additive Manufacturing, 2022, **58**(15): 103063.

[7] J.A. Choren, S.M. Heinrich, M.B. Silver-Thorn, "*Young's modulus and volume porosity relationships for additive manufacturing applications,"* J. Mater. Sci., 2013, **48**(15), 5101-5112.

[8] J. Sharma, C. Totee, V. Kulshrestha, and B. Ameduri, *"Spectroscopic evidence and mechanistic insights on dehydrofluorination of PVDF in alkaline medium,"* European Polymer Journal. 2023, 201, 11280.

Appendix 3: Task 3 (Cathodic Protection System) — SRNL-STI-2026-00371

Cathodic Protection Modeling for Hanford Underground Double-Shell Tank Farms

Anna L. d'Entremont, Pavan Shukla, Andrew Nordquist

August 2026

SRNL-STI-2026-00371

SRNL is managed by Batelle Savannah River Alliance for the U.S. Department of Energy's Office of Environmental Management.

DISCLAIMER

Printed in the United States of America

Prepared for
U.S. Department of Energy

SRNL-STI-2026-00371
Revision 0

Keywords:

Retention: *Varies (Track number is applicable)*

Cathodic Protection Modeling for Hanford Underground Double-Shell Tank Farms

Anna L. d'Entremont, Pavan Shukla,
Andrew Nordquist

August 2026

Savannah River National Laboratory is operated by Battelle Savannah River Alliance for the U.S. Department of Energy under Contract No. 89303321CEM000080.

REVIEWS AND APPROVALS

AUTHORS:

ANNA D'ENTREMONT (Affiliate) Digitally signed by ANNA D'ENTREMONT (Affiliate)
Date: 2026.08.18 13:25:23 -04'00'

Anna L. d'Entremont, Materials Science and Disposition, SRNL Date

PAVAN SHUKLA (Affiliate) Digitally signed by PAVAN SHUKLA (Affiliate)
Date: 2026.08.18 13:38:00 -04'00'

Pavan Shukla, Materials Science and Disposition, SRNL Date

TECHNICAL REVIEWERS:

RODERICK FUENTES (Affiliate) Digitally signed by RODERICK FUENTES (Affiliate)
Date: 2026.08.18 14:28:05 -04'00'

Roderick E. Fuentes, Materials Science and Disposition, SRNL Date

APPROVAL:

MORGANA WHITESIDE (Affiliate) Digitally signed by MORGANA WHITESIDE (Affiliate)
Date: 2026.08.18 14:35:35 -04'00'

Morgana T. Whiteside, Manager: Materials Science and Disposition, SRNL Date

JOSEPH MANNA (Affiliate) Digitally signed by JOSEPH MANNA (Affiliate)
Date: 2026.08.18 15:12:54 -04'00'

Joseph Manna, Director: Materials Technology and Energy Sciences Division, SRNL Date

PREFACE OR ACKNOWLEDGEMENTS

The authors appreciate the contributions of Ben Barkai, who was a member of the SRNL team carrying out technical work and interfacing with the modeling subcontractors throughout most of this project but left SRNL prior to the drafting of this report, and Crystal Girardot, who provided Hanford documents and drawings.

EXECUTIVE SUMMARY

Hanford stores millions of gallons of radioactive and chemically hazardous waste from the production of weapon materials in tank farms consisting of underground carbon-steel storage tanks surrounded by reinforced concrete. Six of these Hanford tank farms use double-shell storage tanks (DSTs). The DST farms were constructed from 1968 to 1986 with a planned 40–50 year design life, so some are already operating beyond their initial life expectancy. Ultrasonic testing (UT) has indicated significant thinning on the bottom of the secondary (outer) liner of these tanks, believed to arise from groundwater intrusion driving concrete-side corrosion.

There is no direct access to the steel/concrete interface between the tank and the concrete pad, making it difficult to apply a chemical-based mitigation strategy or to conduct repairs, but cathodic protection (CP) is a possible method to inhibit further concrete-side corrosion. Hanford already uses CP to protect below-grade steel piping within the tank farms and connected to the tanks, but this system was not designed to protect the tank bottoms. CP design must account for the structures surrounding the DSTs, including the steel reinforcing bars (rebar) within the concrete pad and vault, various process lines, and the existing CP system.

In this study, finite element analysis (FEA) modeling was carried out to simulate CP protection of 1) a single tank and CP anode to develop options for modeling the rebar and to compare to a simpler circuit model and 2) the entire Hanford AN tank farm as a representative example consisting of seven tanks, associated piping, and both existing and new CP anodes.

Both circuit and FEA models predict that significant protective current could be delivered to the bottoms of the tanks with the addition of tank-protection anodes below the depth of the tanks. Simulations with only the existing pipe-protection anodes active confirmed that only a very small current to the tank bottoms is predicted under present conditions.

Multiple simplified representations of the dome and wall rebar were tested to reduce the computational complexity of the tank-farm simulations, resulting in modeling the rebar as edge elements with a prescribed effective circumference that matches the real rebar surface area. The geometry of the rebar is also simplified into horizontal hoops around the tank walls and radial rebar over the dome with increased effective circumference to retain the target surface area. This simplification was found to greatly reduce the complexity and solution time of the models without large changes in current distributions, especially to the tank bottom.

A range of values were tested for model parameters such as soil and concrete resistivities and polarization resistance to investigate their impact on the current and electric potential distributions. Depending on the parameters used, FEA simulations predict some risk of overprotection, particularly on the piping system; since overprotection can also lead to surface damage associated with hydrogen gas generation at the interface (e.g. hydrogen embrittlement or damage to coatings), this needs to be considered when refining the design of the new CP system.

Comparison between the FEA models and the circuit model representation demonstrated that the circuit model could not match the predicted FEA current distribution, even when using the exact same surface areas. This discrepancy appeared to be at least partly attributable to the impact of the relative positions of the tank components and anodes to each other and to the ground surface. The FEA model accounts for the relative positions since it solves the governing equations in three dimensions, but the circuit model cannot account for the positioning. In particular, the circuit model underpredicts the current to the tank bottom and overpredicts the current to the dome compared to FEA for the baseline geometry.

The FEA models omitted the electrically isolated rebar in the bottom concrete slab. However, a circuit-based stray current model estimated that only 2.1% of the total current through the slab would stray into the rebar, corresponding to ~0.21 A for a target current density of 2 mA/ft^2 to the tank bottom. The estimated

corrosion driven by this amount of stray current is predicted to yield a lifetime of >400 years for the minimum rebar diameter, assuming an acceptable cross-section area loss of 10%.

TABLE OF CONTENTS

LIST OF TABLES x
LIST OF FIGURES xi
LIST OF ABBREVIATIONS xiii
1.0 Introduction 1
2.0 Background 1
2.1 Corrosion of steel in contact with soil/concrete and cathodic protection 1
2.2 Hanford Waste Tanks 3
2.2.1 Waste transfer system 5
2.2.2 Integrity assessments and evidence of corrosion 5
2.2.3 Different Hanford Tank Farms 6
2.2.4 Existing cathodic protection system for piping 7
2.2.5 Concept and risks of new cathodic protection system for tanks 8
3.0 Circuit model of current distribution for a single tank (CorrPro) 9
3.1 Assumptions 9
3.2 Current-distribution circuit model 9
3.3 Stray-current model for slab rebar 12
4.0 Model development: Finite element analysis model (COMSOL) 14
4.1 Assumptions 14
4.2 Governing equations 15
4.3 FEA model implementation of the governing equations 15
4.4 Assessment criteria for FEA output 16
4.5 Model geometry 17
4.6 Rebar modeling 18
4.6.1 Dome and walls rebar modeling approach 18
4.6.2 Slab rebar 18
4.7 FEA model mesh and solution settings 19
5.0 Results and Discussion 19
5.1 Baseline circuit model results 19
5.2 Estimate of AP Tank dome and wall rebar 19
5.3 Preliminary rebar test 20
5.4 Single-tank models 21
5.4.1 Single-tank mesh convergence 21
5.4.2 Preliminary no-rebar model and comparison to circuit model 21

5.4.3 Single-tank wall and dome rebar options 24
5.4.4 Comparison of FEA and circuit models with rebar 27
5.5 AN tank-farm model 28
5.5.1 AN Tank Farm mesh convergence 30
5.5.2 Existing pipe-protection CP system without tank-protection anodes 31
5.5.3 Current distribution for tank farm with tank-protection anodes 33
5.5.4 Potentials for tank farm (assessing overprotection and step/touch potentials) 36
6.0 Conclusions 40
7.0 Path forward and future model refinements needed 41
7.1 Rebar amount and distribution 41
7.2 Anode electrical output (existing pipe-protection system) 42
7.3 Deep anode locations 42
7.4 Soil and concrete resistivities and polarization resistance 42
7.5 Effective medium/porous electrode representation of pad 42
7.6 Circuit-model improvements 42
7.7 Experimental investigation of stray currents 43
8.0 References 44
Appendix A . Geometry values used in circuit models A-1

LIST OF TABLES

Table 1. Summary results from secondary liner floor UT inspection (conducted in annulus) [2]. 6

Table 2. Total rebar lengths and areas from AP Tank estimate used to develop FEA model..... 20

Table 3. Results of preliminary rebar comparison. 21

Table 4. Current distribution for single-tank, no-rebar FEA simulation for different currents..... 22

Table 5. Impact of polarization resistance on current distribution for single-tank, no-rebar FEA simulations. 22

Table 6. Current distribution of circuit model for single-tank with no rebar and different values for the number of divisions $\boldsymbol{n}$ of the wall area. 23

Table 7. Circuit and FEA model results for a single tank with rebar and tank walls disabled so that current only flows to the tank dome and bottom..... 24

Table 8. Preliminary surface vs. edge rebar tests for simplified single tank, corresponding to results in Figure 8..... 24

Table 9. Surface vs. edge rebar tests for single tank attempting to match actual rebar areas, corresponding to results in Figure 9 (W=Walls, D=Dome)..... 25

Table 10. Impact of polarization resistance on current distribution for single-tank FEA simulations with rebar using ComboEdge representation ($\boldsymbol{\rho s = 5000}$ Ω·cm, $\boldsymbol{\rho c = 1000}$ Ω·cm). 27

Table 11. Current distribution of circuit model with dome and wall rebar using default areas (Table A-1) and different values for the number of divisions $\boldsymbol{n}$ of the wall area..... 28

Table 12. Current distribution of circuit model with component areas manually set to match the FEA areas. 28

Table 13. Geometry summary for AN Tank Farm model..... 30

Table 14. Mesh convergence results for tank farm model ($\boldsymbol{\rho c = 1000}$ Ω·cm, $\boldsymbol{\rho s = 10000}$ Ω·cm, $\boldsymbol{Rp = 0.5}$ Ω·m$\mathbf{2}$). 31

Table 15. Current distribution for tank farm model with deep TP anodes disabled ($\boldsymbol{\rho c = 1000}$ Ω·cm, $\boldsymbol{\rho s = 10000}$ Ω·cm). 31

Table 16. Effect of polarization resistance on tank farm current distribution ($\boldsymbol{\rho c = 1000}$ Ω·cm, $\boldsymbol{\rho s = 10000}$ Ω·cm). 33

Table 17. Effect of soil resistivity on tank farm current distribution ($\boldsymbol{\rho c = 1000}$ Ω·cm, $\boldsymbol{Rp = 5}$ Ω·m$\mathbf{2}$). 35

Table 18. Effect of concrete resistivity on tank farm current distribution ($\boldsymbol{\rho s = 5000}$ Ω·cm, $\boldsymbol{Rp = 5}$ Ω·m$\mathbf{2}$). 36

Table 19. Effect of polarization resistance on tank farm potentials ($\boldsymbol{\rho c = 1000}$ Ω·cm, $\boldsymbol{\rho s = 10000}$ Ω·cm). 37

Table 20. Effect of soil resistivity on tank farm potentials ($\boldsymbol{\rho c = 1000}$ Ω·cm, $\boldsymbol{Rp = 5}$ Ω·m$\mathbf{2}$)..... 38

Table 21. Effect of concrete resistivity on tank farm potentials ($\boldsymbol{\rho s = 5000}$ Ω·cm, $\boldsymbol{Rp = 5}$ Ω·m$\mathbf{2}$)..... 38

Table A-1. Geometric characteristics used in CorrPro current-distribution circuit model (Sect. 3.2)..... A-1

Table A-2. Geometric characteristics used in CorrPro stray-current circuit model (Sect. 3.3)..... A-2

LIST OF FIGURES

Figure 1. (Top) overall configuration and (bottom) cross-section of a typical double-shell tank [2]..... 4

Figure 2. Drawings of slab cross section for (top) AP tanks [7] and (bottom) AN tanks [8]..... 7

Figure 3. Circuit model representation of the underground tank and CP system used to predict the current distribution..... 10

Figure 4. Drawing of AP tank slab cross-section [7] with the assumed stray-current pickup zone highlighted in green and the discharge zone in red..... 13

Figure 5. (Left) Schematic of computational domain and (right) predicted current density for replication of Peng et al. [14] stray-current model, predicting discharge (positive current) near cathode end of the rebar..... 18

Figure 6. Model setup for preliminary test of different rebar representations. The steel cathode surface is shown in blue at $\boldsymbol{y = 70}$ ft $\boldsymbol{= 21.3}$ m. The two layers of vertical rebar within the concrete layer are marked in black in front of the steel..... 20

Figure 7. Schematic of baseline single-tank, no-rebar FEA model geometry..... 22

Figure 8. Current distribution for the rebar representations listed in Table 8..... 25

Figure 9. Current distribution for different rebar representations approximating the actual rebar surface area corresponding to cases in Table 9. 26

Figure 10. Degrees of freedom and solution time for models in Table 9. 27

Figure 11. AN Tank Farm model geometry for (top) entire tank farm and (bottom) one tank with close-up of rebar. The dome rebar is simplified to only include radial rebar, and the wall rebar is simplified to only circumferential rings, both modeled as edges. 29

Figure 12. Current density to tank bottoms for tank farm with TP anodes disabled for (top) $\boldsymbol{Rp = 0.5}$ Ω·m2 and (bottom) $\boldsymbol{Rp = 5}$ Ω·m2, the same results as in Table 15..... 32

Figure 13. Effect of polarization resistance on tank farm current distribution ($\boldsymbol{\rho c = 1000}$ Ω·cm, $\boldsymbol{\rho s = 10000}$ Ω·cm). 33

Figure 14. Tank-bottom current density with 125 A current to TP anodes for (top) $\boldsymbol{Rp = 0.5}$ Ω·m$\mathbf{2}$ and (bottom) $\boldsymbol{Rp = 50}$ Ω·m$\mathbf{2}$ with the same color scale. 34

Figure 15. Effect of soil resistivity on tank farm current distribution ($\boldsymbol{\rho c = 1000}$ Ω·cm, $\boldsymbol{Rp = 5}$ Ω·m$\mathbf{2}$). 35

Figure 16. Effect of concrete resistivity on tank farm current distribution ($\boldsymbol{\rho s = 5000}$ Ω·cm, $\boldsymbol{Rp = 5}$ Ω·m$\mathbf{2}$). 36

Figure 17. Surface polarization $-\boldsymbol{\varphi surf}$ in overprotected regions ($< -\mathbf{1.1}$ V) of (a) the tank bottoms (same color scale as (b)), (b) the tank wall and wall rebar, and (c) the piping for $\boldsymbol{Rp = 50}$ Ω·m2, with (d) the full piping layout for comparison. 39

Figure 18. Surface polarization $-\boldsymbol{\varphi surf}$ in overprotected regions ($< -\mathbf{1.1}$ V) of the piping for (a) $\boldsymbol{Rp = 5}$ Ω·m2 and (b) $\boldsymbol{Rp = 10}$ Ω·m2 40

Figure 19. A initial proposed lab-scale experimental setup to test the effects of isolated rebar on impressed-current CP of steel plate and associated corrosion of the rebar [18]. 43

LIST OF ABBREVIATIONS

CP	Cathodic protection
CSE	Copper/copper-sulfate reference electrode
DST	Double-shell storage tank
FY	Fiscal year
PP	Pipe-protection (referring to existing CP system for tank-farm piping)
SRNL	Savannah River National Laboratory
SST	Single-shell storage tank
TP	Tank-protection (referring to proposed CP system for tank bottoms)
UT	Ultrasonic testing
WTP	Waste Treatment and Immobilization Plant
WTS	Waste transfer system

1.0 Introduction

Hanford stores over 52 million gallons of radioactive and chemically hazardous waste from the production of weapon materials in 177 underground carbon-steel storage tanks, split between 149 single shell tanks (SSTs) and 28 double shell tanks (DSTs) [1]. DSTs consist of a primary (inner) steel liner in direct contact with the tank contents, surrounded by a secondary (outer) steel liner that contains waste in the event of a leak in the primary tank. For structural stability, each tank rests on a reinforced concrete pad and is surrounded by a reinforced concrete shell/vault around the walls and dome. Six DST tank farms were constructed from 1968 to 1986 with a planned 40–50 year design life [2], so some are already operating beyond their initial life expectancy.

Ultrasonic testing (UT) has indicated significant thinning on the bottom of some of the secondary liners [2], which are in direct and intimate contact with the concrete pad. This is believed to be due to groundwater intrusion driving concrete-side corrosion. Since there is no direct access to the interface between the secondary liner and the concrete pad, it would be difficult to apply a chemical-based mitigation strategy to prevent this corrosion or to conduct repairs. However, cathodic protection (CP) is a potential method to inhibit further concrete-side corrosion without requiring access to this interface. Hanford already uses CP to protect other underground steel components within the tank farms.

CP must be properly designed accounting for the structures surrounding the DSTs, including steel reinforcing bars (rebar) within the concrete pad and vault, various process lines, and the existing CP system designed to protect the underground piping, but not the tanks. The system has been evaluated to understand constraints and opportunities for CP system installation, including assessment of concrete pad thickness, reinforcement layout, accessibility, and potential pathways for CP current distribution.

To support this effort, two finite element analysis (FEA) modeling subtasks have been completed, focusing on the Hanford AN tank farm as a representative example:

- Subtask 1: Development of an FEA model of a single tank with CP. This model enabled investigation of the influence of rebar in the concrete vault on the CP current distribution, comparison of the predicted current distribution to that of a simpler circuit model as a conceptual check, and testing of simplified model representations of the rebar geometry for use in larger-scale (full-tank-farm) models to make them computationally tractable.
- Subtask 2: Development of an FEA model of the entire AN tank farm consisting of seven tanks and associated piping, existing and new CP systems, and other components, incorporating insights from Subtask 1.

Simpler, equivalent circuit models were also developed to predict current distribution to different components of the system and to predict stray-current corrosion in the slab rebar, for comparison with the FEA results.

2.0 Background

2.1 Corrosion of steel in contact with soil/concrete and cathodic protection

For steel in contact with a corrosive electrolyte, localized cathodic and anodic sites will develop on the steel. At the anodic sites, iron will oxidize and dissolve, causing thinning and pitting. However, CP can be applied to reduce the corrosion rate and protect the steel by making it wholly cathodic using a direct current [1]. CP is one of the few methods of effective corrosion control for pre-existing buried or submerged metal structures [1]. It requires that the structure to be protected be electrically continuous and immersed in a sufficient volume of electrolyte to carry the current to the structure; the water in moist ground or concrete can serve as this electrolyte [1, 3]. An external anode is used to establish a circuit, with the steel to be protected serving as the cathode and the soil and concrete acting as an electrolytic medium.

Options for CP include impressed current and galvanic corrosion systems, where galvanic systems use a sacrificial anode that is naturally anodic relative to the protected structure. Impressed current systems drive an external current through anodes electrically connected to the structure being protected (forming a complete circuit) and use "non-consumable" electrodes that are naturally cathodic to steel (impressed-current anodes are still consumed, but at a relatively low rate) [1]. Impressed-current systems are used when currents larger than a sacrificial anode can supply are required, e.g., for the protection of large structures or areas with high electrolyte resistivity [1].

Design of an impressed-current CP system involves determining the amount of protective current required and the best means of applying it to the structure [1]. Soil resistivity is a very important characteristic [1]. The presence and location of other metallic structures in the vicinity may also affect the operation of the system, and multiple CP systems operating in the area can affect each other [1].

The structure-to-electrolyte potential is commonly used to assess adequacy of CP protection; the structure-to-electrolyte potential is the potential difference between the protected structure and a reference electrode (typically copper/copper sulfate for buried structures) in contact with the electrolyte [1]. Different Hanford reports cite different NACE criteria for evaluation of CP performance according to this potential, including NACE Standards RP169-96 ("Recommended Practice for Control of External Corrosion on Underground or Submerged Piping Systems") and RP0285-95 ("Recommended Practice for Corrosion Control of Underground Storage Tanks Systems by Cathodic Protection") [1] and NACE SP0285-2011 "External Corrosion Control of Underground Storage Tank Systems by cathodic protection" (paragraphs 5.2.1.1, 5.2.1.2, and 5.2.1.3) [4]. The summarized criteria from these standards include three potential criteria to use for steel structures [1, 4]:

1. A negative (cathodic) potential of at least 850 mV with CP applied, measured with respect to a saturated copper/copper sulfate reference electrode (CSE) contacting the electrolyte. Voltage drops other than those across the structure-to-electrolyte boundary must be considered for valid interpretation of the measurement.

2. A negative polarized potential (the sum of the structure's open-circuit corrosion potential and the cathodic polarization from CP current) of at least 850 mV relative to a CSE.

3. A minimum of 100 mV of cathodic polarization between the structure surface and a stable reference electrode contacting the electrolyte. The formation or decay of polarization can be measured to satisfy this criterion.

The Hanford evaluations focus on criteria 2 and 3. Meeting criterion 2 "generally implies complete protection from corrosion," while a structure satisfying criterion 3 is considered to be protected against corrosion by a factor of 10 [1]. The corrosion of the structure is expected to be reduced even if the structure is underprotected by CP, with increasing current offering increasing protection [1]. A complete interruption of the CP current will allow corrosion to return to its normal rate within a short period of time [1].

Literature data indicates that the current densities required for protection of structures in different environments cover a wide range. For example, typical/recommended CP current densities for uncoated steel provided in Table 2.5 of Ref. [3] and Table 4-2 of Ref. [5] indicate current densities as low as 0.4–1.5 mA/ft^2 (4.2–16.1 mA/m^2) can be protective in neutral soil, with well-aerated, wet, or acidic soils increasing the current requirements (reaching up to 15 mA/ft^2 for "highly acidic" soil). Soil with active sulphate-reducing bacteria requires particularly high current, with a stated current requirement of 42 mA/ft^2 [3]. Ranges of 0.5–1.5 mA/ft^2 are recommended for dry concrete [3], and moist/wet concrete increases the range to 3–15 mA/ft^2 [5] or 5–25 mA/ft^2 [3].

CP systems have the potential to accelerate corrosion of other structures in the vicinity of the protected structure, called "interference" [1]. CP interference is commonly detected through measurement of structure-to-electrolyte potentials and measurement of current flowing through a structure based on potential drop along it [1]. Test stations to measure current are typically installed on long, CP-protected

pipelines to detect changes in the current that could indicate interference or other problems with the CP protection [1]. The placement of the anodes, particularly use of remote anode beds rather than anodes close to the structure, can cause more interference problems [1].

Excessive CP current density/polarization potential, e.g., due to uneven current distribution over the structure, has the potential to cause hydrogen embrittlement or damage coatings [1]. These effects are associated with generation of hydrogen gas at the surface due to excessive CP potential [1]. Ref. [1] reported the threshold for hydrogen generation is approximately -1.1 V (instant off) potential relative to a CSE, while Ref. [4] uses the threshold of -1.2 V polarization vs. CSE. The target for CP satisfying criterion 2 without risking damage due to overprotection would therefore be a structure-to-CSE potential between -850 mV and the overprotection threshold of -1100 or -1200 mV.

For human safety, the electric potential distribution of the ground surface and exposed system components must avoid hazardous step and touch voltages, i.e., a person should not be able to bridge a hazardous voltage between their feet or between an object they are touching and the ground. This work uses the thresholds stated in NACE SP0177-2026 [6] that consider a 15-V step/touch voltage to be a shock hazard and the horizontal distance for a step or touch voltage to be approximately 1 m.

2.2 Hanford Waste Tanks

Hanford stores radioactive waste in underground storage tanks, some of which are double-shell tanks (DSTs) consisting of a primary (inner) steel liner in direct contact with the tank contents surrounded by a secondary (outer) steel liner encased by a reinforced concrete shell [2], as illustrated in Figure 1. They were designed so that leaks from the primary tank would be detectable and contained by the secondary liner to avoid release to the environment [2]. Six DST tank farms were constructed from 1968 to 1986 with a planned 40–50 year design life [2]. Tank farm AY was the first to go into service in 1971, and one tank, AY-102, has since leaked and been taken out of service [2]. The newest tank farms, AN and AP, went into service in 1981 and 1986, respectively, with 50-year design lives [2]. The DSTs are connected to ancillary equipment such as transfer piping, connectors, valves, and pumps used to control waste flow [2].

The primary tank has a 75 ft inner diameter, a height of 45 ft 9 in at the center, and rests on a refractory concrete slab between the primary and secondary liners (Figure 1, bottom), which provides thermal insulation of the primary tank from the secondary liner and foundation as well as air circulation/leak detection channels [2]. A 2.5-ft annular space exists between the cylindrical walls of the primary and secondary liner; this space allows for leak detection, for visual examination of walls of the primary and secondary liners adjacent to the annulus, and deployment of robots for UT and visual inspections [2]. There is only one steel dome, part of the primary tank, but the secondary tank's "upper knuckle" at the top of the wall overlaps and meets the primary tank knuckle with a small (up to 1 in) gap that is bridged by flashing strips tack-welded to the primary tank [2]. The top of the concrete dome is about 7–8 ft below the ground surface, and the edge of the dome is about 15 ft below the ground surface [2]. Both primary and secondary liners are made of carbon steel of the same specification [2].

For structural stability, each tank rests on a reinforced concrete pad and is surrounded by a reinforced concrete shell/vault around the walls and dome. The reinforced concrete pad/foundation is 89.5 ft in diameter for all active tank farms (other than AY) [2]. For non-AP tank farms, the pad tapers from 2 ft thick in the center (in a 3-ft diameter circle) to an approximately 1 ft minimum thickness, and tapers back to 2 ft at the outer edge, while the AP tank farm foundation has no taper and a uniform 2 ft thickness [2]. The pads also include drain slots to direct any leakage from the secondary tank into leak-detection wells [2]. The concrete slab includes two layers of rebar connected by a small amount of vertical rebar. This makes the full set of slab rebar electrically continuous, but it is electrically isolated from the tank.

The walls of the concrete shell are 1.5 ft thick, and the concrete dome is 1.25 ft thick [2]. The rebar in the dome and walls was installed around the metallic tank/dome before the concrete was poured, with the outside of the secondary liner serving as the inner concrete form.

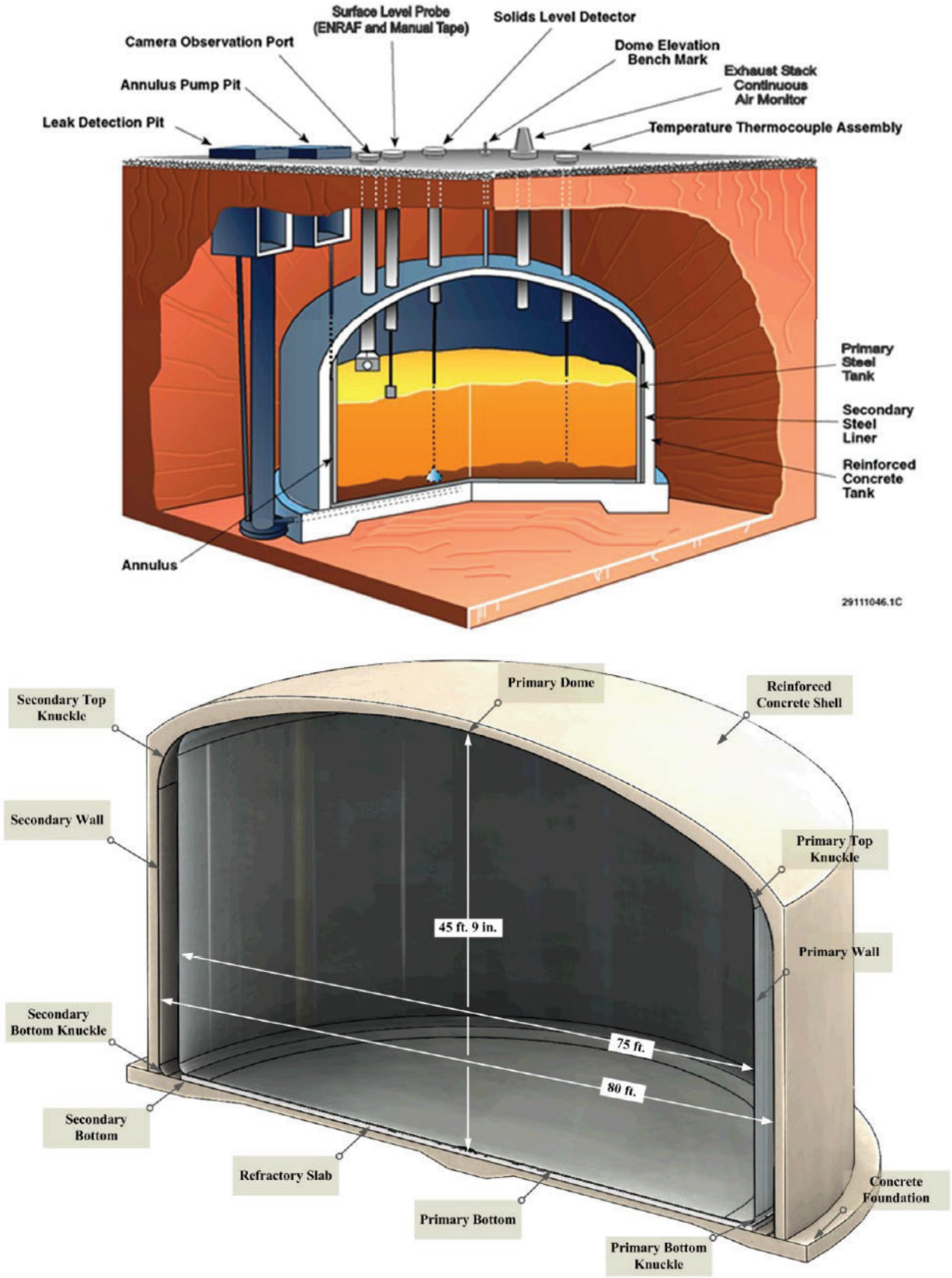

Figure 1. (Top) overall configuration and (bottom) cross-section of a typical double-shell tank [2].

Steel riser pipes providing access to the primary tank and annulus space for waste transfer, equipment installations, and monitoring/inspections penetrate through the concrete dome and steel liners [2]. These risers, and other components of the waste transfer system (WTS) such as valves and pumps are accessible through covered pits [2].

2.2.1 Waste transfer system

The DST WTS transports waste underground between tanks and process facilities and includes pump pits, valve pits, pumps, jumpers, valves, actuators, piping, and hose-in-hose transfer lines [2]. The WTS lines have secondary containment in the form of encasement piping in order to detect/collect leakage in the event of a failure in the primary lines, with carbon steel used for both primary piping and secondary encasement for most lines, switching to stainless-steel primary piping for lines constructed after 1990 [2]. WTS pipelines are buried at depths of nominally 2.5–4 ft with minimum depths as low as 1.65 ft [2]. All of the piping has some form of protective coating, and some newer pipelines have a coating considered to be waterproof (expected to eliminate the need for CP) [2].

2.2.2 Integrity assessments and evidence of corrosion

Periodic integrity assessments are required for existing tank systems storing mixed radioactive and hazardous waste. DST integrity assessments were completed in fiscal year (FY) 2006 and 2016, with a work plan for the next 2026 assessment developed in 2024 [2]. (Some of the actual inspection activities, such as visual examinations, were conducted on shorter intervals than the full integrity assessments.) Multiple possible modes of degradation for the steel and concrete structures are anticipated, with the primary types anticipated for the primary and secondary tanks and pipelines being wall thinning by general corrosion, pitting, stress corrosion cracking and fatigue-induced flaw growth, and liquid-air interface corrosion [2].

Inspections and testing to assess the integrity of the tanks and ancillary components have included [2]:

- Visual inspection of the primary and secondary liner walls via the annulus between them
- Visual inspection of the primary liner bottom via the refractory slab air slots
- UT examination of the primary and secondary liner walls and the secondary liner floor (in the annulus)
- UT examination of WTS primary and encasement piping at selected locations
- Visual inspection of the WTS piping annular space
- Leak testing of WTS pipes/encasements
- Inspection of the (existing) CP system to protect WTS encasements.
- DST concrete shell dome loading survey and settlement measurements
- Visual inspection of concrete pump and valve pit liner systems.

UT of the tanks is performed using remote robotic crawlers and provides a volumetric examination to detect thinning, pitting, and cracking of the steel [2]. The UT crawlers can inspect the vertical walls and the portion of the secondary liner floor within the annulus [2]. However, only portions of these surfaces are inspected, according to specified inspection criteria, and statistical analyses are used to assess the sampled results [2]. UT inspections have been carried out for the DSTs since 1997, with routine inspections of the annulus floors initiated in 2014 [2]. UT of the secondary liner bottom in the annulus has revealed considerable thinning in several tanks, with maximum thinning exceeding 20% for numerous tanks, and reaching >70% in AP-102 (Table 1) [2]. Because the inspected zones were limited to a small fraction of the total tank bottom area and only around the extreme edges, the degree of thinning in other locations could potentially be more severe than the measured values.

The corrosion is believed to be associated with groundwater from the surrounding soil seeping into the concrete vault and creating a corrosive environment [2]. Since the liner exteriors cannot be accessed for cleaning, repair, or replacement, an external system that does not require access to the concrete/steel interface is required to avoid further corrosion.

Table 1. Summary results from secondary liner floor UT inspection (conducted in annulus) [2].

Tank	Fiscal Year	Max Thinning (%)	UT Area (ft^2)
AN-107	1998	10	8
	2022	18.8	50
AP-106	2014	2.2	9.8
	2019	15.8	53
AP-102	2015	70.2	52
	2019	71.6	100
AN-103	2015	23.8	65
AN-104	2015	39.6	69
AW-103	2016	19.4	66
AN-105	2016	29.8	62
AN-106	2017	9.6	60
SY-101	2017	23.2	52
	2022	22.8	50
SY-102	2017	13.6	53
	2023	15	50
SY-103	2017	17.6	58
	2023	18.4	50
AZ-101	2018	11	26
AZ-102	2018	16.2	51
AP-107	2019	13	64
AP-108	2019	10.8	51
AN-102	2019	17.8	50
AW-102	2020	17.2	50
AW-101	2020	20.6	56
AW-106	2021	17	52
AW-105	2021	29	55
AW-104	2021	20.2	50
AP-103	2021	10	50
AY-101	2021	48.4	44
AN-101	2022	46.6	50
AP-105	2022	14	50
AP-101	2023	10.8	50

2.2.3 Different Hanford Tank Farms

Small adjustments and modifications were made as Hanford constructed different tank farms. The tanks in the AY, AZ, AP, and AN farms are similar, but not identical. There are differences in rebar sizes and placement between different tank farms, but the overall distribution is similar. Piping and existing CP systems also differ based on age and design function.

Originally, the modeling work was intended to focus on the AP Tank Farm, due to the highest (~70%) measured floor thinning being observed in an AP DST (AP-102), and some modeling work started based on the AP tank design. However, the AP Tank Farm is directly adjacent to the Hanford Waste Treatment

& Immobilization Plant (WTP), which contains large metallic structures. This proximity was anticipated to present electrical interference from components outside the tank farm, complicating the initial modeling and potentially making this tank farm non-representative of the performance of tank farms in other locations. As a result, the modeling effort was shifted to AN Tank Farm, which is more distant from the WTP.

The cross-sectional profile of the reinforced concrete pad differs between the AP and AN tank farms, as illustrated in Figure 2, but the material selection was identical for both tank farms.

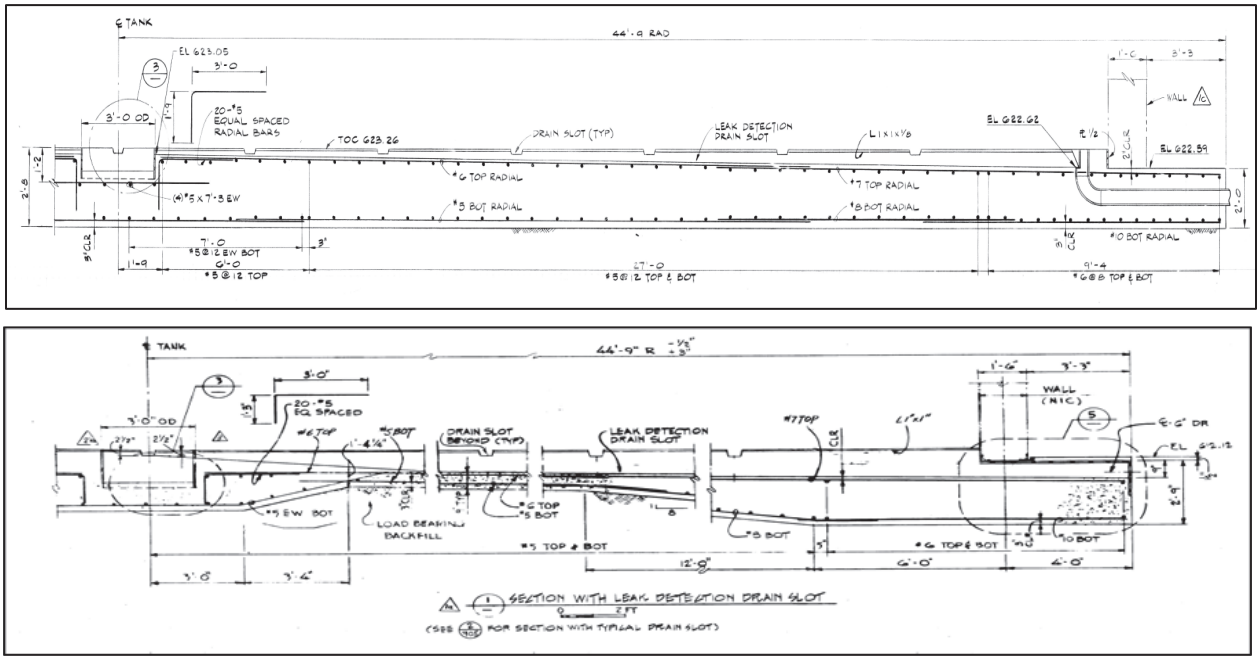

Figure 2. Drawings of slab cross section for (top) AP tanks [7] and (bottom) AN tanks [8].

2.2.4 Existing cathodic protection system for piping

Hanford currently has impressed-current CP systems used to protect buried pipelines but not designed to protect the tanks or full tank farms [9]. It aims primarily to protect the outer confinement pipes of the DST transfer lines; water lines, chemical addition lines, sewer lines, and most heating, ventilation and air conditioning ducts are excluded from CP coverage [4]. Transfer lines for single-shell tanks are all now out of service and therefore not part of the CP system monitoring program [4].

CP has been used on the underground waste lines since 1947; the original system successfully prevented waste-line leaks for over thirty years and was replaced by a newer CP system starting in 1980 (actual construction 1986-1996) [4, 9]. The existing CP system is beyond a normal 20–30-year design life given that it was built mostly in the 1984-1996 timeframe [4]. There have been upgrades to aboveground equipment since the construction of the newer CP system, but the system below ground remains unchanged since installation and in some cases has shown off-normal readings [4].

The original corrosion of stainless-steel pipes was attributed to sulfuric acid formed by bacteria [1, 9]. The newer CP system consisted of 35 rectifiers, 1418 anodes, and 529 test stations [9]. The 8-in-diameter anodes are prepackaged anodes made of silicon iron and coke breeze [9]. High-silicon cast iron forms a protective SiO_2 film that reduces anode consumption, and the film is stable "in many environments, with the exception of chloride rich environments" (a chromium-bearing alloy with similar silicon content has been developed to address this) [1]. Because these electrodes are naturally cathodic relative to steel, they would tend to drive accelerated corrosion if connected in the absence of the imposed current; the CP system uses diodes between the piping and CP anodes to prevent accelerated corrosion when the system is turned off [1]. Test

stations are located above protected piping, underground in manholes, and feature CSE connected to the underground piping to monitor the CP performance [1, 9].

Initially, tank ventilation lines were not cathodically protected because they were neither radioactive nor waste lines [9]. In 1981, one of the ventilation lines was discovered to have "corroded away" from extensive general corrosion due to reaction with the soil over less than 15 years service life; as a result, it was decided that all future underground ventilation lines should be cathodically protected [9].

Hanford selected a single CP acceptance criterion out of the multiple NACE criteria (Sect. 2.1) for their design purposes, namely a negative cathodic structure potential of –0.85 V relative to a CSE [1, 9]. The post-1980 CP system limits individual anode outputs to 0.03 A (30 mA) above the DSTs and 0.5 A (500 mA) away from the DSTs; anodes directly above tanks are installed horizontally, while those away from the tanks are vertical [1]. The soil resistivity was assumed to be of 40000 Ω·cm [1]. The anodes are closely coupled along the piping, with rectifiers outside the tank farms and independent of adjacent systems [1]. The system is designed to provide some flexibility of operation, and anodes can be disconnected from the circuit in order to improve current distribution, reduce overprotection, or eliminate stray currents [1].

Data for underground structure-to-electrolyte potential is collected annually at multiple CP test stations throughout the complex for comparison to NACE/AMPP International standards to check the system's effectiveness, and aboveground equipment (e.g., rectifiers) is monitored bimonthly [4]. The 2007 integrity assessment of the existing CP system [1] reported that only 33% of tested pipelines designed to be cathodically protected met NACE criterion 2 (Sect. 2.1) expected to provide complete protection. This was attributed to attempts to stay within the 30-mA/anode design limit intended to protect the tank rebar against stray-current corrosion. Approximately 90% of the pipelines met criterion 3, expected to provide partial protection (a factor of 10 reduction in corrosion rate). As of 2025, 305 of the test stations were considered actively monitored, with data from 165 of them being reported in the 2024 Annual Survey [4]. In 2024, ~67% of the tested CP system was found to meet NACE criteria 2 and/or 3 (Sect. 2.1) for adequate protection; 12% had inadequate polarization (not meeting either of the criteria); 19% were overprotected (i.e., more negative than -1.2 V relative to CSE), and ~2% of test stations "could not be located" [4].

2.2.5 Concept and risks of new cathodic protection system for tanks

The proposed new CP system analyzed in this study aims to deliver current predominantly to the tank bottom (i.e., bottom of the secondary liner) in order to protect against further corrosion. The anodes will be buried in the soil below the depth of the tank bottom (much deeper than the existing CP anodes intended to protect pipelines), and the current will pass through the reinforced-concrete slab to reach the metal.

Outside Hanford, CP systems are used to protect reinforcement steel inside concrete structures, but in this case, the CP current will have to travel through a reinforced concrete structure to protect the tank secondary liner. Interactions between the CP current and rebar are anticipated, but the impact of the rebar on the CP of the tank liner and the potential for detrimental impacts on the rebar itself are to be determined.

Both a single-tank model and a full AN tank farm model have been developed using FEA in COMSOL, as well as simplified equivalent circuit models to predict the current distribution and stray-current corrosion for a single tank, in order to better understand the expected behavior of a new CP system to protect the tanks. The models aim to predict whether the reinforced concrete will act as a barrier to protecting the liner, whether stray CP current will cause significant corrosion of the slab rebar, and how the new CP system will interact with other tank farm components and the existing CP systems. The simplified circuit model serves as a conceptual check for comparison to the FEA-predicted behavior.

This report refers to the existing Hanford CP system and its shallow anodes designed to protect the piping as the "pipe-protection" (PP) system/anodes and refers to the proposed new CP system with deep anodes to protect the tank bottoms as the "tank-protection" (TP) system/anodes.

3.0 Circuit model of current distribution for a single tank (CorrPro)

Simple electric-circuit models of the CP system were developed and implemented in the form of Microsoft Excel spreadsheets by a subcontractor (CorrPro) to predict current distribution and stray-current effects for comparison to the FEA models.

Because soil and concrete are both stagnant, low-conductivity media where factors such as the overpotential and ion kinetics are expected to be inconsequential, the system is modeled using a primary current distribution representation wherein the current distribution is controlled by only the resistivity of the medium and the surface areas of the components. Relevant surface areas for the tanks and rebar were estimated based on drawings for AP Tank Farm provided by Hanford [10].

3.1 Assumptions

- The current distribution is predicted based on resistivities in each zone and relative surface areas (primary current distribution) without accounting for the relative locations/proximity of structures. All resistances between structures and earth are calculated with formulas for structure to remote earth. Tank regions are treated as parallel resistors.
- The circuit model represents a single tank connected to a single rectifier and set of CP anodes. No tank farm piping is included.
- Dome and wall rebar is electrically connected ("shorted") to the tank. The spreadsheet calculates separate results for the slab rebar being electrically isolated from or connected to the tank.
- A ground grid of horizontal bare grounding cable is accounted for, with separate results for it being electrically isolated from or connected to the tank to a given cable size and spacing in the two horizontal directions. Resistance along the cable is neglected.
- Target CP current density to the tank bottom is 2 mA/ft^2 (10.05 A over entire tank bottom).
- If the slab rebar is electrically isolated from the tank, it may experience accelerated corrosion from stray CP current. The lower layer of rebar and all rebar beyond the tank radius are assumed to pick up current that is discharged by the upper layer of rebar directly under the tank.

3.2 Current-distribution circuit model

The circuit model represents the underground tank and CP anode as a network of resistors connected to a rectifier supplying direct current, as shown in Figure 3. The circuit consists of four series-connected sections:

- R1 represents the resistance of wires connecting the rectifier to the anode junction box.
- R2 represents the CP anodes as a set of parallel resistors, with the number and dimensions of the anode wells as model inputs. Figure 3 represents three CP anode wells as R2A, R2B, and R2C, but the spreadsheet model accommodates up to six.
- R3A through R3E represent the parallel resistances of sections of CP-protected metal to earth.
    - R3A is the ground grid resistance to earth based on the assumed layout. (Only included in the circuit if electrically connected to the tank.)
    - R3B, R3C, and R3D are the respective resistances of the tank dome, the cylindrical tank walls, and the tank bottom to earth. All of these resistances include the resistance of the soil, treated as a near-infinite domain, and the resistance of the concrete vault, treated as a coating on the steel. The resistances of the rebar around the dome and walls are included in parallel with the resistances of the dome and wall shell to calculate overall resistance.

  - R3E is the resistance of the bottom rebar in the concrete slab to earth. (Only included in the circuit if electrically connected to the tank.)

- R4 represents the resistance of the wires connecting the rectifier to the tank.

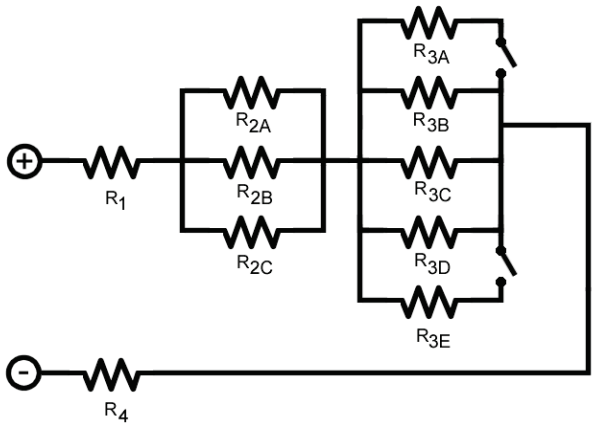

Figure 3. Circuit model representation of the underground tank and CP system used to predict the current distribution.

The model was implemented as a spreadsheet in Microsoft Excel with tank geometry details based on AP tank drawings. It is divided into nine worksheets, with eight sheets devoted to calculating the model resistances (R1, R2, R3A, R3B, R3C, R3D, R3E, and R4), and one summary sheet to consolidate the calculated resistances and calculate the resulting current distribution, i.e., the current to the tank shell bottom, walls, and dome; to the rebar in the bottom, walls, and dome, and to the ground grid. The summary sheet presents the current distribution for four different scenarios:

- Tank Shorted to Ground Grid and All Rebar
- Tank Isolated from Ground Grid and Foundation Rebar
- Tank Shorted to Ground Grid and Isolated from Foundation Rebar
- Tank Isolated from Ground Grid and Shorted to All Rebar

This report focuses on results for the second case corresponding to no connected ground grid and electrically isolated rebar in the bottom slab, since that is consistent with the assumptions used in the FEA model.

The calculation of R1 and R4 is straightforward. The wire length and its resistance per unit length are multiplied, and the product is divided by the number of parallel wires.

The anode resistance R2 assumes a set of vertical, cylindrical anodes of length L (cm) and diameter D (cm) in soil of resistivity ρ_s (Ω·cm) and calculates the resistance R_N (Ω) for the entire set of N anodes using the "Sunde equation," with the last term corresponding to a crowding factor for N anodes spaced with distance s (cm) [5]:

$$R_N = \frac{\rho_s}{2\pi NL}\left(\ln\left(\frac{8L}{D}\right) - 1 + \frac{2L}{s}\ln(0.656\,N)\right). \quad \textbf{1}$$

If $N = 1$, the spreadsheet sets the spacing s to a very large value (10^{100} cm) to yield the same result as the single-anode formula without the crowding factor. The resistance R_N is multiplied by N to calculate the equivalent resistance of an individual anode; the individual anode resistance is combined in series with the resistance of the wire leading to it (calculated by multiplying its length and unit resistance), and the individual anode-and-wire resistances are combined in parallel for the final resistance value.

The ground-grid resistance R3A considers a network of bare horizontal cable of diameter D (cm) using a formula for horizontal cable to earth resistance for cable buried at depth t (cm):

$$R = \frac{\rho_s}{2\pi L}\ln\left(\frac{L^2}{tD}\right). \quad \textbf{2}$$

Eq. 2 is calculated for $L = 3048$ cm (100 ft) to get a resistance per unit cable length (Ω/100 ft), which is then multiplied by a factor of 100 ft divided by the total cable length (effectively treating the ground cable as a set of 100-ft cable lengths in parallel). Finally, it was multiplied by an estimated crowding factor based on Eq. 1 as $NR_N/R_{N=1}$ where R_N is the result of Eq. 1 with N and s based on the assumed grid cable spacing, and $R_{N=1}$ is the single-rod version of Eq. 1 with the crowding factor equal to zero. For the calculations with the tank isolated from the ground grid, as is the focus in this report, resistance R3A is not included in the circuit.

Resistances R3B through R3D for the tank components rely heavily on two formulas: The soil resistance R_s (Ω) is calculated based on the resistance of a structure to a near-infinite domain of resistivity ρ_s (Ω·cm) using an effective diameter D_{eff} (cm) for a circle of the same surface area as the structure

$$R_s = \frac{\rho_s}{2D_{eff}} \quad \textbf{3}$$

and the concrete resistance R_c (Ω) is calculated as the resistance through a coating of thickness L (cm) and resistivity ρ_c over surface area A (cm^2)

$$R_c = \frac{L\rho_c}{A}. \quad \textbf{4}$$

Due to the L/A factor in Eq. 4 and the large area of the tank relative to the concrete thickness, R_c is generally expected to be a small contributor to the total resistance unless the concrete resistivity ρ_c is significantly higher than the soil resistivity ρ_s.

For the tank dome (resistance R3B), the surface area of the dome A_{dome} (cm^2) is estimated as half the surface area of an ellipsoid A_{ellip} (cm^2) using Knud Thomsen's equation

$$A_{dome} = \frac{1}{2}\,A_{ellip} \approx \frac{1}{2}\left[4\pi\left(\frac{(ab)^{1.6} + (ac)^{1.6} + (bc)^{1.6}}{3}\right)^{\frac{1}{1.6}}\right] \quad \textbf{5}$$

where a (cm) and b (cm) both equal the radius of the tank and c (cm) is the height from the top of the tank wall to the top of the dome. The length of rebar per ft^2 of dome surface area is calculated based on rebar spacing, and the surface area and volume of rebar around the dome is estimated from the length and a uniform rebar diameter. The effective resistivity of the concrete is reduced by the volume fraction of rebar in the concrete (this reduction is small). To calculate the resistance of the dome shell to earth, an equivalent diameter D_{eff} for a circle of area A_{dome} is calculated and used in Eq. 3 for the soil, and a concrete thickness L is used to calculate the resistance through the concrete using Eq. 4; these two resistances are combined in series. The resistance of the dome rebar is scaled from the dome shell values. The dome rebar resistance to soil equals the dome shell R_s scaled by the ratio of surface areas, $A_{dome}/A_{rebar,dome}$, and the rebar resistance through the concrete equals half the shell R_c since the rebar is inside the concrete; the two are combined in series. The total resistance associated with the dome is the resistance of the dome shell and the dome rebar in parallel.

The tank walls (resistance R3C) are a vertical cylindrical shell with height smaller than its diameter. As a result, the (single-rod) form of Eq. 1 applicable to long, narrow vertical cylinders ($L > D$) does not apply to the tank wall. Instead, the circuit model divides the surface area of the tank wall cylinder into n segments, calculates the equivalent diameter D_{eff} of a circle equal to the surface area of one segment, and calculates

the soil resistance of each segment using Eq. 3; the n segments are treated as parallel resistors, i.e., the calculated R_s for one segment is divided by n to get the total for the entire wall. The resistance R_c through the concrete is calculated using Eq. 4 with concrete resistivity reduced by the volume fraction of rebar. The resistance of the wall rebar is calculated from the wall shell resistance using the same methodology described previously for the dome.

The number of segments the tank wall is divided into is arbitrary, and the choice of n does affect the calculated resistance and resulting current density. It can be shown that dividing the area into n parallel segments with resistance given by Eq. 3 results in the total resistance being proportional to $n^{-1/2}$. Therefore, the calculated wall resistance decreases continuously with increasing n, approaching zero in the limit $n \to \infty$. The spreadsheet received from CorrPro fixed the number of divisions $n = 4$, but no physical basis for this choice was given. The current report includes results with different values of n to demonstrate its impact.

The tank bottom (resistance R3D) is the simplest of the tank components. Since the tank bottom is circular, its resistance to the soil is calculated using Eq. 3 using the actual tank diameter. The resistance through the concrete is calculated with Eq. 4 with concrete resistivity reduced by the volume fraction of rebar. The tank bottom rebar is handled separately as R3E to allow for it being electrically isolated from the tank shell.

The resistance R3E was calculated for the slab rebar based on the tank bottom resistances using the same methodology used for the dome and wall rebar. This resistance is only included in the circuit when the rebar is assumed to be electrically connected to the tank shell. Under the base assumption that the slab rebar is electrically isolated from the tank, R3E is omitted.

The summary sheet takes the resistances calculated in the individual sheets for all cathode components, i.e., the ground grid (if connected), tank components, and corresponding rebar, and uses them to calculate the percentage of the current going to each component. All of the cathode components are assumed to be in good electrical contact with each other with a common potential difference V (V) relative to earth, so the current fraction $I_{frac,i}$ of an individual component i can be readily calculated as $I_{frac,i} = \frac{I_i}{I_{tot}} = \left(\frac{V}{R_i}\right)\left(\frac{R_{tot}}{V}\right) = \frac{R_{tot}}{R_i}$ where I_i (A) and R_i (Ω) denote the current and resistance, respectively, of component i, and I_{tot} (A) and R_{tot} (Ω) are the total current and resistance of all of the cathode components in parallel.

The summary sheet takes a target average current density to the tank bottom as an input for each of the four cases. The target current density is multiplied by the tank bottom area to calculate the total current density I_{bottom} (A) to the tank bottom, and the current to all other cathode components is scaled from that value based on the current fractions, i.e., $I_i = I_{bottom}(I_{frac,i}/I_{frac,bottom})$. The summary sheet also calculates the total resistance of the circuit by summing the series-connected components (R1, R2, the combined R3, and R4) and calculates the required rectifier voltage to drive the total current.

The user inputs to the circuit model are resistivities, target current density, and various geometric parameters used to calculate surface areas and cable resistances. In contrast to the FEA model, the circuit does not account for polarization resistance Rp or the relative positions of different components.

The as-built circuit model spreadsheet always includes the dome and wall rebar in the calculation of current distribution for a tank, with no built-in mechanism to remove it from the circuit like the slab rebar. However, predictions for a tank with no rebar can be made by setting the rebar area to a very small value (e.g., by inputting an extremely small rebar diameter) resulting in a very high rebar resistance and thus no current to the rebar.

3.3 Stray-current model for slab rebar

The spreadsheet consists of two sheets, one for surface area calculations and one for stray-current calculations.

The surface-area sheet uses data from the slab Drawing H-2-90439 [7] to prepare detailed estimates of lengths, diameters, surface area, and volume of the rebar in the concrete slab below the tank bottom. There are two layers of rebar in the slab, with the upper and lower layers electrically connected to each other through a relatively small quantity of vertical bars near the center of the tank bottom. The concrete slab has a diameter of 89.5 ft, extending beyond the 80 ft diameter steel tank. Since CP current will flow upwards through the slab from the soil to the tank, the model assumes that the lower layer of rebar and the rebar beyond the 40-ft radius of the tank picks up stray current and the upper layer of rebar within the 40-ft tank radius discharges this current accompanied by accelerated corrosion. The assumed pick-up and discharge regions are marked in green and red, respectively, in Figure 4.

The spreadsheet itemizes various groups of rebar from the two rebar layers in the slab and their lengths, surface areas, and volumes in order to develop subtotals for the pick-up region (lower layer + upper layer outside tank radius) and discharge region (upper layer within tank radius).

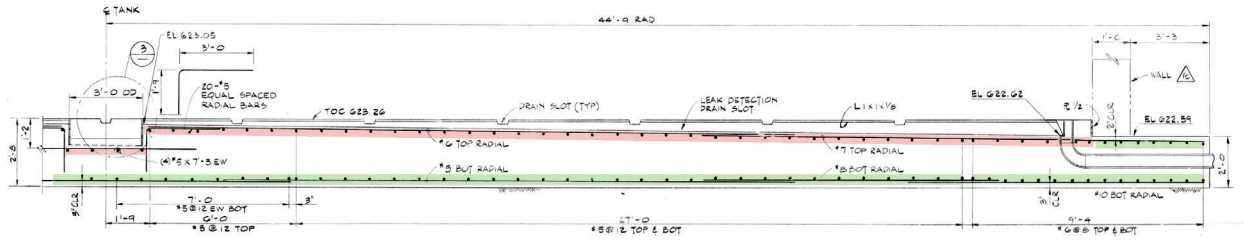

Figure 4. Drawing of AP tank slab cross-section [7] with the assumed stray-current pickup zone highlighted in green and the discharge zone in red.

The stray-current sheet estimates the fraction of current entering the slab rebar and the resulting corrosion rate using the rebar data from the surface-area sheet, soil and concrete resistivities, and the assumed thickness of the pick-up zone in the concrete. The lower portion of the concrete and the entire outer region beyond the radius of the tank is treated as part of the pick-up zone, while the discharge zone is the upper portion of concrete exclusively below the tank.

The volume fraction of rebar is higher in the pick-up zone than the discharge zone due to closer spacing of rebar in the bottom layer and greater use of larger-diameter rebar. These volume fractions are used to reduce the effective resistivity of the concrete in each zone.

The resistance through the discharge-zone concrete (the 40-ft-radius, 1-ft-thick circle of concrete below the tank) is calculated using Eq. 4 with L corresponding to the thickness of the disk and A to the area of the circle. The resistance through the pick-up zone concrete is treated as a parallel-resistance combination of the resistance of the lower 1-ft disk (calculated using Eq. 4 with L corresponding to the thickness and A to the area of the 89.5-ft circle of the slab) and the resistance of the inward path through the upper ring of concrete around the outer edge of the slab. The latter is calculated using Eq. 4 with $L = (89.5\ \text{ft} - 80\ \text{ft})/2$ representing the radial distance through the outer ring and $A = \text{average}(80\ \text{ft}, 89.5\ \text{ft})\pi(1\ \text{ft})$, i.e., the area of a cylinder midway through the ring of concrete. The total resistance through the concrete is the series combination of the pick-up and discharge resistances.

The resistance from the tank bottom to earth is calculated using Eq. 3 as in the current-distribution model; it is combined in series with the total concrete resistance to obtain the combined resistance from the tank bottom to earth.

The resistances from the pick-up and discharge rebar to the concrete are scaled from the tank-bottom-to-earth resistances based on the relative surface areas of the tank bottom and rebar and the resistivities of soil vs. concrete according to

$$R_{rebar-to-c} = R_{s,bottom}\frac{A_{bottom}}{A_{rebar}}\frac{\rho_c}{\rho_s}. \qquad 6$$

(This formulation for estimating resistance of a network of closely spaced cylinders scaled from a flat anode resistance is of unclear accuracy and may need improvement.) The total circuit resistance for the stray current to enter the rebar in the pick-up zone and leave it in the discharge zone is the series combination of the two rebar-to-concrete resistances for the pick-up and discharge zones. This value is used to predict the amount of stray current passing through the rebar.

The spreadsheet takes the target current density to the tank bottom as a user input. The tank-bottom current density and the tank-bottom area are used to calculate the total current through the slab, and the total current is multiplied by the total tank-bottom-to-earth resistance to calculate the tank-to-remote-earth IR drop (V).

The voltage drops across the pick-up and discharge zones of the concrete are calculated using the total current and the resistances for the pick-up and discharge zones of the concrete (Eq. 6); their sum, the voltage drop across the entire concrete slab, is divided by the total circuit resistance of pick-up and discharge from the rebar to predict the amount of stray current going through the rebar. Since the rebar spans only part of the concrete slab thickness, this approach is expected to overestimate the voltage drop and stray current experienced by the rebar. Dividing the total stray current by the surface area of rebar in the discharge zone provides the corrosion current density.

The corrosion current density is converted to a penetration rate (in mpy=mils/y) using the conversion factor 0.45 mpy = 1 $\mu A/cm^2$. The penetration rate corresponds to the rate of decrease in rebar radius.

The penetration rate is used to estimate the lifetime of rebar in the discharge zone for both the minimum rebar diameter and a calculated average diameter; the average diameter is calculated by dividing the total estimated surface area of the discharge-zone rebar by its total length to get an average circumference and dividing by π for the average diameter.

Acceptable metal loss is assumed to be up to 10% reduction in the cross-sectional area of the rebar, which corresponds to 5.13% loss in diameter or radius. The acceptable loss in radius is divided by the penetration rate to predict the lifetime of the rebar.

4.0 Model development: Finite element analysis model (COMSOL)

The objective of the modeling is to predict the current distribution of the CP system to different regions of the tanks and to guide the placement of the new CP anodes to protect the tank bottoms. To ensure adequate protection, all components of a tank farm must be considered, since the piping, existing PP CP systems, rebar, etc., will affect the distribution of current with the new, TP CP system.

COMSOL Version 6.3 was used for the FEA simulations in this work.

4.1 Assumptions

- The system can be modeled using primary current distribution, i.e., considering only the resistivity of the soil and concrete, with negligible polarization and other factors.
- The tanks and all associated piping in the system are in good electrical contact with each other and have practically uniform electric potential in the metal (much higher electrical conductivity in metal than in concrete/soil).
- The rebar in the reinforced concrete vault around the walls and dome is in good electrical contact with the metal of the corresponding portion of the secondary liner.
- The rebar in the pad below the tank is electrically isolated from the tank liner and all other metallic components. It exchanges current only with the surrounding concrete of the pad.
- Only the soil and concrete domains need to be simulated, with the metal domains (tanks, pipes, etc.) represented as boundary conditions at the interface of the metal with the soil and/or concrete.
- CP anodes can be simulated with an imposed current density boundary condition.

- The surroundings of the tanks/tank farms can be represented as large volume of soil that is electrically insulated far from the tanks.

4.2 Governing equations

In the underground soil and concrete domains, the electrolyte resistance is expected to dominate, so that the primary current distribution is sufficient for most cases [11]. The distribution of electric potential φ (V) in the soil/concrete domain is obtained by solving the Laplace equation

$$\nabla^2\varphi = 0. \quad (7)$$

The current distribution at the below- or at-grade protected metal structures such as storage tank surfaces and piping is estimated using the following equation:

$$i_m = \frac{V_m - \varphi_{surf} - E_{corr}}{Rp} \quad (8)$$

where i_m (A/m^2) is the CP current density at the metal interface with the concrete or soil, V_m (V) is the potential of the metal, φ_{surf} (V) is the concrete/soil potential at the interface with the metal, E_{corr} (V) is the corrosion potential of the metal, and Rp (Ω-m^2) is the polarization resistance of the metal in contact with the concrete/soil. The current density i_m is also related to the gradient of the concrete/soil electric potential at the interface with the metal by the relationship

$$i_m = -\frac{1}{\rho}\nabla\varphi \quad (9)$$

where ρ is the resistivity of the concrete or soil in contact with the interface [11].

The form of the interface current in Eq. 8 incorporates the corrosion kinetic effects by approximating the Butler-Volmer equation for low overpotentials. The full Butler-Volmer type kinetic equation is expected to be unnecessary due to the expected dominance of the electrolyte resistance on the current distribution [11].

Anodes for the CP systems are modeled with a prescribed current through their surfaces.

The three equations above plus the anode current output complete the mathematical description of the model for electric potential in the soil and concrete domains. The electric potential of the metal, V_m, is treated as a known input for calculation of the soil and concrete potential distribution.

4.3 FEA model implementation of the governing equations

In COMSOL, the Laplace equation (Eq. 7) is implemented using "Current Conservation" over all soil and concrete domains, using the electric conductivity conduction model. The electric conductivity $\sigma = 1/\rho$, where ρ is the electrical resistivity, differs for the soil and concrete domains but is uniform within each of the two media.

The soil domain around the tank or tank farm is defined as a cylindrical region in single-tank models and a rectangular region in tank-farm models; the top of the domain corresponds to ground level, and in all other directions, the soil extends beyond the modeled tank/tank farm components. On all sides except the ground surface, there is a 50-ft-thick region in the model geometry designated as an Infinite Element Domain. This feature applies a stretching/scaling functionality to effectively apply the outer boundary conditions at a large distance compared to the model geometry. On the outer edges of the domain (including the ground surface and the artificially distant in-soil boundaries), an Electric Insulation condition is applied to impose zero current density.

The boundary condition on the surfaces of all protected steel components, i.e., tanks and piping, is imposed using a normal current density defined as

$$i_m = (-\varphi - E_{corr})/Rp \quad \textbf{10}$$

At the steel interfaces where $\varphi = \varphi_{surf}$, this expression represents Eq. 8 with the metal potential $V_m = 0$ V as the implicit zero point of electric potential. Here, $E_{corr} = -0.5$ V.

The application of this boundary condition for each component depends on how that component is modeled in COMSOL. For the tanks, modeled as surfaces, the boundary condition is a straightforward Normal Current Density condition setting the inward normal current density $-\boldsymbol{n} \cdot (\sigma \boldsymbol{E}) = \boldsymbol{n} \cdot ((1/\rho)\nabla\varphi) = i_m$. Inward current density is positive when flowing into the computational domain, which is the concrete and soil, i.e., positive current density flows *outward* from the metal.

The piping systems are represented as line/edge elements instead of surfaces in the model, so the boundary condition is adjusted to current per unit length (A/m) by multiplying i_m by the pipe circumference, C_{pipe}. The boundary condition is applied as a Line Current Source equal to $i_m \cdot C_{pipe}$. The piping in the model was grouped by diameter; some groups corresponded to a small range of pipe diameters for simplicity and used the average of the circumferences for the upper and lower diameter bounds. Pipe penetrations are modeled so that they only contact the edges of the concrete vault instead of penetrating the concrete, in order to simplify the model geometry and avoid an excessive number of discrete geometry objects.

A variety of representations were tested for the rebar, as will be discussed later, including rebar modeled as line elements with simplified geometry (i.e., a simplified pattern of rebar designed to be computationally tractable while approximating the overall distribution of the actual rebar). The boundary condition for this rebar is handled as a Line Current Source similar to the piping, using an effective circumference chosen to make the surface area of the simplified rebar roughly match that of the real rebar for that region.

The TP anodes are modeled as cylindrical surfaces with either a Normal Current Density condition to impose a uniform surface current or (in the tank-farm model) a Terminal (Current) boundary condition to impose the total current over the surface. The (existing) PP anodes are modeled as edges with a Line Current Source, similar to the pipes; they are defined in groups with assigned currents based on the prescribed maximum currents for horizontal and vertical anodes in the Hanford CP system.

A Stationary study is used to solve for the steady-state solution. A uniform initial value for the electric potential, $\varphi = \varphi_{init}$, is applied throughout the computational domains (soil and concrete) to initialize the FEA calculations. This initial value is set to $\varphi_{init} = -E_{corr,m} = 0.5$ V, corresponding to zero current flow across the surfaces of the protected metal structures.

4.4 Assessment criteria for FEA output

The NACE criteria (Sect. 2.1) are used for field measurements to test installed systems and are limited by what physical performance metrics can be effectively measured in real systems. Field measurements cannot measure the localized variation of CP performance across the structure and instead give an averaged performance indication for portions of the structure relative to discrete reference electrode locations.

The COMSOL FEA output is not subject to the same limitations and offers a more comprehensive view of the predicted behavior of the system, including the ability to directly examine both local current density and local potential drop across the metal/concrete or metal/soil interface without having to correct for additional IR drop through soil/concrete.

The model calculates the electric potential in the concrete/soil domain relative to the steel at $V_m = 0$ V (Eq. 10). Principles to keep in mind when interpreting the FEA results with respect to measurements of actual installed CP systems include:

- The structure-to-electrolyte potential at a given location on the surface is equal to $V_m - \varphi_{surf} = -\varphi_{surf}$, i.e., a positive electric potential φ_{surf} predicted in the concrete/soil corresponds to a negative (cathodic) structure-to-electrolyte potential across the interface.
- Despite the simulation representing an active CP system, $-\varphi_{surf}$ is the equivalent of the instant-off potential, because it is the polarized potential across the interface without any IR drop through the soil. (In a real system, turning the CP current off is a workaround to compensate for being unable to measure the concrete/soil potential directly at the interface, but this is unnecessary in the simulated system).
- The corrosion potential E_{corr} is the depolarized potential reached by an unprotected system.

Since the FEA model can directly interrogate the local current density across the interface, this study focuses on the distribution of current density to assess the capability to supply a protective cathodic current, i.e., current from the electrolyte to the structure (negative boundary current in the FEA results) across the entire tank bottom. This is not a NACE-recognized criterion for monitoring CP systems due to the difficulty of identifying and empirically checking all anodic sites on a structure [3]. However, this criterion "[t]heoretically would provide complete protection" (Table 1.7 of [3]), and it is simple to check in the FEA model.

4.5 Model geometry

The model geometries, including steel tanks, concrete vault, rebar, pipelines, risers, existing CP anodes, etc. were based on drawings provided by Hanford [10, 12, 13].

Initial investigation of current flow focused on modeling a single tank before scaling up to a model of a full tank farm. The initial plan was to focus on AP tank farm due to its high measured floor-thickness losses, so the single-tank models were based on the geometry of an AP tank. The tank farm models are based on AN Tank Farm because it is further from the large metallic structures of WTP. The AP and AN tanks have similar geometries and rebar amounts, but there are some differences including different profiles of the bottom concrete slab. In the AP tanks, the slab is near-uniform with a slight taper along the radius, while the AN tank slabs have a more-varied slab thickness.

The single-tank model represents a single AP tank inside a cylindrical soil domain with a single TP anode. No pipelines, risers, or PP anodes were included in the single-tank model. The rebar was simplified in geometry for computational tractability as discussed further in Sect. 4.6, but the coverage and surface area of rebar over the areas of the tank and the total surface area of the rebar were based on estimates from the rebar drawings. The rebar in the slab below the tank was omitted from the model due to computational difficulties in simulating the electrically isolated rebar.

The tank farm model represents the layout of AN Tank Farm with seven tanks and associated piping, risers, and existing PP anodes. The piping penetrations through the tank domes were modeled based on Tank AN-101 (93 geometry objects in total) and copied to other tanks, mirrored in the east-west or north-south directions as needed to match the orientation of the connections in the drawings for each tank in AN Tank Farm. Piping interconnections between all tanks were added to the model, including water, drain, instrument air, steam, supernatant, slurry, intake, and exhaust lines. Five deep TP anodes that do not exist in the actual current tank farm were added in the model. As in the single-tank model, simplified rebar modeled as edges was included around the dome and walls of the tank, but the electrically isolated slab rebar was omitted from the model.

4.6 Rebar modeling

4.6.1 Dome and walls rebar modeling approach

Given the small scale of individual rebar compared to the tank structure, simulating the full rebar structure would be computationally costly. To reduce computational demands, alternative representations of the rebar were tested with the goal of identifying a more tractable model that maintains the same overall current distribution as the full model. This simplification is particularly important for the scaled-up model representing an entire tank farm with multiple tanks, piping, and numerous PP anodes.

The base representation is to model the rebar surface similarly to the tank shell. The rebar consists of hollow cylinders within the concrete domain, and the i_m boundary condition (Eq. 10) is applied at the interface. It is expected that simpler rebar geometries that retain the same effective surface area as the actual geometry will be able to predict the same current distribution. (This would be the case in the circuit model, but the FEA model will have additional geometry effects.)

In the "edge" representation, the rebar cylinders were replaced with edges (lines with no thickness) with the current density boundary condition applied as a Line Current Source equal to $i_m C_{rebar}$, where C_{rebar} is the circumference of the rebar. If the edge rebar follows the same path (and thus has the same length) as the actual rebar, C_{rebar} corresponds to the actual circumference of the rebar with no adjustment required. If the geometry of the edge rebar is further simplified, the effective circumference must be adjusted to match the surface area of the actual rebar.

In the "shell" representation, the rebar is replaced by a boundary following the shape of the outer surface of the concrete, and the current density is applied as a Boundary Current Source equal to $i_{rebar} = i_m f_{RB}$. To match the effective surface area, f_{RB} would equal the ratio of the actual rebar area to the shell area, i.e., $f_{RB} = A_{rebar}/A_{shell}$ (a smaller shell surface area than actual rebar surface area requires a larger effective current density).

4.6.2 Slab rebar

The slab rebar that is electrically disconnected from the tank could attract stray currents from the CP current passing through the slab that could lead to corrosion of the rebar. A simple, preliminary model was developed to try to replicate a stray-current model from Ref. [14] of an experimental setup of three pieces of rebar, with the surface polarization described by the Tafel equation. The model from Ref. [14] aimed to predict the spatial distribution of the stray-current corrosion to compare to the experimental test.

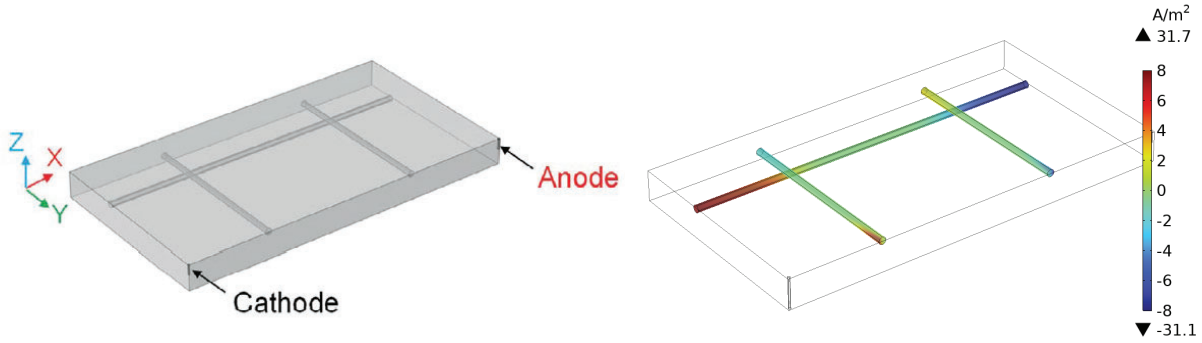

Figure 5. (Left) Schematic of computational domain and (right) predicted current density for replication of Peng et al. [14] stray-current model, predicting discharge (positive current) near cathode end of the rebar.

This modeling approach was ultimately not used in the models of the Hanford tanks/tank farms because attempts to simulate the isolated foundation rebar in the tank model led to the models crashing. No

successful solution for simulating the slab rebar in the tank models has been found to date. Instead, current models omit the rebar in the slab.

4.7 FEA model mesh and solution settings

Meshing for the FEA models was performed using COMSOL's predefined mesh size settings calibrated for general physics. These mesh settings provide sets of parameters governing the maximum and minimum element sizes, element-size growth rate, etc., at nine levels of refinement ranging from "Extremely Fine" to "Extremely Coarse."

In the single-tank model, the entire domain except for the Infinite Element Domain (around the perimeter of the cylindrical soil domain) was meshed with a free tetrahedral mesh using the same settings. The outer layer of Infinite Element Domains was meshed as five even layers of elements using a swept mesh.

For the tank-farm model, the "Pipe soil" (a layer of soil at the top of the domain containing the piping) and the concrete vaults were grouped and meshed with a finer mesh size setting than the remaining bulk of the soil domain. Both are meshed with a free tetrahedral mesh. The outer layer of Infinite Element Domains was meshed as five even layers of elements using a swept mesh.

All simulations were carried out with a user-selected tolerance of 0.00001.

5.0 Results and Discussion

5.1 Baseline circuit model results

A summary of the best-estimate geometric parameters based on AP tanks and used in the circuit models is provided in Table A-1 (current-distribution model) and Table A-2 (stray-current model) in Appendix A.

Using this geometry, soil resistivity $\rho_s = 5000\ \Omega\cdot\text{cm}$, and concrete resistivity $\rho_c = 1000\ \Omega\cdot\text{cm}$ with the default $n = 4$ for the tank-wall resistance calculation, the current-distribution model predicted that the majority of the rectifier current will go to the dome and walls of the tank (shell and rebar) for all cases, i.e., regardless of whether the ground grid R3A or slab rebar R3E are assumed to be electrically connected or electrically isolated. Only 7.7–9.5% of the current is expected to go to the tank bottom, with the higher end of that range (8.5-9.5%) corresponding to the slab rebar being electrically isolated (i.e., omitted from the model except as a volume-fraction reduction in the concrete resistivity).

To reach an average current density of 2 mA/ft^2 (total 10.05 A) on the tank bottom, the circuit model estimates a total rectifier current of 106 A would be needed in the case of the tank being isolated from both the ground grid and slab rebar. (The other cases would require larger total current.)

In this case, a total 10-A current would pass through the slab with the isolated bottom rebar, creating the potential for stray-current corrosion. The stray-current model predicts that only 2.1% of the total current through the slab would stray into the rebar, corresponding to ~0.21 A for a target tank-bottom current density of 2 mA/ft^2. This amount of stray current is predicted to drive a corrosion rate of 0.035 mpy, resulting in a lifetime of ~460 y for the minimum-diameter rebar and ~560 y for the average diameter. Note that the resistivities of the soil and concrete do not alter the calculated stray-current fraction, only the voltage drops, so the predicted corrosion rate and lifetime depend solely on the target current density to the tank bottom and the geometry.

5.2 Estimate of AP Tank dome and wall rebar

Table 2 shows the rebar lengths and areas from the estimate used to develop the FEA models and calculate effective diameters for the modeled rebar. Note that these rebar estimates differ from those in Table A-1 (Appendix A) for the circuit model. There were several attempts by different people to estimate the amount of rebar based on drawings and to divide it between dome and wall rebar. Different estimates reached somewhat different totals and differed substantially in the proportion of dome versus wall rebar. Differences

in the total length and surface area reflect error in the estimates of the actual total length and area, but the division between the dome and wall rebar is artificial, and the section of concrete around the corner where the wall and dome meet has a large amount of rebar that is ambiguous whether it should be considered as part of the wall or as part of the dome.

Table 2. Total rebar lengths and areas from AP Tank estimate used to develop FEA model.

Dome rebar length (ft)	51921
Dome rebar area (ft^2)	13094
Walls rebar length (ft)	65114
Walls rebar area (ft^2)	16513

5.3 Preliminary rebar test

Prior to testing on the single tank geometry, a simple, preliminary model of a flat square of reinforced concrete between a soil domain and a metal/concrete interface was set up as shown in Figure 6 to compare results for electrically connected rebar modeled as hollow cylinders, edges, or a shell. This model used a 50 ft x 50 ft square cross-section, with 70 ft length of soil and 2-ft thick concrete, and two layers of #9 rebar spaced at 12-in intervals. A 10-A current source was applied at the opposite end of the soil domain, assuming resistivities of $\rho_s = 20000\ \Omega{\cdot}\text{cm}$ and $\rho_c = 5000\ \Omega{\cdot}\text{cm}$, and polarization resistance $Rp = 0.5\ \Omega{\cdot}\text{m}^2$. The rebar array consisting of 98, 49-ft-long bars of #9 rebar had a total surface area of 1413.3 ft^2.

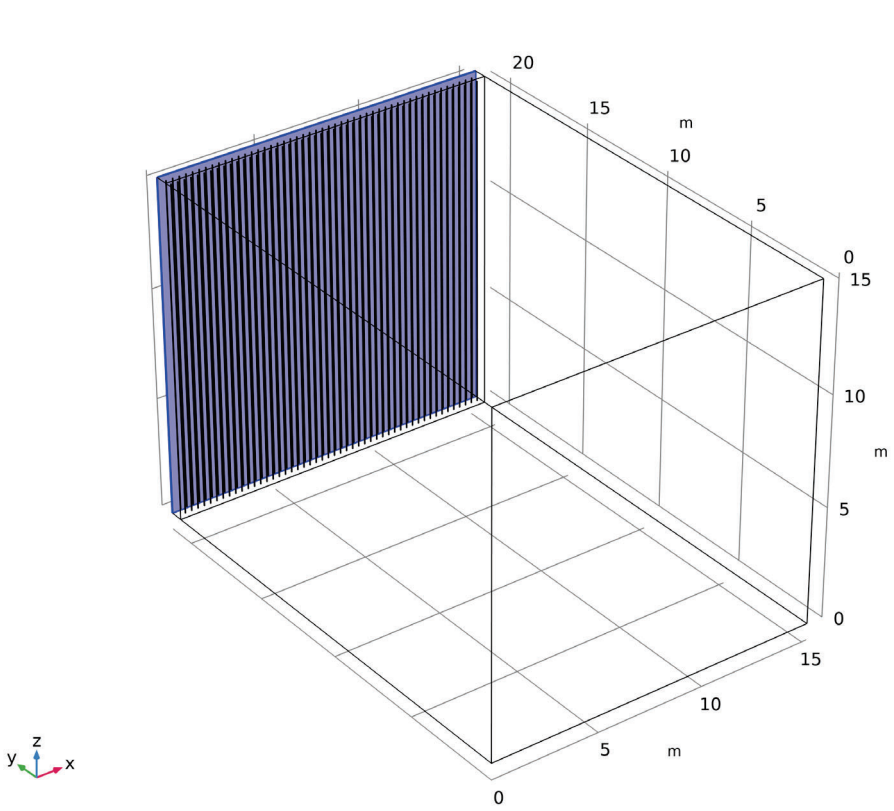

Figure 6. Model setup for preliminary test of different rebar representations. The steel cathode surface is shown in blue at $y = 70$ ft $= 21.3$ m. The two layers of vertical rebar within the concrete layer are marked in black in front of the steel.

The preliminary rebar test showed that the simplified rebar representations successfully reduced the computational load (Table 3). The degrees of freedom in the model were reduced by ~80% for the edge representation, ~70% for the 2-layer shell, and 97% for the 1-layer shell. The solution time was reduced by ~90% for the edge representation, ~80% for the 2-layer shell, and ~97% for the 1-layer shell.

Rebar modeled as edges has more "transparency" to the current, i.e, a larger fraction of the current reached the tank surface, than the model using hollow cylinders. Rebar modeled as shells resulted in a more uniform current distribution on the tank steel compared to the non-shell representations.

In the shell representation, the current distribution between the rebar and tank steel can be tuned with the f_{RB} parameter. The simulations indicated that the values of f_{RB} that closely matched the current distribution of the hollow-cylinder model did not necessarily correspond to matching the effective surface area. For a single shell layer with area 2401 ft^2 ($A_{rebar}/A_{shell} = 0.58$), $f_{RB} = 0.5$ matched the current density of the hollow-cylinder model closely, but for a model using two shell layers with area 4802 ft^2 ($A_{rebar}/A_{shell} = 0.29$), an approximate match to the hollow-cylinder current distribution was achieved with $f_{RB} = 0.125$.

Table 3. Results of preliminary rebar comparison.

	Hollow cylinder	Edge	2-layer shell	1-layer shell
Rebar area (ft^2)	1407.8	1414.3	4802	2401
Area adjustment	N/A	N/A	$f_{RB} = 0.125$	$f_{RB} = 0.5$
Rebar current (A)	-9.3025	-7.4220	-9.4087	-9.2769
Tank steel current (A)	-0.6973	-2.5779	-0.5913	-0.7231
Degrees of freedom	2633944	444816	752373	83619
Solution time (s)	29	3	6	1

5.4 Single-tank models

The surface areas of the dome, walls, and bottom of the steel tank in the model were 6370.6 ft^2, 8081.7 ft^2, and 5129.4 ft^2, respectively. A single cylindrical anode was modeled with a length of 20 ft and a radius of 5 ft, giving a surface area of 785.4 ft^2. The anode was placed at a depth of 140 ft below the ground surface and at a horizontal distance of 160 ft from the tank's centerline, in the x-direction (placing it 120 ft horizontally beyond the 40-ft-radius tank shell wall).

5.4.1 Single-tank mesh convergence

The current baseline single-tank mesh used for most of the current results uses the "Finer" mesh setting. Increasing the mesh refinement on level to "Extra Fine" increased the number of domain elements by ~2.6x. For a simulation with $\rho_c = 1000$ Ω·cm and $\rho_s = 5000$ Ω·cm, polarization resistance $Rp = 0.5$ Ω·m^2, and total current of 32 A to the single deep anode, the total currents to each component of the tank (dome, walls, bottom, and rebar) changed by ≤4.3%. The change to the bottom current was the lowest at only 0.5%. Since the current distribution and particularly the current to the tank bottom are the primary outputs of interest, the Finer mesh was considered adequately converged.

For the same simulation with higher polarization resistance of $Rp = 10$ Ω·m^2, the change from an "Extra Fine" mesh to "Finer" was even smaller, with the currents to the dome, walls, bottom, and rebar all changing by ≤0.2%.

5.4.2 Preliminary no-rebar model and comparison to circuit model

For initial comparison to the circuit model, a single tank (steel liner) and concrete shell with no rebar was simulated inside a soil domain with one anode below and to the side of the tank, as shown in Figure 7.

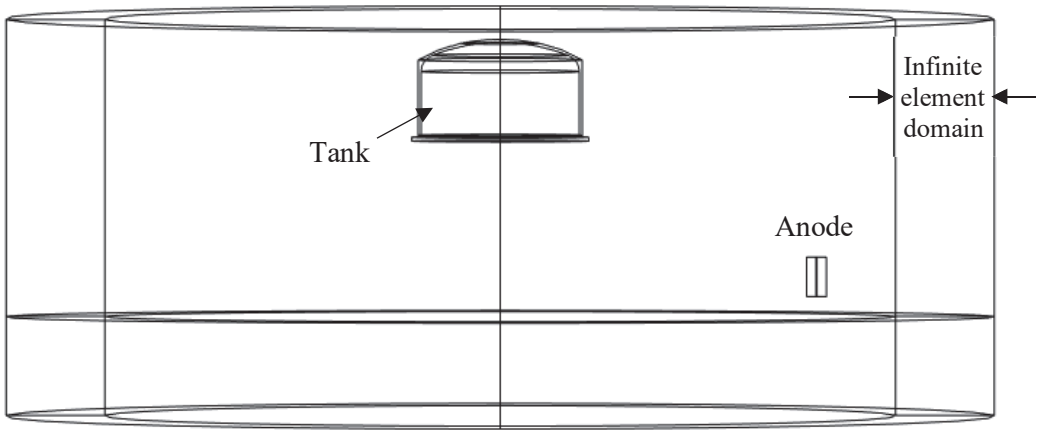

Figure 7. Schematic of baseline single-tank, no-rebar FEA model geometry.

Simulations using two different total currents at the anode, 50 A and 10 A, with $\rho_s = \rho_c = 1000\ \Omega \cdot \text{cm}$ and $Rp = 0.5\ \Omega{\cdot}\text{m}^2$ (Table 4) confirmed that the current distribution over different portions of the tank did not change with total current, as expected under the primary current distribution assumption.

Table 4. Current distribution for single-tank, no-rebar FEA simulation for different currents.

	Anode current: 10 A		**Anode current: 50 A**	
	Current (A)	**% of current**	**Current (A)**	**% of current**
Dome	-2.15	21.47%	-10.73	21.47%
Walls	-4.82	48.24%	-24.12	48.24%
Bottom	-3.03	30.29%	-15.15	30.29%
Total	-10.00	100.00%	-50.00	100.00%

Simulations using different values of the polarization resistance Rp with $\rho_s = \rho_c = 1000\ \Omega \cdot \text{cm}$ (Table 5) showed small changes in the current distribution. As Rp increased from 0.5 to 50 $\Omega{\cdot}\text{m}^2$, the dome current fraction increased monotonically from 21.5% to 25.0%, and the bottom current fraction decreased monotonically from 30.3% to 28.7%.

Table 5. Impact of polarization resistance on current distribution for single-tank, no-rebar FEA simulations.

	Rp=0.5 Ω·m²		**Rp=5 Ω·m²**		**Rp=10 Ω·m²**		**Rp=50 Ω·m²**	
	Current (A)	**% of current**	**Current (A)**	**% of current**	**Current (A)**	**% of current**	**Current (A)**	**% of current**
Dome	-2.15	21.47%	-2.17	21.74%	-2.22	22.15%	-2.50	24.99%
Walls	-4.82	48.24%	-4.86	48.55%	-4.84	48.41%	-4.63	46.33%
Bottom	-3.03	30.29%	-2.97	29.71%	-2.94	29.44%	-2.87	28.68%
Total	**-10.00**	**100.00%**	**-10.00**	**100.00%**	**-10.00**	**100.00%**	**-10.00**	**100.00%**

Table 6 shows the corresponding circuit model results for $\rho_s = \rho_c = 1000\ \Omega \cdot \text{cm}$ and no rebar (achieved via multiplying the rebar diameter by a factor of 10^{-100}). The circuit model does not include the polarization resistance Rp. Results are shown for several values of the geometry factor n governing how many pieces the tank wall is sectioned into for the calculation, ranging from the baseline $n = 4$ used by CorrPro down

to $n = 1$ corresponding to treating the entire cylindrical wall as if it were a single circle. Both the circuit and FEA models predict that the largest fraction of the current goes to the tank walls (roughly half, for all except the circuit model with $n = 1$). However, while the FEA model predicts more current to the tank bottom than the tank dome, the circuit model predicts the opposite: more current to the dome than the bottom.

The circuit model current distribution also varies with n. Since the calculated wall resistance is proportional to $n^{-1/2}$ (Sect. 3.2), the wall current fraction increases with increasing n while the dome and bottom current fractions decrease.

Table 6. Current distribution of circuit model for single-tank with no rebar and different values for the number of divisions n of the wall area.

	$n = 4$		$n = 3$		$n = 2$		$n = 1$	
	Current (A)	**% of current**	**Current (A)**	**% of current**	**Current (A)**	**% of current**	**Current (A)**	**% of current**
Dome	2.31	23.06%	2.48	24.83%	2.74	27.37%	3.17	31.71%
Walls	5.64	56.44%	5.31	53.10%	4.83	48.29%	4.01	40.10%
Bottom	2.05	20.50%	2.21	22.07%	2.43	24.33%	2.82	28.19%
Total	**-10.00**	**100.00%**	**-10.00**	**100.00%**	**-10.00**	**100.00%**	**-10.00**	**100.00%**

The approximate surface areas calculated for the circuit model (Table A-1) differed from the surface areas in the FEA model. To confirm that this difference is not the sole cause of the discrepancy, the areas of each tank section from the FEA model (dome 6370.6 ft^2, walls 8081.7 ft^2, and bottom 5129.4 ft^2) were directly input into the circuit model, replacing the calculated values. This shifts the results only slightly, resulting in a current distribution for $n = 4$ of 24.4% to the dome, 54.0% to the walls, and 21.6% to the tank bottom and still predicts more current to the dome than the bottom, opposite to the FEA prediction.

One hypothesized cause for the difference between dome and bottom current distribution is the relative positioning of the anode and the tank, which the 3D FEA model accounts for and the circuit model cannot. The depth of the anode could result in the closer tank region (the bottom) receiving more current. Table 7 shows the current distribution for both the circuit model and the FEA model with the current to the tank walls disabled to further simplify the geometry (in FEA, the tank wall current boundary condition is disabled; in the circuit model, an extremely low surface area is set for the walls) and also eliminate n as a factor. As above, the circuit model predicts more current to the dome (53%) than the bottom (47%). The FEA results include three different anode depths: 140 ft (baseline), 70 ft, and 35 ft (above the midline of the tank). Reducing the depth of the anode did shift the current density very slightly towards the dome, but the current to the bottom remained larger. In addition to the anode position, the tank itself was close to the surface of the soil (the top of the tank was 10 ft below ground level). A simulation adjusting the depths of both tank and anode to center them at a depth of 75 ft did result in a larger current distribution to the dome than the bottom, similar that predicted by the CorrPro circuit model, confirming that this ratio is affected by the relative positioning of the tank and anode to each other and to the ground surface, which the circuit model cannot replicate.

Table 7. Circuit and FEA model results for a single tank with rebar and tank walls disabled so that current only flows to the tank dome and bottom.

		FEA (Rp=0.5 Ω·m^2)			
		Tank top 10 ft deep			Tank and anode centered at 75 ft deep
	Circuit model	Anode depth 140 ft	Anode depth 70 ft	Anode depth 35 ft	
	% of current	% of current	% of current	% of current	% of current
Dome	52.94%	45.17%	46.22%	46.82%	54.52%
Bottom	47.06%	54.83%	53.78%	53.18%	45.48%
Total	**100.00%**	**100.00%**	**100.00%**	**100.00%**	**100.00%**

5.4.3 Single-tank wall and dome rebar options

The actual tank geometry includes two layers of rebar in a relatively thin concrete wall and includes both circumferential and vertical (in wall) or radial (in dome) rebar. Attempting to simulate the full rebar geometry posed difficulties in the FEA model, e.g., geometry failure errors occurred when trying to include circumferential rebar in the dome. As a result, in addition to testing use of edges instead of hollow cylinders, the geometry/path of the modeled rebar was also simplified, with modified diameters to match surface areas.

Initial tests compared rebar simulated as surfaces (hollow cylinders) vs. edges, each with several different simplified rebar distributions, as shown in Table 8 and Figure 8. The models used $\rho_s = 5000$ Ω·cm, $\rho_c = 1000$ Ω·cm, and $Rp = 0.5$ Ω·m^2. Of these seven cases, only the "Baseline" included rebar in the dome, while the others simulated only wall rebar. As a result, the Baseline case has much larger rebar surface area (~80% larger) than the other cases. The rebar surface areas of the non-Baseline cases varied by <3%. All of the rebar surface areas in this preliminary comparison are much smaller than the estimated actual rebar area totaling ~30k ft^2 (Table 2).

The non-Baseline current distributions are similar, suggesting only minor differences between horizontal vs. vertical rebar and edge vs. surface representations. However, the Baseline case had much larger differences from the other simulations; specifically, the current to the rebar increased, and the current to the dome decreased by a similar amount relative to the average of the other cases; this indicates that inclusion of the rebar in both walls and dome is important.

Table 8. Preliminary surface vs. edge rebar tests for simplified single tank, corresponding to results in Figure 8.

Name	Type	Rebar location	Description	Rebar surface area (ft^2)
Baseline	Edge	Walls & dome	Vertical and circumferential rebar in walls; radial rebar in dome.	10655
528 Surf	Hollow cyl.	Walls only	528 vertical #9 rebar	5989.7
39 Surf	Hollow cyl.	Walls only	39 horizontal #18 rebar	5849.5
78 Surf	Hollow cyl.	Walls only	78 horizontal #9 rebar	5849.3
528 Edge	Edge	Walls only	528 vertical #9 rebar	6016.2
39 Edge	Edge	Walls only	39 horizontal #18 rebar	5882.0
78 Edge	Edge	Walls only	78 horizontal #9 rebar	5882.0

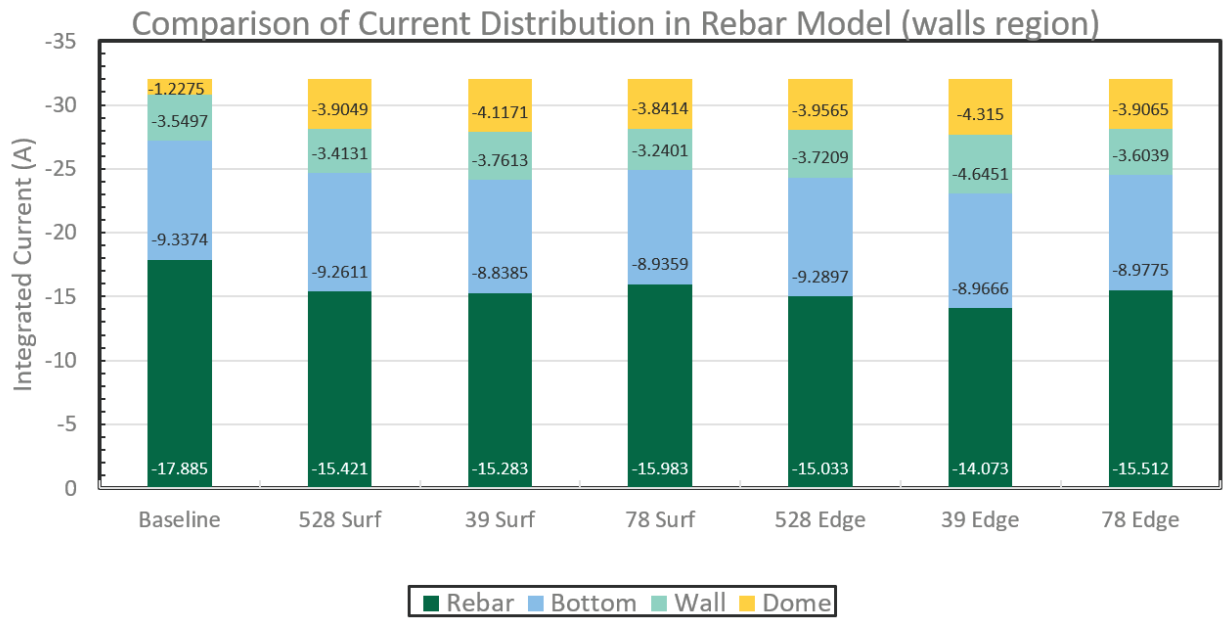

Figure 8. Current distribution for the rebar representations listed in Table 8.

Subsequent simulations, shown in Table 9 and Figure 9, targeted a total rebar surface area of 30000 ft^2 to approximate the rebar area of ~13k ft^2 in dome and ~17k ft^2 in walls (Table 2). The parameters in Table 9 includes four different approaches to matching the actual rebar area, each tested with a pair of one hollow-cylinder and one edge representation. The first pair used radial/vertical rebar of uniform diameter through both dome and wall, matching the total rebar area. The second pair approximated the wall rebar surface area with horizontal wall rebar and no dome rebar. The third pair approximated the total surface area with horizontal wall rebar (larger diameter) and no dome rebar, and the final pair used radial dome rebar and horizontal wall rebar with different diameters to individually match the dome and wall rebar surface areas.

Table 9. Surface vs. edge rebar tests for single tank attempting to match actual rebar areas, corresponding to results in Figure 9 (W=Walls, D=Dome).

Name	Type	Rebar location	Description	Rebar diameter (in)	Dome rebar surf. area (ft^2)	Wall rebar surf. area (ft^2)
Baseline528	Hollow cyl.	W & D	528 rad/vert	3.7	30272	
BaselineAll	Edge	W & D	528 rad/vert	3.6	30142	
Wallhoriz17	Hollow cyl.	W only	78 horiz	3.3		17158
Edgehoriz17	Edge	W only	78 horiz	3.3		17254
Wallhoriz30	Hollow cyl.	W only	78 horiz	5.75		29898
Edgehoriz30	Edge	W only	78 horiz	5.75		30063
ComboSurf	Hollow cyl.	D & W	528 rad. (D); 78 horiz. (W)	4.5 (D) 3.4 (W)	13508	17225
ComboEdge	Edge	D & W	528 rad. (D); 78 horiz. (W)	4.1 (D) 3.3 (W)	13024	17034

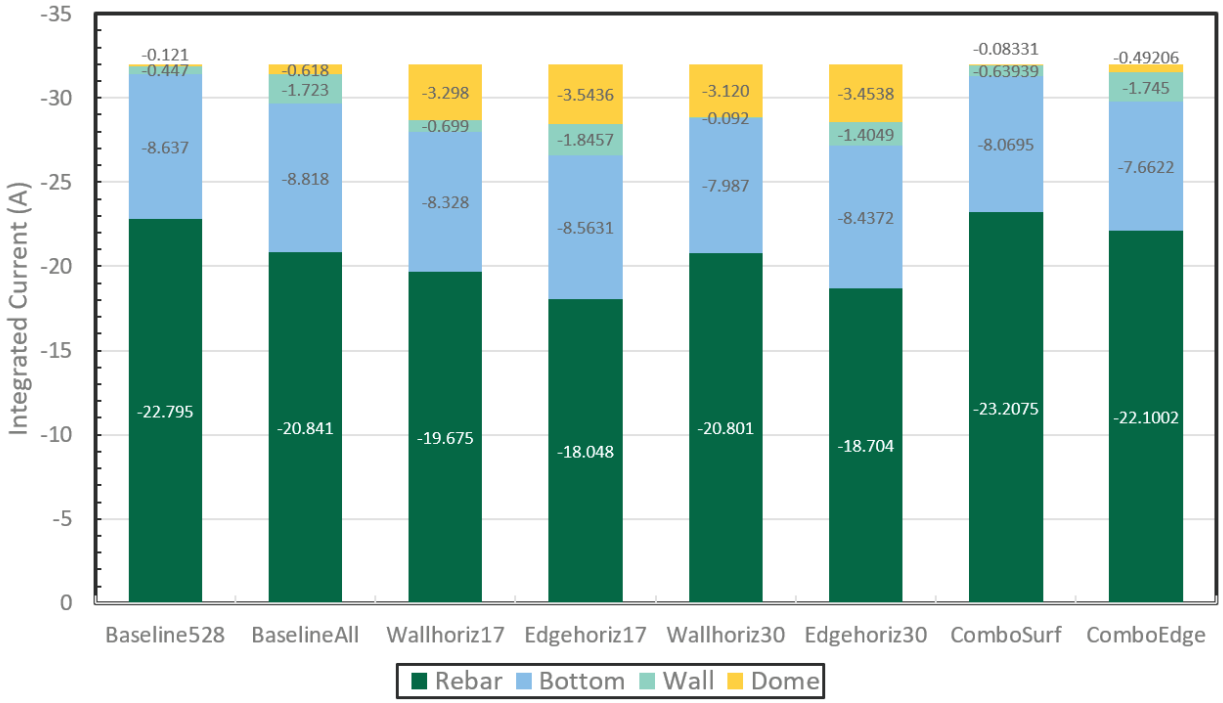

Figure 9. Current distribution for different rebar representations approximating the actual rebar surface area corresponding to cases in Table 9.

For each pair of surface vs. edge simulations, the edge representation resulted in lower current to the rebar and higher current to the walls. The use of vertical vs. horizontal rebar in the walls ("Baseline__" vs. "Combo__" models) had little impact on the current distribution. However, omission of the dome rebar resulted in much higher current to the dome and correspondingly lower rebar current, even if the wall rebar area was increased to the full ~30k ft^2. This shows that it is important to include rebar in the correct areas around the tank, not just match the total rebar area. The current to the tank bottom, the primary focus of this study, remained fairly consistent across all of the rebar representations.

Figure 10 shows the number of degrees of freedom and solution time for the models above. For each pair, using the edge representation instead of the surface (hollow cylinder) representation substantially reduces the complexity and solution time of the model. As a result, the edge representation will be used to cut down on the computational load of the model. Using separate diameters to match the dome and wall rebar (ComboEdge) is slightly more computationally complex than using uniform radial/vertical rebar for both (BaselineAll); however, this slightly more complex representation is selected in the interest of separating out the current going to dome vs wall rebar.

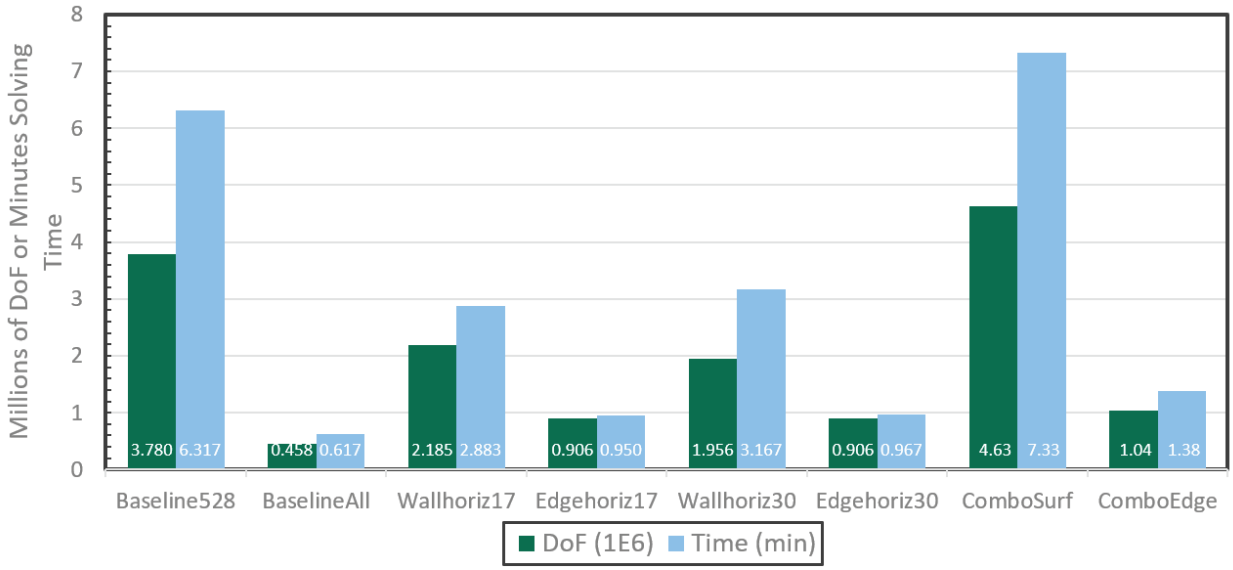

Figure 10. Degrees of freedom and solution time for models in Table 9.

5.4.4 Comparison of FEA and circuit models with rebar

Table 10 shows the current distribution for a single tank using the ComboEdge model to represent the dome and wall rebar for $\rho_s = 5000$ Ω·cm, $\rho_c = 1000$ Ω·cm, and values of Rp from 0.5 to 50 Ω·m^2. For all values of polarization resistance, the largest fraction of the current goes to the wall rebar; the smallest fraction goes to the dome shell, and the tank bottom receives ~23–25% of the current. Overall, increasing Rp results in more current going to the dome and walls and less to the rebar.

Table 10. Impact of polarization resistance on current distribution for single-tank FEA simulations with rebar using ComboEdge representation ($\rho_s = 5000$ Ω·cm, $\rho_c = 1000$ Ω·cm).

	Rp=0.5 Ω·m^2		Rp=5 Ω·m^2		Rp=10 Ω·m^2		Rp=50 Ω·m^2	
	Current (A)	% of current	Current (A)	% of current	Current (A)	% of current	Current (A)	% of current
Dome	-0.49	1.54%	-1.3364	4.18%	-1.5764	4.93%	-1.9129	5.98%
Walls	-1.75	5.45%	-4.0542	12.67%	-4.6819	14.63%	-5.6246	17.58%
Bottom	-7.66	23.94%	-8.0647	25.20%	-8.0513	25.16%	-7.4942	23.42%
Dome rebar	-4.43	13.85%	-3.91	12.23%	-3.7888	11.84%	-3.8341	11.98%
Wall rebar	-17.67	55.21%	-14.63	45.72%	-13.902	43.44%	-13.134	41.04%
Total	**-32.00**	**100.00%**	**-32.00**	**100.00%**	**-32.00**	**100.00%**	**-32.00**	**100.00%**

Table 11 and Table 12 show the current distribution predicted by the circuit model with n ranging from 4 to 1 using the calculated areas (Table 11) and with areas overridden to match the FEA model (Table 12). Adjusting the areas to match the FEA model improves the prediction of the distribution between dome and wall rebar in particular, since the circuit model and FEA model had very different estimates of dome vs. wall rebar. However, neither successfully captures the behavior of the FEA model. E.g., the circuit model predicts a much lower fraction of current to the tank bottom and higher fractions reaching the dome and dome rebar compared to the FEA model. Given the previous results for the simpler models without rebar, this discrepancy is probably attributable to the relative positioning of tank components that the circuit model is incapable of capturing.

Table 11. Current distribution of circuit model with dome and wall rebar using default areas (Table A-1) and different values for the number of divisions n of the wall area.

	$n = 4$		$n = 3$		$n = 2$		$n = 1$	
	Current (A)	**% of current**	**Current (A)**	**% of current**	**Current (A)**	**% of current**	**Current (A)**	**% of current**
Dome	3.39	10.59%	3.64	11.38%	3.99	12.47%	4.56	14.25%
Walls	8.38	26.19%	7.81	24.41%	7.00	21.88%	5.67	17.72%
Bottom	3.03	9.47%	3.25	10.16%	3.56	11.13%	4.07	12.72%
Dome rebar	9.09	28.41%	9.76	30.50%	10.69	33.41%	12.22	38.20%
Wall rebar	8.11	25.34%	7.54	23.56%	6.76	21.13%	5.47	17.10%
Total	**-32.00**	**100.00%**	**-32.00**	**100.00%**	**-32.00**	**100.00%**	**-32.00**	**100.00%**

Table 12. Current distribution of circuit model with component areas manually set to match the FEA areas.

	$n = 4$		$n = 3$		$n = 2$		$n = 1$	
	Current (A)	**% of current**	**Current (A)**	**% of current**	**Current (A)**	**% of current**	**Current (A)**	**% of current**
Dome	2.91	9.09%	3.18	9.94%	3.58	11.18%	4.27	13.34%
Walls	6.58	20.56%	6.24	19.51%	5.74	17.93%	4.85	15.16%
Bottom	2.60	8.13%	2.84	8.88%	3.19	9.97%	3.81	11.91%
Dome rebar	6.04	18.88%	6.59	20.60%	7.41	23.15%	8.84	27.63%
Wall rebar	13.87	43.34%	13.14	41.08%	12.09	37.77%	10.23	31.97%
Total	**-32.00**	**100.00%**	**-32.00**	**100.00%**	**-32.00**	**100.00%**	**-32.00**	**100.00%**

5.5 AN tank-farm model

The AN tank farm model includes seven tanks and their associated piping, the PP anodes of the existing CP system, and five deep anodes representing a TP CP system that does not yet exist in the actual tank farm. The model geometry is shown in Figure 11. A summary of geometric parameters for the model, including the total and per-tank surface areas of the tank domes, walls, bottoms, and rebar in the tank farm model is provided in Table 13. The five deep anodes are modeled as cylindrical with 20 ft length and 5-ft radius, giving each a surface area of 785.4 ft^2, and they were placed at a depth of 140 ft below the ground surface.

The dome and wall rebar is modeled as edges with simplified geometry. The dome is modeled with only radial rebar, and the walls are modeled only with circumferential rebar. The dome and wall rebar are each assigned an effective diameter to match the estimated surface area of the actual rebar $A_{rb,act}$ from Table 2 with the length of the modeled rebar ($L_{rb,mod}$, Table 13) using the formula $A_{rb,act}/(\pi L_{rb,mod})$.

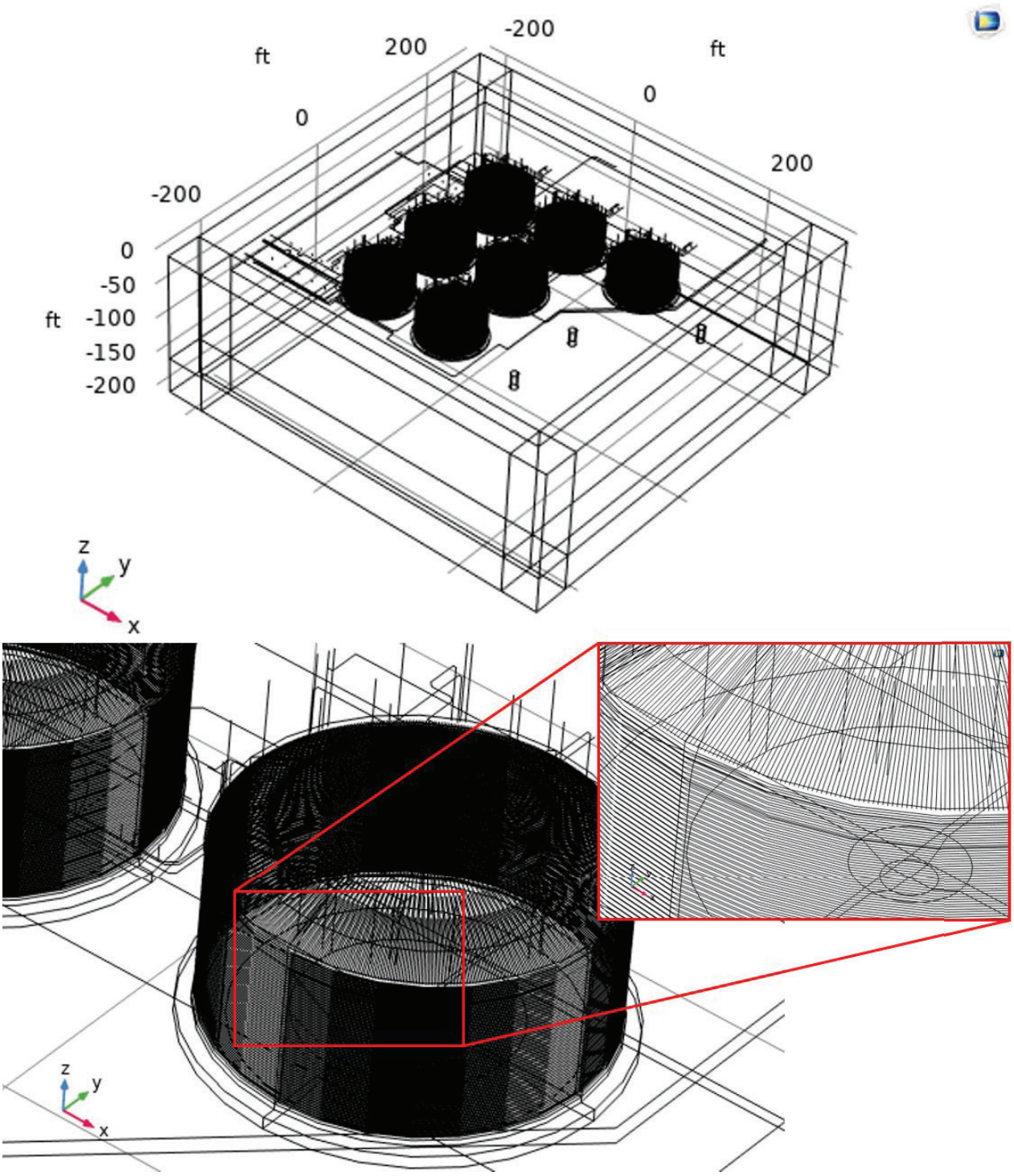

Figure 11. AN Tank Farm model geometry for (top) entire tank farm and (bottom) one tank with close-up of rebar. The dome rebar is simplified to only include radial rebar, and the wall rebar is simplified to only circumferential rings, both modeled as edges.

Table 13. Geometry summary for AN Tank Farm model.

	Total	Per tank
# Tanks	7	
# Deep anodes	5	
Dome area (ft^2)	44594	6371
Walls area (ft^2)	55405	7915
Bottom area (ft^2)	35905	5129
Dome rebar length (ft)	82603	11800
Dome rebar effective diameter (in)	4.24	
Dome rebar area (ft^2)	91693	13099
Walls rebar length (ft)	200740	28714
Walls rebar effective diameter (in)	2.2	
Walls rebar area (ft^2)	115612	16516
Pipes length (ft)	20962	
Deep anode area (ft^2)	3927	
Existing CP anode area (ft^2)	871.27	

5.5.1 AN Tank Farm mesh convergence

The current baseline tank farm mesh used for most of the current results uses "Extra Fine" mesh in the Pipe Soil and concrete vaults with "Fine" mesh in the bulk soil. Table 14 shows the results of the baseline tank farm mesh compared to one coarser and one finer mesh. Each mesh refinement more than doubled the number of domain elements. For these simulations, the resistivity values were $\rho_c = 1000\ \Omega{\cdot}\mathrm{cm}$ and $\rho_s = 10000\ \Omega{\cdot}\mathrm{cm}$; the polarization resistance of the metal structures was $Rp = 0.5\ \Omega{\cdot}\mathrm{m}^2$, and total current to the five deep anodes was 125 A (25 A per anode) and 9.71 A total to the shallow CP anodes. The total current to the tank bottom changed by only 0.55% in the baseline mesh compared to the coarser mesh and by 0.28% upon further refinement to the finer mesh. Changes to the total currents to the tank dome rebar, tank wall rebar, and piping were <3% for both mesh refinements. The largest percent changes were to the current to the wall and dome shells, but these corresponded to absolute changes of <0.5 A over all tanks due to the relatively low total current. Because the current to the tank bottoms, not the dome and wall shells, is the primary output of interest in these simulations, the baseline mesh was considered to be sufficiently converged.

As observed for the single-tank model, the change due to mesh refinement was smaller at higher values of the polarization resistance. For $Rp = 5\ \Omega{\cdot}\mathrm{m}^2$, the percent change in current for the baseline mesh compared to the coarser mesh was ≤4.4% for all of the components listed in Table 14, and the change in the bottom current was only 0.43%. Increasing it to $Rp = 10\ \Omega{\cdot}\mathrm{m}^2$ and $Rp = 50\ \Omega{\cdot}\mathrm{m}^2$ decreased the maximum percent change in current to 2.5% and 1.1%, respectively.

Table 14. Mesh convergence results for tank farm model ($\rho_c = 1000$ Ω·cm, $\rho_s = 10000$ Ω·cm, $Rp = 0.5$ Ω·m^2).

	Coarser mesh	Baseline mesh		Finer mesh	
Pipe soil & concrete mesh setting	Finer	Extra Fine		Custom*	
Bulk soil mesh setting	Normal	Fine		Finer	
	Result	**Result**	**% change from coarser mesh**	**Result**	**% change from baseline mesh**
Domain elements	1929592	5484871	184.25%	12101964	120.64%
Dome current (A)	-0.33	-0.38	16.70%	-0.42	10.67%
Walls current (A)	-3.43	-3.89	13.39%	-4.31	10.72%
Bottom current (A)	-52.63	-52.92	0.55%	-53.07	0.28%
Dome rebar current (A)	-2.79	-2.87	2.69%	-2.88	0.58%
Walls rebar current (A)	-36.15	-35.75	-1.09%	-34.95	-2.24%
Pipes current (A)	-39.38	-38.90	-1.23%	-39.08	0.46%

*The custom mesh setting for the finer mesh was based on the Extremely Fine setting, with the maximum and minimum element sizes increased to 15.15 ft and 0.47 ft, respectively, corresponding to the average of the values for the Extremely Fine and Finer default mesh settings.

5.5.2 Existing pipe-protection CP system without tank-protection anodes

Because the tanks (and wall/dome rebar) are assumed to be electrically connected to the piping systems, they are connected to the existing PP CP system. As a result, disabling the current boundary condition on the deep TP anodes in the simulation so current is provided only by the existing PP anodes should provide an approximation of the current and potential distributions within the system as it exists today.

Table 15 shows the current distribution and anode voltage results for the tank farm without TP current for two different polarization resistances, and Figure 12 shows the corresponding distribution of current density to the tank bottoms. The majority of the current goes to the pipes, as expected since the PP anodes were installed specifically to protect the piping, and the predicted current densities on the tank bottoms are very small.

Table 15. Current distribution for tank farm model with deep TP anodes disabled ($\rho_c = 1000$ Ω·cm, $\rho_s = 10000$ Ω·cm).

	Rp=0.5 Ω·m^2	Rp=5 Ω·m^2
Dome current (A)	-0.070	-0.22
Walls current (A)	-0.047	-0.17
Bottom current (A)	-0.16	-0.17
Dome rebar current (A)	-0.56	-0.59
Walls rebar current (A)	-0.77	-0.73
Pipes current (A)	-8.11	-7.83
Avg. bottom curr. density (mA/ft^2)	-0.0044	-0.0047
Max. potential on PP anodes (V)	12.27	12.50
Min. potential on PP anodes (V)	0.77	0.86

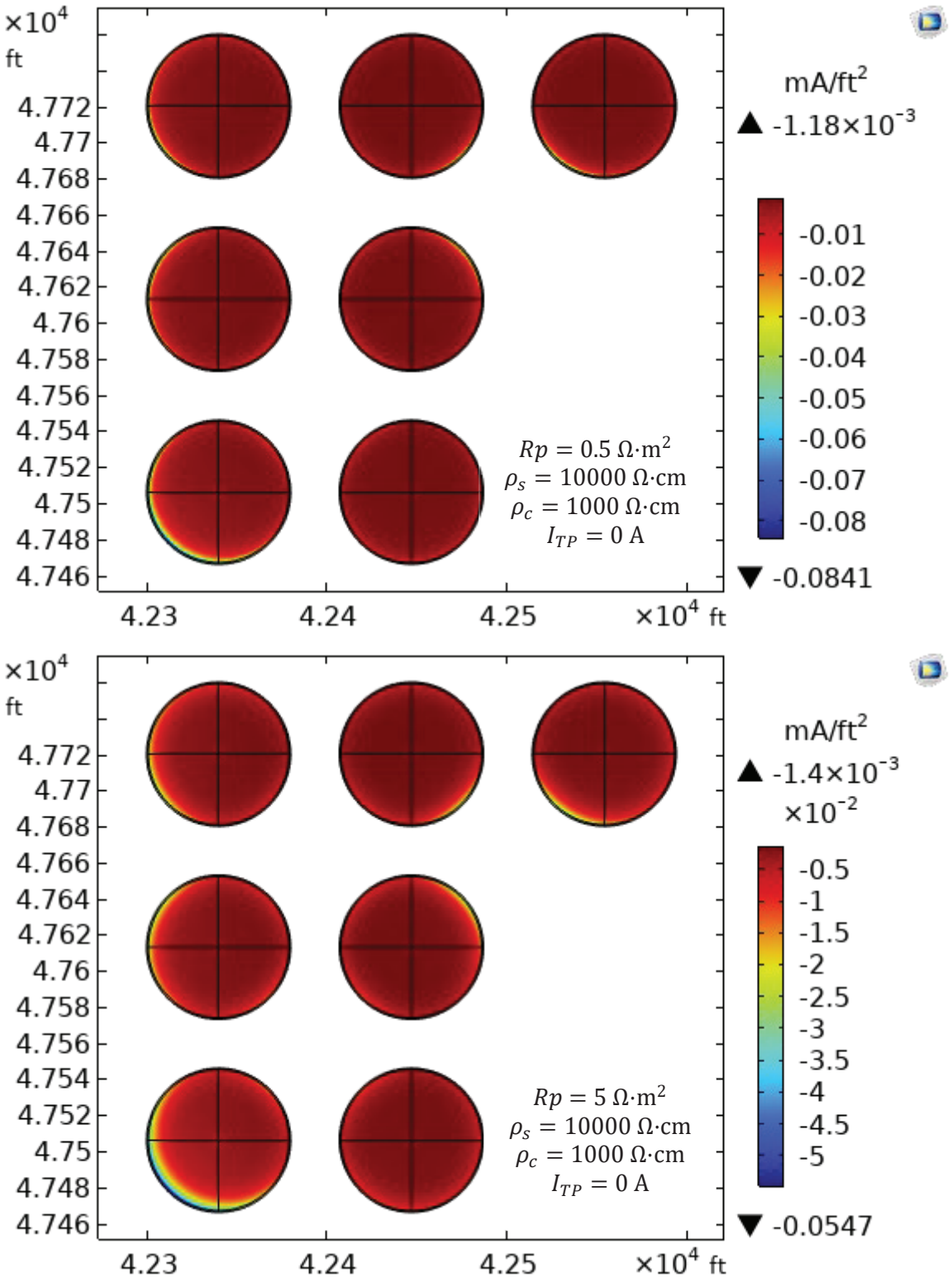

Figure 12. Current density to tank bottoms for tank farm with TP anodes disabled for (top) $Rp = 0.5\ \Omega{\cdot}m^2$ and (bottom) $Rp = 5\ \Omega{\cdot}m^2$, the same results as in Table 15.

With the current model setup/parameters and assumed PP anode currents, these simulations predict some local non-cathodic (non-negative) current density on small portions of the piping (<0.5% of the 20962 ft

total): for $Rp = 0.5\ \Omega{\cdot}m^2$, ~91 ft with average current $< 4 \times 10^{-4}$ mA/ft (maximum 2.9 mA/ft) and, for $Rp = 5\ \Omega{\cdot}m^2$, ~1.3 ft with average current $< 10^{-6}$ mA/ft (maximum 0.08 mA/ft). Plotting the sections with predicted non-negative current shows that these correspond to very short sections of pipe scattered across the tank farm.

5.5.3 Current distribution for tank farm with tank-protection anodes

Table 16 and Figure 13 show the currents to various components of the tank farm with all CP anodes active, for different values of the polarization resistance Rp ranging from 0.5 to 50 $\Omega{\cdot}m^2$. (This is a broader range than the 5–30 $\Omega{\cdot}m^2$ range expected for an uncoated structure [11].) In this simulation, the resistivities were $\rho_c = 1000\ \Omega{\cdot}cm$ and $\rho_s = 10000\ \Omega{\cdot}cm$, and the total current was 125 A to the five deep TP anodes (25 A per anode) and 9.71 A total to the shallow PP anodes. The component currents in Table 16 sum to the total anode current of 134.7 from both sets of anodes. As Rp increases, the current to the tank bottoms and pipes decreases (becomes less negative), while more current reaches the tank walls and, to a lesser extent, the dome.

Table 16. Effect of polarization resistance on tank farm current distribution ($\rho_c = 1000\ \Omega{\cdot}cm$, $\rho_s = 10000\ \Omega{\cdot}cm$).

	Rp=0.5 Ω·m²	Rp=5 Ω·m²	Rp=10 Ω·m²	Rp=50 Ω·m²
Dome current (A)	-0.38	-1.36	-1.75	-2.85
Walls current (A)	-3.89	-10.74	-12.86	-17.25
Bottom current (A)	-52.92	-50.56	-49.12	-44.38
Dome rebar current (A)	-2.87	-2.95	-3.19	-4.86
Walls rebar current (A)	-35.75	-31.71	-31.68	-35.46
Pipes current	-38.90	-37.38	-36.12	-29.92
Avg. bottom curr. dens. (mA/ft²)	-1.47	-1.41	-1.37	-1.24

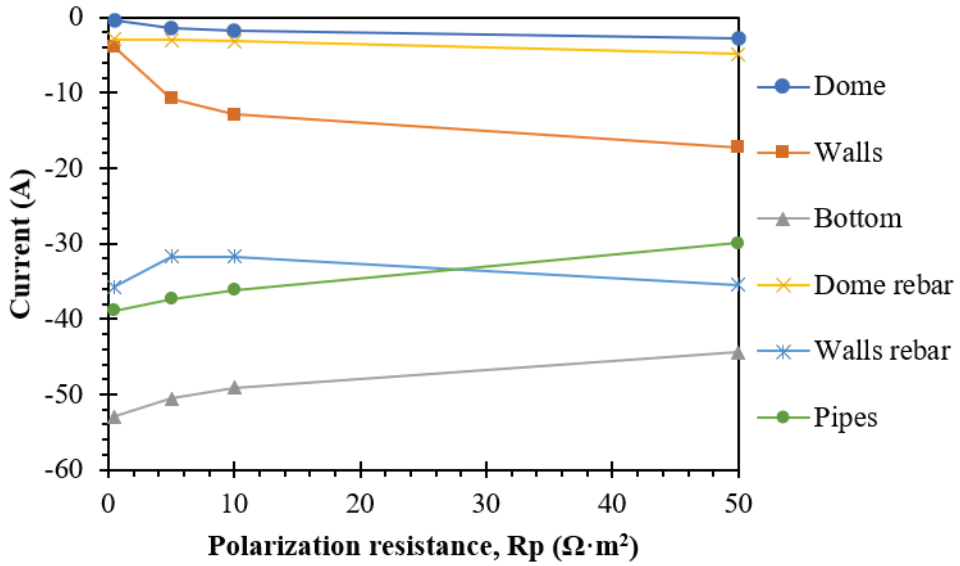

Figure 13. Effect of polarization resistance on tank farm current distribution ($\rho_c = 1000\ \Omega{\cdot}cm$, $\rho_s = 10000\ \Omega{\cdot}cm$).

Figure 14 shows the corresponding distribution of current density to the tank bottoms for $Rp = 0.5\ \Omega{\cdot}m^2$ and $Rp = 50\ \Omega{\cdot}m^2$, with the color scale set to the same range for both plots. The current density for $Rp = 50\ \Omega{\cdot}m^2$ is more uniform than for $0.5\ \Omega{\cdot}m^2$ with a much smaller range of current density in addition to the

lower overall current to the tank bottoms. The largest current densities occur around the perimeters of the tanks on sides furthest from other tanks.

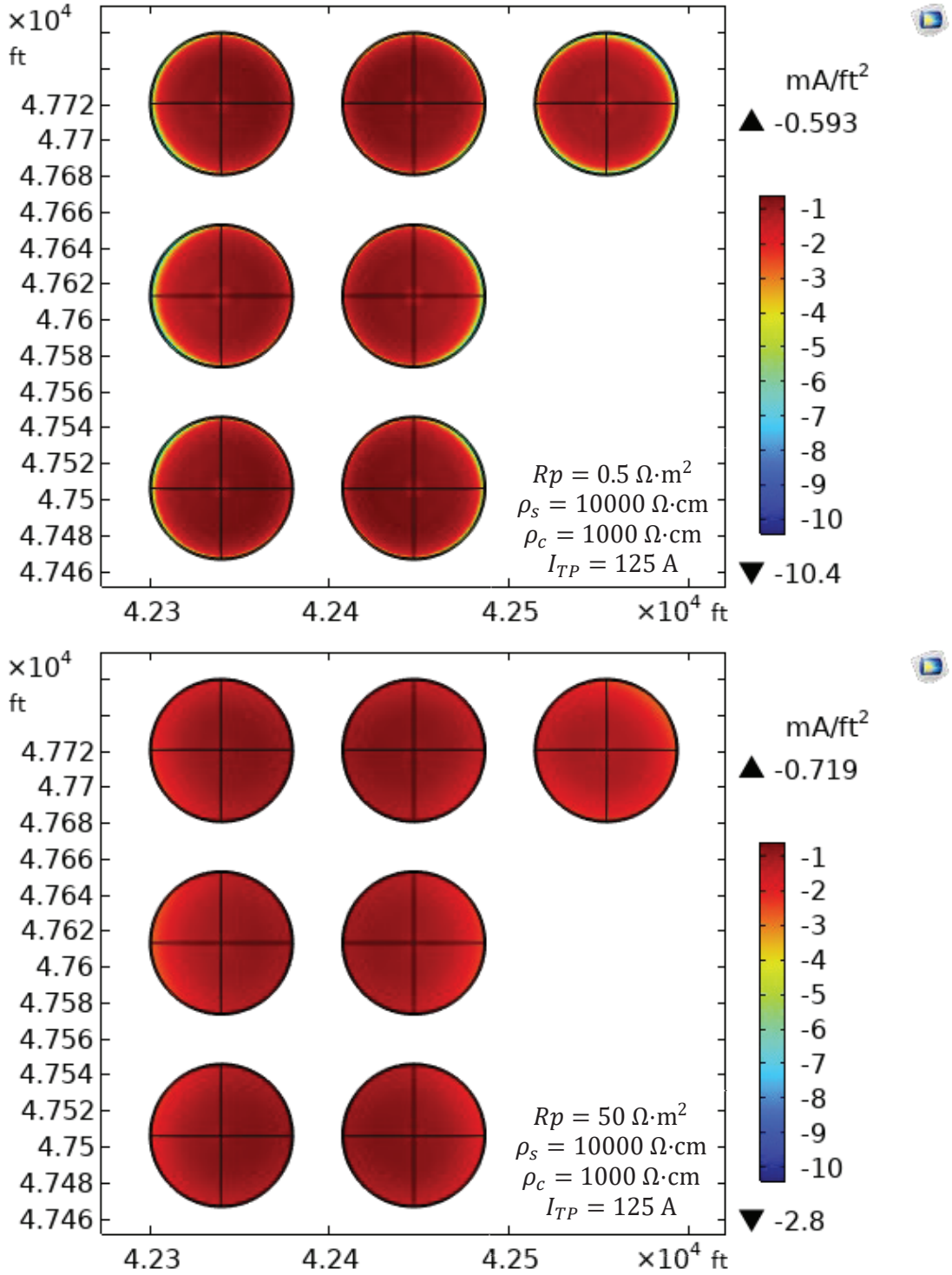

Figure 14. Tank-bottom current density with 125 A current to TP anodes for (top) $Rp = 0.5\ \Omega{\cdot}m^2$ and (bottom) $Rp = 50\ \Omega{\cdot}m^2$ with the same color scale.

Table 17 and Figure 15 show the currents to various components for different values of the soil resistivity ρ_s ranging from 1000 to 10000 Ω·cm for simulations with $\rho_c = 1000$ Ω·cm and $Rp = 5$ Ω·m^2, and 125 A to the deep anodes. At the low end, the soil and concrete resistivities are equal, $\rho_s = \rho_c = 1000$ Ω·cm. The component currents sum to the total anode current of 134.7 from both sets of anodes. As the soil resistivity decreases, the fraction of the current density to the tank bottoms and pipes decreases (becomes less negative), while more current reaches the wall rebar and, to a lesser extent, the dome.

Table 17. Effect of soil resistivity on tank farm current distribution ($\rho_c = 1000$ Ω·cm, $Rp = 5$ Ω·m^2).

	Soil resistivity, ρ_s (Ω · cm)			
	10000	**5000**	**2500**	**1000**
Dome current (A)	-1.36	-1.49	-1.68	-2.09
Walls current (A)	-10.74	-11.14	-11.67	-12.58
Bottom current (A)	-50.56	-48.78	-46.72	-43.75
Dome rebar current (A)	-2.95	-3.25	-3.73	-4.79
Walls rebar current (A)	-31.71	-33.44	-35.65	-39.28
Pipes current (A)	-37.38	-36.62	-35.27	-32.21
Avg. bottom curr. dens. (mA/ft^2)	-1.41	-1.36	-1.30	-1.22

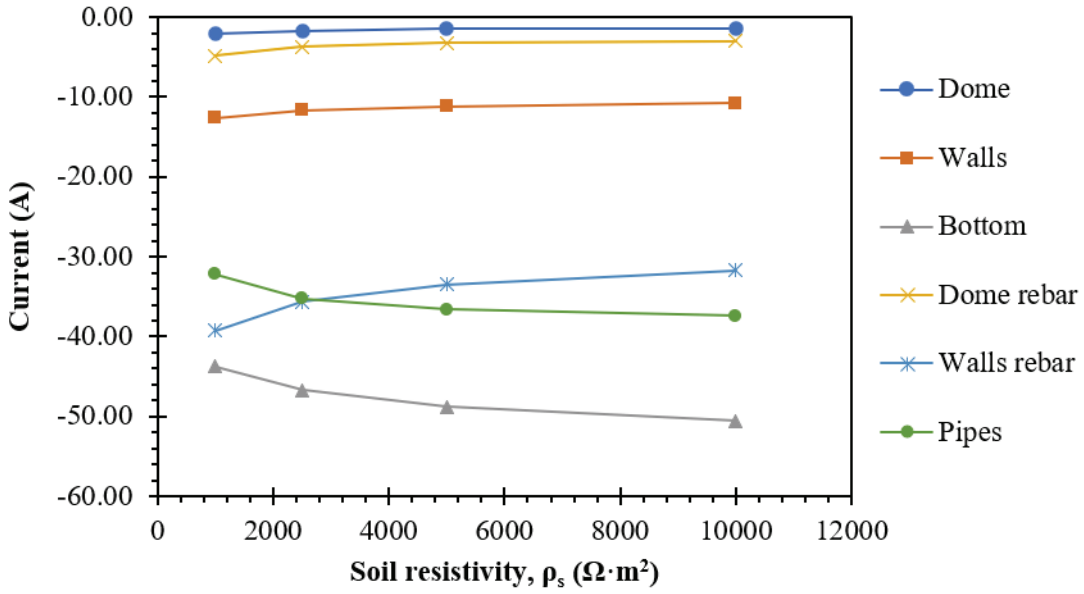

Figure 15. Effect of soil resistivity on tank farm current distribution ($\rho_c = 1000$ Ω·cm, $Rp = 5$ Ω·m^2).

Table 18 and Figure 16 show the currents to various components for different values of the concrete resistivity ρ_c ranging from 1000 to 5000 Ω·cm for simulations with $\rho_s = 5000$ Ω·cm and $Rp = 5$ Ω·m^2, and 125 A to the deep anodes. At the high end, the soil and concrete resistivities are equal, $\rho_s = \rho_c = 5000$ Ω·cm.

Table 18. Effect of concrete resistivity on tank farm current distribution ($\rho_s = 5000$ Ω·cm, $Rp = 5$ Ω·m^2).

	Concrete resistivity, ρ_c (Ω · cm)		
	1000	**2500**	**5000**
Dome current (A)	-1.49	-1.04	-0.71
Walls current (A)	-11.14	-8.21	-5.87
Bottom current (A)	-48.78	-46.84	-44.46
Dome rebar current (A)	-3.25	-3.32	-3.28
Walls rebar current (A)	-33.44	-37.71	-41.66
Pipes current (A)	-36.62	-37.60	-38.73
Avg. bottom curr. dens. (mA/ft^2)	-1.36	-1.30	-1.24

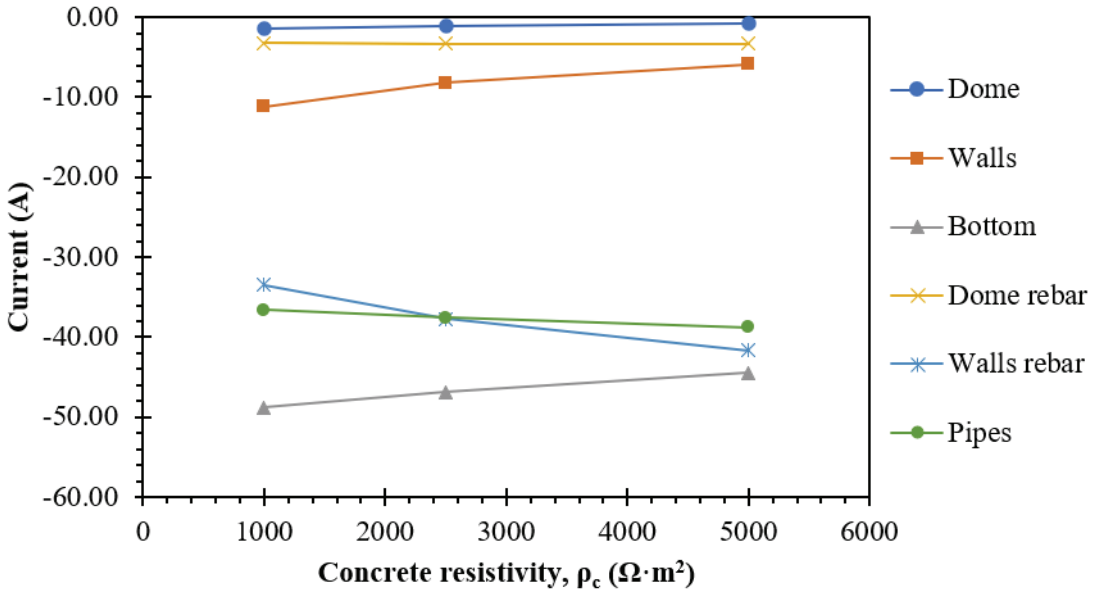

Figure 16. Effect of concrete resistivity on tank farm current distribution ($\rho_s = 5000$ Ω·cm, $Rp = 5$ Ω·m^2).

All of the simulations predict negative, i.e., cathodic, average current to all of the steel structures, and the local current densities on the tank shells and rebar were exclusively negative.

For most of the simulations discussed above, current on the piping was also exclusively negative, but two simulations, with $\rho_s = 10000$ Ω·cm and $Rp = 0.5$ Ω·m^2 or 5 Ω·m^2 (Table 16), predicted local non-negative current on small portions of the piping (<0.4% of the total 20962 ft in the model). For $Rp = 0.5$ Ω·m^2 and $\rho_s = 10000$ Ω·cm, it consisted of ~79 ft of the piping, with an average current of $< 4 \times 10^{-4}$ mA/ft (maximum 3.5 mA/ft); for $Rp = 5$ Ω·m^2 and $\rho_s = 10000$ Ω·cm, only ~1.3 ft with an average of $< 10^{-6}$ mA/ft (maximum 0.07 mA/ft). The regions predicted to lack cathodic current consisted of very short sections of pipe scattered across the tank farm. Note that these results are very similar to those for the simulations with only the PP anodes active (Sect. 5.5.2).

5.5.4 Potentials for tank farm (assessing overprotection and step/touch potentials)

Confirming protective (cathodic) currents is one of the major aims of the simulations, but there are several electric potentials that are also important to check:

- The voltage at the anodes required to drive the CP current determines the power output required to run the system.
- Overprotection/excessively large polarization (instant-off potential <-1.1 V or -1.2 V), as described in Sect. 2.1, may cause damage to structures by causing hydrogen gas generation at the surface, potentially resulting in embrittlement or damage to coatings. In the FEA model, the negative of the potential at the steel surface, i.e., $-\varphi_{surf}$, is equivalent to the instant-off potential. Therefore, regions with $-\varphi_{surf} < -1.1$ V indicate risk of overprotection damage.
- The electric potential distribution at ground level indicates whether there is a danger of hazardous step and touch potentials (Sect. 2.1).

Table 19, Table 20, and Table 21 show the voltage of the deep TP anodes, the minimum $-\varphi_{surf}$ on the pipes, rebar, and tank shell, the amount (length or area) of overprotected structure where applicable, and the maximum ground-level electric potential for the same tank-farm simulations discussed in Sect. 5.5.3.

Table 19. Effect of polarization resistance on tank farm potentials ($\rho_c = 1000$ Ω·cm, $\rho_s = 10000$ Ω·cm).

	Rp=0.5 Ω·m^2	Rp=5 Ω·m^2	Rp=10 Ω·m^2	Rp=50 Ω·m^2
Anode voltage (V)	87.48	87.64	87.79	88.63
Min. $-\varphi_{surf}$ on pipes (V)	-1.86	-4.57	-5.66	-8.71
Min. $-\varphi_{surf}$ on rebar (V)	-0.54	-0.71	-0.86	-1.75
Min. $-\varphi_{surf}$ on shell (V))	-0.56	-0.81	-1.01	-2.01
Overprotected pipe length ($-\varphi_{surf} < -1.1$ V) (ft)	3.62	520.67	2121.1	5273.4
Overprotected rebar length ($-\varphi_{surf} < -1.1$ V) (ft)				5891.7
Overprotected shell area ($-\varphi_{surf} < -1.1$ V) (ft^2)				1850.8
Max. ground-level potential (V)	12.18	12.40	12.60	13.73

Table 20. Effect of soil resistivity on tank farm potentials ($\rho_c = 1000\ \Omega\cdot$cm, $Rp = 5\ \Omega\cdot m^2$).

	Soil resistivity, ρ_s ($\Omega \cdot$ cm)			
	10000	**5000**	**2500**	**1000**
Anode voltage (V)	87.64	44.22	22.48	9.40
Min. $-\varphi_{surf}$ on pipes (V)	-4.57	-3.11	-2.11	-1.36
Min. $-\varphi_{surf}$ on rebar (V)	-0.71	-0.69	-0.68	-0.65
Min. $-\varphi_{surf}$ on shell (V))	-0.81	-0.77	-0.72	-0.67
Overprotected pipe length ($-\varphi_{surf} < -1.1\ V$) (ft)	520.67	398.67	284.35	106.75
Max. ground-level potential (V)	12.40	6.60	3.68	1.89

Table 21. Effect of concrete resistivity on tank farm potentials ($\rho_s = 5000\ \Omega\cdot$cm, $Rp = 5\ \Omega\cdot m^2$).

	Concrete resistivity, ρ_c ($\Omega \cdot$ cm)		
	1000	**2500**	**5000**
Anode voltage (V)	44.22	44.37	44.54
Min. $-\varphi_{surf}$ on pipes (V)	-3.11	-3.18	-3.26
Min. $-\varphi_{surf}$ on rebar (V)	-0.69	-0.73	-0.76
Min. $-\varphi_{surf}$ on shell (V))	-0.77	-0.76	-0.74
Overprotected pipe length ($-\varphi_{surf} < -1.1\ V$) (ft)	398.67	434.18	461.57
Max. ground-level potential (V)	6.60	6.71	6.83

The anode voltages range from 9 to 89 V and are unsurprisingly determined by the soil resistivity, with almost no change with Rp or ρ_c.

All of the simulations predicted a non-zero amount of overprotected pipe, with the amount increasing most strongly with increasing Rp and, to a smaller extent, with increasing ρ_s or ρ_c. The total length of pipe in the simulation is 20962 ft, so the worst-case scenario at $Rp = 50\ \Omega\cdot m^2$ (Table 19) predicts ~25% of the pipe is overprotected. The $Rp = 50\ \Omega\cdot m^2$ simulation was also the only case that predicted overprotection for a portion of the tank shell and rebar.

Figure 17 shows the overprotected regions for the case with $Rp = 50\ \Omega\cdot m^2$ (Table 19). The high polarization regions occurred around the edges of the tanks (outer sections of the tank bottoms and a small region of wall and wall rebar close to the bottom) and in piping that was not located above a tank. Figure 18 shows the overprotected piping for $Rp = 5\ \Omega\cdot m^2$ and $Rp = 10\ \Omega\cdot m^2$ (Table 19). Again, the overprotection occurs in regions of the piping not located over tanks; for $Rp = 5\ \Omega\cdot m^2$, only piping very close to the simulation boundary is affected, which could be an artifact of how the boundaries are handled.

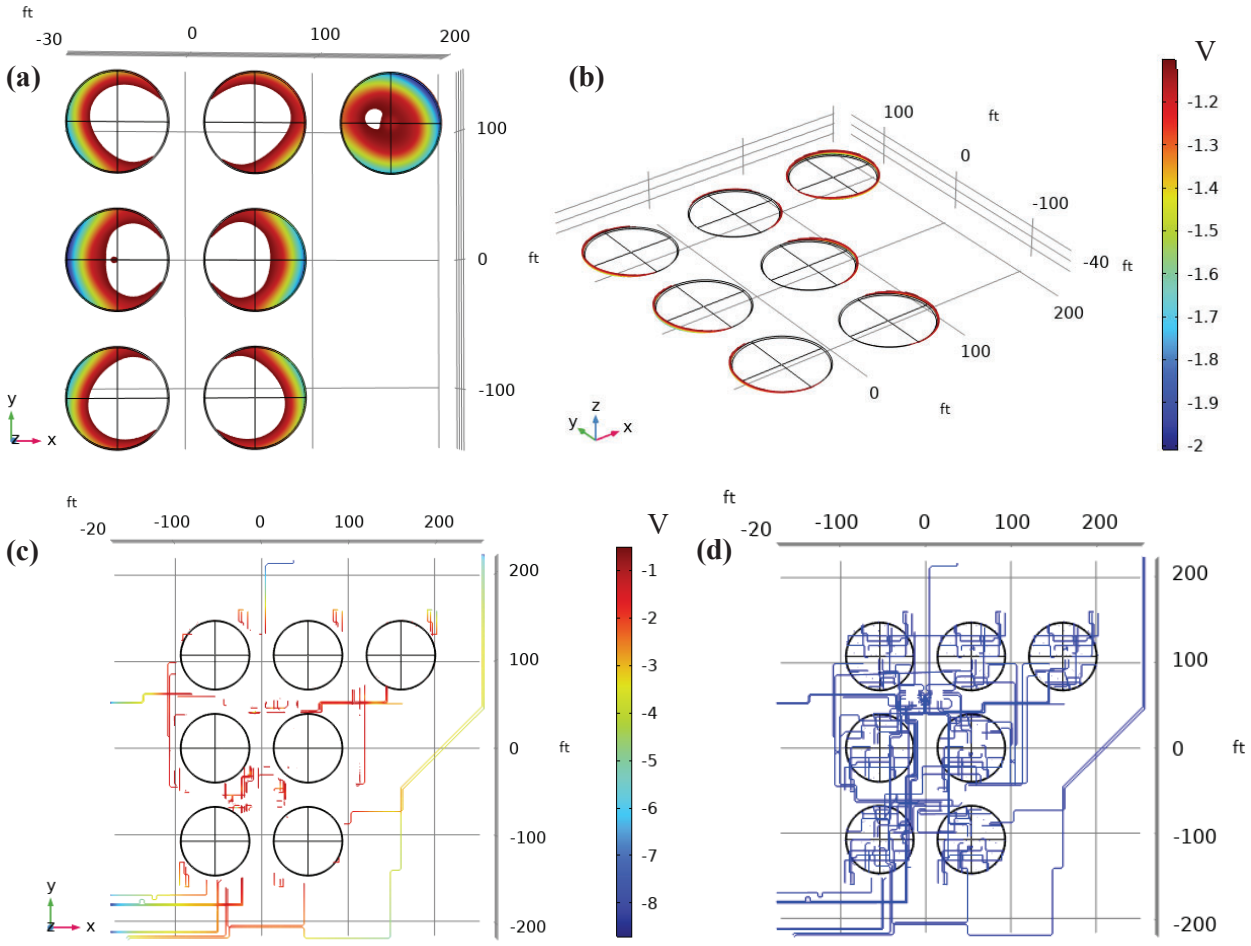

Figure 17. Surface polarization $-\varphi_{surf}$ in overprotected regions (< -1.1 V) of (a) the tank bottoms (same color scale as (b)), (b) the tank wall and wall rebar, and (c) the piping for $Rp = 50\ \Omega{\cdot}m^2$, with (d) the full piping layout for comparison.

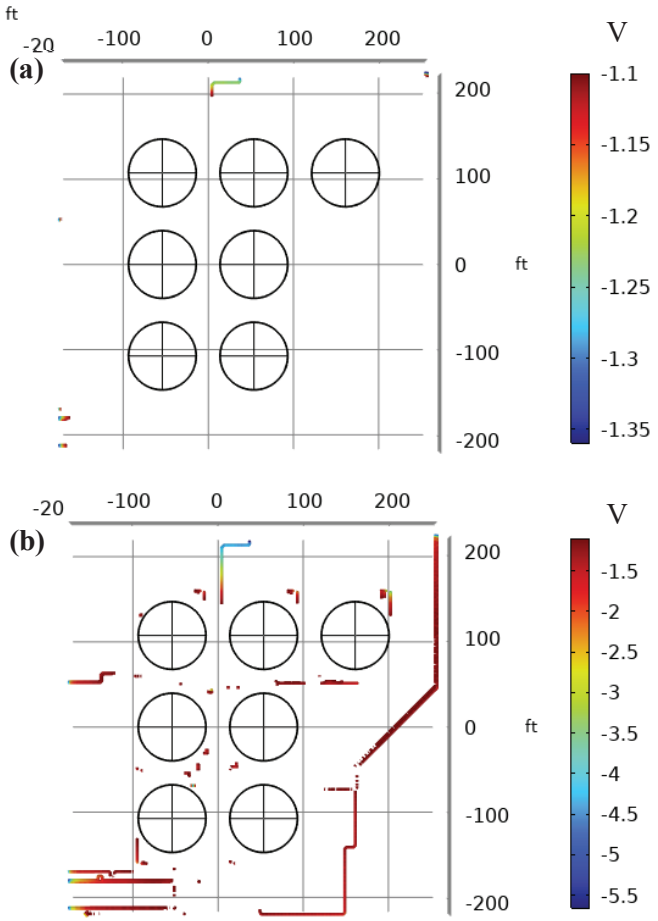

Figure 18. Surface polarization $-\varphi_{surf}$ in overprotected regions (< -1.1 V) of the piping for (a) $Rp = 5$ Ω·m^2 and (b) $Rp = 10$ Ω·m^2.

For all of the models simulated here, the ground-level potentials were exclusively positive, with maximum values <15 V. Therefore, there is no possibility of a step or touch voltage >15 V, even if someone simultaneously touched the 0-V steel structure and the highest-potential ground-level location.

6.0 Conclusions

Circuit and FEA models of single CP-protected tanks and FEA models of a CP-protected tank farm were applied to assess the potential for protecting the bottom of Hanford double-shell tanks from further corrosion. All models predicted that significant protective current could be delivered to the bottom of the tank with the addition of TP anodes below the depth of the tanks. Simulations with only the existing PP anodes active confirmed that only a very small current is predicted to the tank bottoms under present conditions. In these models, all current delivered by the anodes must flow to the CP-protected steel structures, and the magnitude of the total current does not change the distribution to different portions of the structure, so the current density to a given component could be scaled up or down by changing the overall imposed anode current.

Multiple simplified representations of the dome and wall rebar were tested to reduce the computational complexity of the simulations. The selected rebar representation models the rebar as “edge” (line) elements with the surface current density multiplied by an effective circumference to yield a current per unit edge length. In addition, the geometry of the rebar is simplified and the effective circumference scaled up to match the actual rebar surface area with the shorter rebar length; the final models use a single layer of

horizontal hoops of rebar around the walls of the tank and radial rebar over the dome, with separate circumferences for dome and wall rebar to individually match the rebar area in these regions. This edge/line representation was also used for piping and PP anodes in the full tank-farm model.

Current distributions were found to be similar for edge vs. surface representations of the rebar, as well as for different orientations (horizontal vs. vertical) of simplified rebar geometry. The edge representation was consistently found to be slightly more "transparent" (more current reaching the tank shell and less going to the rebar) than modeling the rebar surface as hollow cylinders, but it massively reduced the degrees of freedom of the model and the time required to simulate it. Overall coverage/placement of rebar in the correct rebar was found to be important, with omission of the dome rebar resulting in much higher current to the dome and correspondingly lower rebar current, even when the wall rebar area was adjusted to match the rebar area for the entire tank. The current to the tank bottom, the primary focus of this study, remained fairly consistent across all of the rebar representations tested for the dome and walls.

The predicted electric potential distribution over the steel surfaces indicated a risk of overprotection (polarized potential <-1.1 V) of piping near the edges of the tank farm, and (for higher Rp values) piping in the spaces between the tank footprints. The predicted amount of overprotected area was strongly dependent on the value of Rp used, and at the highest value (50 $\Omega \cdot m^2$), overprotected regions were also predicted on the tank bottoms. Identifying an appropriate value of Rp to use in the simulations would be important to accurately assess this risk; in addition, the predicted structure-to-electrolyte potentials on overprotected piping reached magnitudes up to 8.7 V, so the model assumption of low overpotential may need to be revisited to accurately assess this.

Comparison between the FEA models and the circuit model representation demonstrated that the circuit model could not match the current distribution predicted by FEA, even when using the same surface areas. FEA simulations with different anode depths and with a deeper tank depth confirmed that this is at least partly attributable to the relative positions of different components, e.g., tank and anodes, and by their proximity to the ground surface. These relative positions are accounted for in the FEA model but cannot be accounted for by the circuit model. In particular, the circuit model representation underpredicts the current to the tank bottom and overpredicts the current to the dome compared to FEA for the baseline geometry.

The current model omitted the rebar from the concrete slab, which is electrically isolated from the tank, due to difficulties finding an appropriate and tractable modeling approach for it. However, the circuit-based stray current model estimated that only 2.1% of the total current through the slab will stray into the rebar, corresponding to ~0.21 A for a target current density of 2 mA/ft^2 to the tank bottom. This amount of stray current is estimated to yield a lifetime of >400 years for the minimum rebar diameter, assuming an acceptable cross-section area loss of 10%.

7.0 Path forward and future model refinements needed

7.1 Rebar amount and distribution

Several people individually estimated the amount (length, volume, and surface area) of rebar in the walls and dome of the concrete vault based on the drawings. Totals were similar, but the amounts of rebar associated with the dome versus the walls differed greatly. Some of the discrepancy is likely due to rebar in the region around the transition from the vertical wall into the curve of the dome, with different people reaching different conclusions of what rebar in this region belonged to the dome vs. the wall region.

"Wall" and "dome" rebar are separated in the simplified rebar representation of the model. Therefore, the choice of how to divide the total rebar into "wall" and "dome" rebar to size the respective simplified rebar makes a difference in the resulting model.

Further refinement of the model should assess how much impact this discrepancy has on model results of interest, and, if found to be significant, try to refine these estimates.

7.2 Anode electrical output (existing pipe-protection system)

Maximum currents are prescribed for each anode, and the CP survey report provides information about the two AN rectifiers. However, accurate operating currents for these anodes are to be determined. Comparison of FEA predictions (PP anodes only) with past test station measurements may help to refine or confirm more realistic PP anode currents.

7.3 Deep anode locations

The current simulations tested only one location for the deep, TP anodes, based on input from CorrPro. However, this may not be the optimal location for CP protection, and additional simulations to optimize this may be beneficial for designing the new system. For example, a different distribution of anodes might better deliver current to the tank bottoms without increasing the current to the piping to the point of overprotection.

7.4 Soil and concrete resistivities and polarization resistance

The current modeling used various representative ranges for the electrical resistivities of the soil and the concrete and for the polarization resistance of the steel surface. Identifying more accurate values for these variables would enable more accurate predictions, particularly for the range of electric potential.

Soil resistivity values have been measured on the Hanford site in the past, e.g., [15] and [16]. Since soil is very inhomogeneous, a range of resistivity values may be appropriate. A tank farm could also be simulated with a non-uniform distribution of soil resistivity if site-specific measurements indicating the actual distribution were available. To the best of our knowledge, no Hanford-specific data is available for the concrete used in the vaults; however, the concrete was made following ASTM/ACI standards, and it may be possible to correlate the known properties of the concrete to a more precise resistivity range.

7.5 Effective medium/porous electrode representation of pad

No feasible approach for FEA simulation of the electrically isolated rebar in the bottom slab of the tank model was identified in this work. COMSOL representatives suggested that the effective medium/porous electrode functionality may be useful for simulating the current that would go through the bottom reinforced slab, and future work could explore whether this approach would improve the simulation of the CP currents. (Stray currents would continue to be assessed using only the spreadsheet circuit model in this approach.)

7.6 Circuit-model improvements

Ref. [17] provides the "most well-known formula for calculation of the ground resistance of a vertical ground rod" of length L and radius r, buried in soil of resistivity ρ, as

$$R_{cyl} = \frac{\rho}{2\pi L}\left(ln\left[\frac{2L}{r}\left(1+\sqrt{1+\left(\frac{r}{2L}\right)^2}\right)\right]+\frac{r}{2L}-\sqrt{1+\left(\frac{r}{2L}\right)^2}\right). \quad \textbf{11}$$

In the limit of $L \gg r$, this simplifies to approximately $\frac{\rho}{2\pi L}\left(\ln\left[\frac{4L}{r}\right]-1\right)$ [17], the same as the single-anode form of Eq. 1, but for the walls of the tank, the full expression would be needed because its radius is greater than its height. This formula should be explored to potentially replace the current formula for the resistance of the cylindrical tank wall for a more accurate representation of the actual geometry and to eliminate the arbitrary factor n.

The scaling used in Eq. 6 to estimate the resistance of a network of closely spaced cylinders based on a plate-anode resistance is also in question and needs verification or refinement. It is possible that a more appropriate formula for horizontal bars may be found, e.g., perhaps something similar to Eq. 2 that was used for the ground-grid resistance.

In general, the efficiency and clarity of the circuit model implementation could likely be improved by developing the set of model equations analytically rather than proceeding step-by-step in a spreadsheet. E.g., the stray-current model takes user inputs (the soil and concrete resistivities) and calculates numerous voltages that have no effect on the final current distribution, corrosion rate, or lifetime predictions. Developing the equations analytically could have revealed that these variables drop out, simplifying the calculations and providing clearer insight into what factors are important for this analysis.

7.7 Experimental investigation of stray currents

Bench-scale experiments were planned [18] to experimentally simulate layers of soil, reinforced concrete, and steel representative of the tank bottom pad, with a DC current imposed between an anode in the soil layer and the steel plate to represent the CP system, as shown in Figure 19. The rebar in the concrete would be electrically isolated from the steel and soil to mimic the bottom pad structure. The experiments would aim to determine whether the anode can deliver a protective cathodic current through the rebar to the steel plate and investigate the effect on rebar corrosion rate.

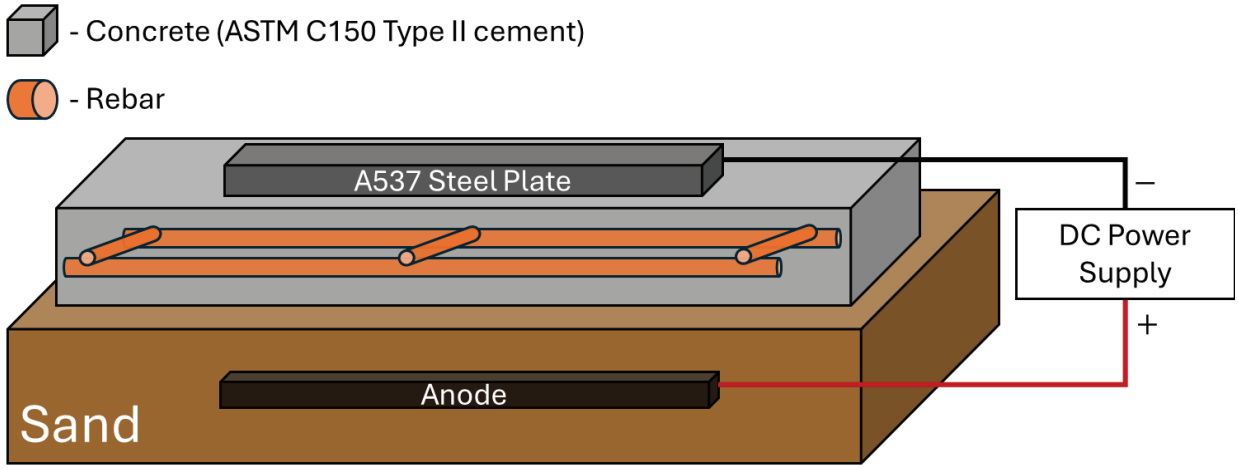

Figure 19. A initial proposed lab-scale experimental setup to test the effects of isolated rebar on impressed-current CP of steel plate and associated corrosion of the rebar [18].

The setup shown in Figure 19 with only one steel-plate cathode would be consistent with the assumptions of the CorrPro stray-current model (Sect. 3.3) where all of the imposed current must ultimately flow through the rebar to the cathode, making it suitable to assess rebar corrosion under a known current flow.

The method of measuring the corrosion rate of the rebar in concrete was anticipated to use electrical-resistance measurements through hollow surrogate rebar. (This was proposed in lieu of techniques like linear polarization resistance and electrochemical impedance spectroscopy, that were expected to be challenging for measurements within the concrete medium.) Applying a low current through the “rebar” and measuring its resistance will detect changes in thickness due to corrosion. The use of hollow steel tubes will reduce the amount of initial steel so that the corrosion metal loss will be a higher fraction of the metal and thus produce a stronger signal in the resistance change. Visual inspection of the rebar and steel plate would be performed at the conclusion of the experiment.

To test the impact of the rebar on the CP current distribution itself, the inclusion of one or more additional steel-plate cathodes without rebar between the cathode and anode would probably be required allow investigation of whether isolated rebar alters the current distribution between the cathodes. E.g., the setup could use two steel-plate cathodes situated symmetrically with respect to the anode so that equal current would be expected to each, with the only difference between them being isolated rebar in the slab below one cathode. The measured difference in current could be compared to circuit-model predictions to see whether simply accounting for the volume fraction of rebar in the concrete resistivity is sufficient to predict

the impact on current distribution. The core measurements here would be simpler, since the total current distribution between the individual cathodes could be measured with ammeters in series with each individual cathode.

This experimental effort was paused.

8.0 References

1. Huber, J., *Volume 4: IQRPE DST System Integrity Assessment - Cathodic Protection for DST Transfer Lines*, 2007, RPP-25299, Rev. 1.
2. Page, J.S., *Work Plan for the 2026 Double-Shell Tank System Integrity Assessment*, 2024, Washington River Protection Solutions, LLC, RPP-PLAN-65866.
3. NACE International, *CP 4-Cathodic Protection Specialist Course Manual*, 2000, Version 1.00.
4. Hall, M.N., *Annual Protected Pipeline CP Status Report Based on 2024 Annual Survey Data*, 2025, Hanford Tank Waste Operations & Closure, RPP-RPT-47435, Rev. 9.
5. NACE International, *CP 3–Cathodic Protection Technologist Course Manual*, 2008.
6. Association for Materials Protection and Performance (AMPP), *Mitigation of Alternating Current and Lightning Effects on Metallic Structures and Corrosion Control Systems*, 2026, NACE SP0177-2026.
7. Kaiser Engineers Hanford Company, *Structural Concrete Tank Foundation Plan and Details*, 1982, U.S. DOE Richland Operations Office,, H-2-90439.
8. Vitro Engineering Corporation, *Structural Concrete Tank Foundation Plan and Details*, 1977, U.S. DOE Richland Operations Office,, H-2-71904.
9. Carlos, W.C., *Cathodic Protection System Operating Experience for Underground Piping at the Hanford Site*, 1992, Westinghouse Hanford Company, WHC-SA-0648-FP.
10. *AP tank farm drawings: H-2-90439, Rev. 1; H-2-90441, Rev. 2; H-2-90442, Rev. 2; H-2-90443, Rev. 2*. 1982, US Department of Energy, Richland Operations Office.
11. Shukla, P.K., A. Nordquist, and R.E. Fuentes, *Cathodic Protection Design Considerations for Facilities with Congested Areas*, 2020, Savannah River National Laboratory, P.R.C. International PR644-183602-R01.
12. *AN Tank Drawings: H-2-71904; H-2-71906; H-2-71907; H-2-71975, Rev. 3; H-2-71103; H-2-71105; H-2-71106; H-2-71160, Rev. 2*. US Department of Energy, Richland Operations Office.
13. *AN Tank Farm Piping and Dome Penetrations Drawings: H-2-71979, Rev. 11; H-2-71986, Rev. 10; H-2-71987, Rev. 7; H-2-71991, Rev. 15; H-2-71992, Rev. 16; H-2-71993, Rev. 10; H-2-71994, Rev. 13; H-2-71995, Rev. 14; H-2-71996, Rev. 11; H-2-72039, Rev. 10; H-2-71989, Rev. 4; H-2-73843, Rev. 4; H-2-90635; H-14-104389, Rev. 5; H-14-104536, Rev. 2; H-2-70550, Rev. 4; H-14-010501, Rev. 29*. US Department of Energy, Richland Operations Office.
14. Peng, Y., et al., *Spatial characteristics of stray current corrosion of reinforcing bars in pseudo concrete.* Structural Concrete, 2022: p. 1–15.
15. Jaske, R.T., *Evaluation of Soil Corrosion at Hanford Atomic Products Operation Summary Report - Underground Pipeline and Structure Corrosion Study Program*, 1955, Hanford Atomic Products Operation, HW-33911.
16. Key, K.T., *Nuclear Waste Tank and Pipeline External Leak Detection Systems*, 1977, Atlantic Richfield Hanford Company, ARH-ST-127.
17. Tsiamitros, D., et al., *Ground resistance of a vertical ground rod in homogeneous earth*, in *2022 2nd International Conference on Energy Transition in the Mediterranean Area (SyNERGY MED)*. 2022: Thessaloniki, Greece. p. 1–6.
18. Farelas, F., B. Barkai, and M. Neveau, *Technical Task Plan for Laboratory-Scale Experiments Associated with Hanford Tank Bottom Cathodic Protection to Mitigate Soil-Side Corrosion*, 2025, Savannah River National Laboratory, SRNL-RP-2025-00824.

Appendix A. Geometry values used in circuit models

Table A-1. Geometric characteristics used in CorrPro current-distribution circuit model (Sect. 3.2).

All cable characteristics (used for R1, R2, R4)				
Size (AWG)	2			
Unit resistance (Ω/1000 ft)	0.159			
Resistances R1 and R4 (rectifier wires)	**R1 (positive)**	**R4 (negative)**		
Cable length (ft)	50	100		
# parallel cables	2	2		
Resistance R2 (anodes)				
Anode column length (ft)	150			
Anode column diameter (in)	8			
# anode columns	3			
Spacing between anodes (ft)	75			
Cable length from rect. to Anode 1 (ft)	100			
Cable length from rect. to Anode 2 (ft)	200			
Cable length from rect. to Anode 3 (ft)	300			
Resistance R3A (ground grid)				
Width and length of earth per tank (ft)	100			
Grid spacing (horiz.) (ft)	25			
Grid spacing (vert.) (ft)	50			
Ground cable size	~4/0			
Ground cable diameter (in)	0.5			
Cable depth (ft)	5			
Tank resistances R3B-R3E	**R3B (tank dome)**	**R3C (tank walls)**	**R3D (tank bottom)**	**R3E (slab rebar)**
Tank diameter (ft)	80	80	80	
Height (ft)	15	38.34		
Surface area tank shell (ft)	6289	9637	5027	
Concrete thickness (ft)	2	1.5	2	
Est. total length of rebar (ft)	57388	31432		29322
Est. total surf. area of rebar (ft^2)	16902	9258		6470
Est. total volume of rebar (ft^3)	396	217		115

Table A-2. Geometric characteristics used in CorrPro stray-current circuit model (Sect. 3.3).

Tank diameter (ft)	80	
Slab diameter (ft)	89.5	
Total concrete thickness (ft)	2	
	Pick-up region ("lower")	**Discharge region ("upper")**
Zone thickness (ft)	1	1
Zone volume (ft^3)	7556	5027
Rebar		
Est. total length of rebar (ft)	23598	14605
Est. total surf. area of rebar (ft^2)	5273	2923
Est. total volume of rebar (ft^3)	100.5	47.4

Distribution:

SRNL
eric.pierce@srnl.gov
morgana.whiteside@srnl.gov
charles.james@srnl.gov
william.jolin@srnl.gov
joseph.manna@srnl.gov
pavan.shukla@srnl.gov
kiana.sykes@srnl.gov
mark.kranjc@srnl.gov
kareen.blue@srnl.gov
nicholas.valdes@srnl.gov
christine.langton@srnl.gov
naim.kabir@srnl.gov
haley.jones@srnl.gov
anna.dentremont@srnl.gov
maxwell.alderman@srnl.gov
richard.wyrwas@srnl.gov
chris.martino@srnl.gov
michael.stone@srnl.gov
Records Administration (EDWS)

DOE
em-labcall@em.doe.gov
ming.zhu@em.doe.gov
sailendra.mahapatra@hq.doe.gov

H2C
jason_s_page@rl.gov
shawn_t_campbell@rl.gov
jason_r_gunter@rl.gov
melinda_r_fagundes@rl.gov
stephanie_r_doll@rl.gov
david_j_swanberg@rl.gov
rodney_s_skeen@rl.gov
zabrina_b_smith@rl.gov